Proceedings of the 4th Meeting of Japan CF Research Society

Edited by Hiroshi YAMADA

October 17-18, 2002

Iwate University, Japan

Preface

This book is Proceedings of the 4th Meeting of Japan CF-Research Society, JCF4 which was held at Iwate University, Morioka Japan, on October 17-18, 2002.

Japan CF-Research Society (JCF) was established in March 1999. The main aim of the society is to investigate the nuclear reactions that occur in the solid-state or condensed matter, especially in low energy regions. CF stands for Condensed-matter Fusion, Coherently-induced Fusion, Cleaner Fission, Cold Fusion and other nuclear reactions in condensed matter. And the main goal is expected to develop science and technologies to extract useable energy from CF phenomena. CF researches cross traditional academic domains and require an interdisciplinary approach in collaboration efforts of nuclear physics, fusion science, radiation physics, condensed-matter physics, surface and catalysis science, metallurgy, hydrogen science, electrochemistry, calorimetry, accelerator and beam science, laser science, nuclear and quantum-science and engineering, molecular dynamics, acoustics, thermodynamics, physical chemistry, and so on. Another significant goal of the society is to enhance Japan's role as a focal point of research in this area and to act as a clearing house for international cooperation and information exchange. This commonly reasons why we employ English as conference language and publish books of ABSTRACTS and PROCEEDINGS in English. For the past three meetings, JCF1, JCF2 and JCF3, we published books of ABSTRACTS only on our web-site (http://www.eng.osaka-u.ac.jp/nuc/03/nuc03web/JCF/). The society has decided to issue books of PROCEEDINGS for further meetings from the JCF4 meeting, as printed versions and electronic versions in our web-site.

Submitted papers to JCF4 were peer-reviewed by the editorial board (Chairman: Prof. Hiroshi Yamada, Iwate University). One or two reviewers were selected by the board to review papers, comment problems and errors, return to authors for correction. Most papers were accepted to publish via one-through reviewing processes with minor corrections.

In JCF4 Meeting, there came about 50 participants and 26 papers were presented (see JCF4 ABSTRACTS). This book of JCF4 PROCEEDINGS contains 21 full papers through submission and reviewing processes. For non-JCF members, inquiry to obtain a copy of book should be sent to Prof. Hiroshi Yamada (Faculty of Engineering, Iwate University, Morioka Japan; yamada@dragon.elc.iwate-u.ac.jp).

We thank all participants of JCF4 for their efforts to make this PROCEEDINGS and hope the information of this proceedings useful to further progress of CF studies.

Akito Takahashi (Prof., Osaka University), Director-in-Chief of JCF

Hiroshi Yamada (Prof., Iwate University), Chairman of JCF Editorial Board

January, 2003

CONTENTS

THEORY

Performance of Electrolysis Cell and Thermal Behavior of Deuterated Metals in 0.1M LiOD

Hiroo Numata numata@mtl.titech.ac.jp

Tokyo Institute of Technology, 2-12-1 O-okayama, Meruro-ku Tokyo Japan 152-8552

Abstract: An isoperibolic calorimeter has been constructed. To attain low noise instrumentation, a thermo-regulated tap water has been used as a coolant, however, the abrupt change of the flow rate influences the level of the heat recovery. It is suggested that an ordinary pump driven coolant supply equipment could attain the acceptable level of heat recovery. The function of PID control has been checked by measuring heater current of the auxiliary heater responding to the temperature difference between Tcell and the surroundings.

Keywords: isoperibolic calorimeter, heat calibration, data acquisition system

1. INTRODUCTION

Low noise and reliable measurement system for an accurate data analysis are key issues to cold fusion study. Miscellaneous phenomena [1-2] and solid-state properties [3], i.e., surface voids and fault formation during the electrochemical hydrogen/deuterium evolution on Pd were studied using in-situ measurement of the physico-chemical properties of the Pd-H system and SEM observation [4]. The absorption of deuterium into a Pd electrode has been known to be inhomogeneous, there, however, is remained unsolved yet the relationship between the generation of heat and neutron and these peculiar surface and solid-state phenomena.

In this experiment, a new calorimeter and data acquisition system have been constructed. The Joule heating calibration has evaluated the heat transfer characteristic of the calorimeter.

2. EXPERIMENTAL

2.1 Experimental set up

An electrolytic cell with double walled water jacket, made by transparent quartz was placed in a Cu box (7; referred to number shown in Fig.1). It was plugged with a silicone rubber stopper (4) where the ports for the electrolyte feed and evolved gas release (12); the holders of three electrodes and the calibration heater (2) are equipped. Electrolyte content is 150 ml. The detail of the electrolytic cell has been reported elsewhere [1-2].

In the experimental set up calibrated Pt resistance thermometers (Netsusin Co. Ltd.) were used, which were located in the box and the electrolytic cell,

Tin: inlet of coolant, Tout: outlet of coolant, Tcell: electrolytic cell, Tcell room : space over electrolyte, Troom: properly located in the box and inserted into coolant tubing, as shown in Fig.1 The nominal accuracy of Pt resistance thermometer is ± 0.01 ℃. We report here our effort to measure calibrated heat generation in the previously improved cell placed in the constant temperature box (7), made by Cu plate (0.8 mm thickness). To ascertain thermal homogeneity in the room and the electrolytic cell four longitudinal walls of the box are cooled/heated through properly attached Cu tubing. As shown in Fig.1, the temperature of a heat transfer medium in the Cu tubing is controlled through a heat exchanger (10). Even though the water flow is thermally regulated, the temperature variations have been measured to be ± 0.075℃ due to the room temperature fluctuations.

An accurate measurement necessitates well-performed accessories, i.e., power supply (constant power), coolant supply system furnished with rotor type flow meter (turbine meter MF1/2X50B, indicator FC801-2LPA, Japan flow control Co. Ltd.), Potentiostat with GPIB bus and the calibration and auxiliary heaters.

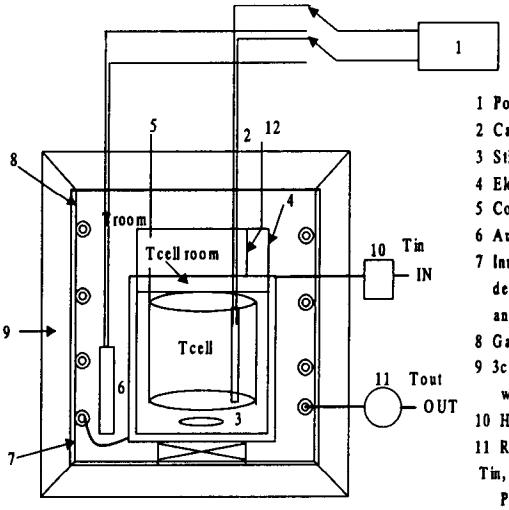

Fig.1 Schematic view of open electrolytic cell

The box containing heat generation device and electrolytic cell is thermally insulated to minimize the influence of the room temperature fluctuations. In spite of sufficient knowledge about our hardware characteristics design changes have been made as a result of the preliminary examinations. For example, the specifications of cooling fan and stirrer were carefully suited to maintain the cell and box temperatures constant.

It is noted that motor driven equipments (stirrer, water circulation for cooling) were rejected and miscellaneous electrostatic noise shielding for apparatus and noise cut trans for electricity were adopted to eliminate electric noise.

3. RESULTS AND DISCUSSION

3.1 Data acquisition system and PID control

The data acquisition system was designed to compare neutron counting rate, heat generation, Pd electrode potential, D/Pd ratio (evaluated by analysis of Pd resistance value) and possibly dilation. That is, the time correlation among these observations will be checked within the 10 ms time scale. This time scale was determined by a chosen number of clock cycles and a software delay: 20 micro s with respect to the instrument. The data acquisition system is schematically shown in Fig.2. One IBM computer drives a measurement instrument (Agilent HP34970A) and a computer controlled Potentio/ galvanostat (BASIC driven) through a GPIB interface. The driver software of the instrument was originally obtained from the corresponding web site.

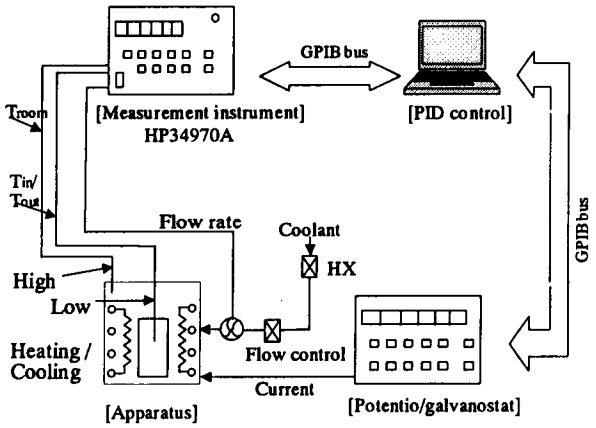

Fig.2 Diagram of data acquisition system and PID control

The data acquisition system was further modified to process temperature control of the box. Figure 3 shows the schematic diagram of data processing with

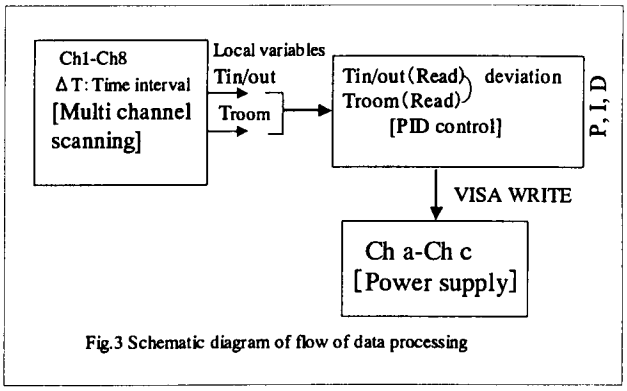

Fig.3 Schematic diagram of flow of data processing

LabVIEW software. The measurement instrument reads and stores the temperature values: Troom, Tin/Tout (the latter essentially representing the temperature of the cell) and time. The data transfer between the measurement loop and PID control was done using the local variable technique in one assembled program. When a deviation between these temperatures is detected, the PID control program processes and sends the commands (VISA Write) to the power supply. Thus, the power applied to the heater generates heat to eliminate a deviation. Concurrently, the electric fan rotates frequently, although the time interval and size of the fan should be properly adjusted to avoid blow the cell directly.

Figure 4 shows time dependence of the flow rate and the applied power (supplied to auxiliary heater: 700ohm) during an initial period of the performance test. Since the temperature difference between Troom and the temperature of wall of the water jacket, which could equilibrate with the coolant temperature, was apparent compared with the base lines, the heater current of the power supply was measured as a result of active PID control. The small difference in these temperatures could be attributed to the change of the surroundings, which originates active PID control to maintain the heat conduction conditions constant during a whole experimental run.

3.2 Heat generation calibration

Heat calibration tests have been conducted to make sure whether heat recovered is acceptable level or not using a

new calorimeter. We have designed an isoperibolic calorimeter keeping the following items in mind,

1 Adequate cell volume accessible to long term electrolysis
2 Optional measurement probes close to the cell, which requires the cell surrounded not by liquid but by air
3 Attainment facile thermal homogeneity in the box furnished with PID controlled heater and fan and also the box walls made by Cu plate furnished with Cu cooling tubing
4 Rapid heat transfer from the source to a heat transfer medium with water jacket

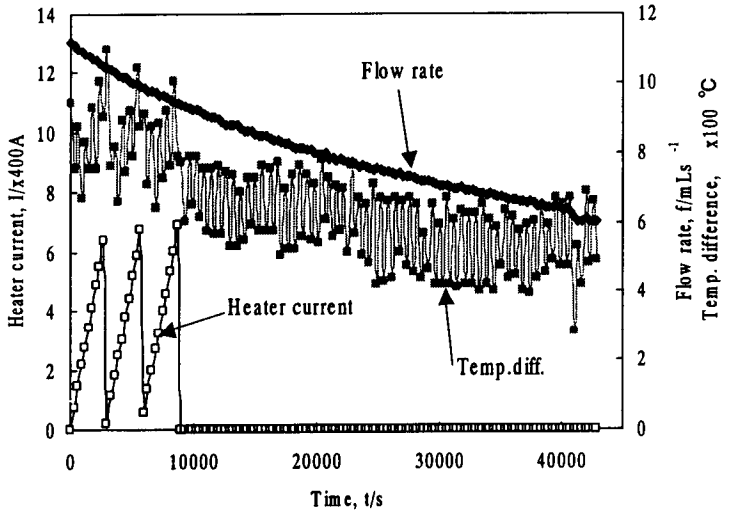

Fig.4 Time variation of flow rate and heater power (supplied to auxiliary heater: 700ohm) during an initial period of performance test (time interval 5min)

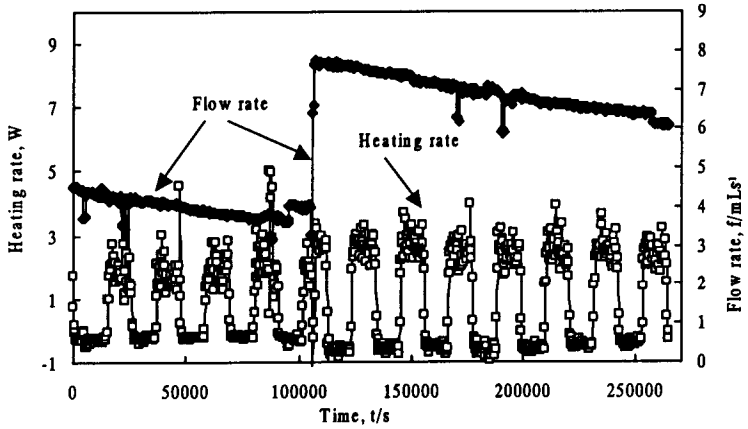

Fig.5 Time variation of flow rate and heating rate recovered during a Juol heater calibration

5 Low noise instrumentation

In isoperibolic calorimetry the heat generated in the cell is determined by the following,

$W=Kf\Delta T$ K: 4.184

where K is a constant given as the specific heat of water, f is flow rate and ΔT is the temperature difference between Tin and Tout at the water jacket.

The calibration heater (400ohm, sheathed by SUS316) was donated by the manufacturer. The heater power control and data acquisition system are almost the same as the above except that the output of the power supply is connected to the calibration heater.

Figure 5 shows variation of the flow rate and heat recovered as a function of time. The input power was 4.2W (4h ON/OFF mode) during the whole experimental run. At the initial times the low level flow rate produces lower output power, while after a total time of 10^5 s the power level recovered increased to be 85% of the input power: these heat recovery is strongly depending on the flow rate. The continued experimental runs show that the heating rate fluctuations during input power ON is responded to those of the surroundings (the temperature difference between Troom and Tin/Tout). Firstly, it is pointed out that some modification with respect to the coolant supply system will reduce the temperature drift of the thermo regulated water flow.

To address low noise instrumentation, tap water whose flow rate is regulated by the stopcock has been introduced to the Cu tubing attached to the Cu box as a coolant. However, it is significant to replace this water supply system to an ordinary pump driven, thermo regulated coolant supply equipment. In addition, the possible temperature drift of the heat transfer medium; i.e., due to the room temperature fluctuations and

bubble inclusion might be properly corrected using PID controlled auxiliary heater.

Acknowledgements: The author would like to thank Dr. T. Mizuno of Hokkaido University for his insightful discussions.

References:

1) Ryuzo Takagi, et al.: Neutron Emission During a Long-term Electrolysis of Heavy Water; Fusion Technol., 19, 2135-2139(1991)
2) Hiroo Numata et al.: Neutron Emission and Surface Observation During a Long-term Evolution of Deuterium on Pd in 0.1LiOD; Conf. Proc. Vol.33 of ACCF2, "The Science of Cold Fusion", p.71-79 (1991)
3) Hiroo Numata et al.: Low-Temperature Elastic Anomalies and Heat Generation of Deuterated Pd; Fusion Technol., 31, 300-310(1997)
4) Hiroo Numata et al.: In situ Potentiometric, Resistance and Dilatometric Measurements of Pd Electrode During Repeated Electrochemical Hydrogen Absorption; Fusion Technol., 38, 206-223 (2000)

HEAT MEASUREMENT DURING LIGHT WATER ELECTROLYSIS USING FLOW CELL (Ⅲ)

H.Inoue, M.Fujii, S.Mitsushima, N.Kamiya and K.Ota

Depertmant of Energy and Safety Engineering, Yokohama National University
79-5 Tokiwadai, Hodogaya-ku, Yokohama 240-3501, JAPAN

Abstract: We reported clear excess heat during light water electrolysis at ICCF9 in Beijing. In order to confirm these results, we have conducted heat measurement, separately, using the improved cell with the compression of electrode beads and the thermal insulator. The electrode beads were Ni rods, Ni beads or Al_2O_3 beads, with Pd thin film on the surface that was formed by sputtering or chemical plating. The electrolyte was Li_2SO_4-H_2O or K_2CO_3-H_2O solution. The electrolysis was performed with constant current. Due to compression of electrode beads the cell voltage was stabilized and the oxidation of electrode was suppressed. The accuracy of measurements was improved considerably. In several experiments, small excess heat (less then 5%) was observed. However, we have not observed a clear excess heat (10% or more) during these experiments.

1. INTRODUCTION

In our laboratory we have studied the heat measurements using Patterson Type Power Cell, and we observed clear excess heat in several experiments.[1] However, the problems was the poor reproducibility and the large variation. The purpose of this study is to improve the accuracy of measurement and to performed heat measurement using the improved cell.

2. EXPERIMENT

Figure.1 shows the two types of the electrolytic cell which were used in this study. Cell-1 is the cell used before. Cell-2 is the cell that improved Cell-1. The electrodes were the electrode beads for cathode and Pt mesh for the anode. Electrode beads are Ni rods (ϕ 1mm × 2mm), Ni beads (ϕ 1mm) or Al_2O_3 beads (ϕ 1mm), with Pd thin film on the surface which was formed by chemical plating or sputtering. Electrolyte was 1.0 mol/l Li_2SO_4-H_2O, 1.0 mol/l or 0.5 mol/l K_2CO_3-H_2O solution, and it was circulated through the cell. As shown in Figure.1, it entered from the cathode side of a cell, and it went away from the anode side with the gas that was generated during electrolysis. The electrolyte flow rate was about 40 ml/min. The electrolyte inlet temperature and the room temperature were kept at

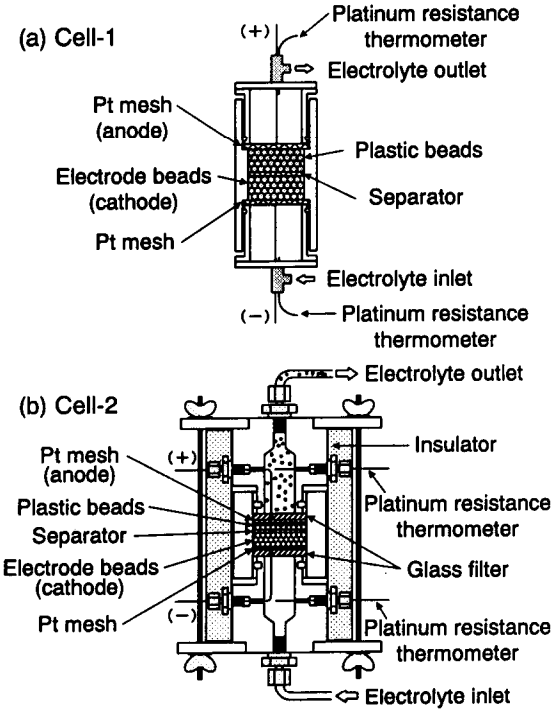

Fig.1 Electrolytic cell

25℃ and 22℃, respectively. Electrolysis was performed with constant current (1.0A) except one experiment. At the experiment the current was changed from 0.1 to 3.0A. During electrolysis, we measured the cell voltage, the cell current, the electrolyte inlet temperature, the electrolyte outlet temperature, the electrolyte flow rate and the gas flow rate of the gaseous product (H_2 + O_2).

The output energy during electrolysis was obtained mainly by the temperature increase of the electrolyte. The temperature of the electrolyte was measured at the inlet and the outlet of the cell using the platinum resistance thermometers. The output energy was corrected by measuring the gas flow rate of the gaseous product. The heat loss through the wall of our system was neglected in this study. The loss was considered to be very small compared to two factors, since the electrolyte temperature was kept very close to the room temperature and the cell was insulated.

The heat balance was calculated by the following equations.

$$W_0 = V \times I \quad (1)$$

$$W_1 = FR \times \Delta T \times d \times Cp \quad (2)$$

$$W_2 = (2/3) \times V_g \times Q \quad (3)$$

$$HB\# = W_1 / W_0 \quad (4)$$

$$HB = (W_1 + W_2) / W_0 \quad (5)$$

Where W_0 is the input energy, W_1 is the output energy that was used for temperature increase of the electrolyte, W_2 is the output energy that was used for electrolysis, HB# is heat balance when output energy is only W_1, HB is heat balance when output energy is the sum of W_1 and W_2, V is the cell voltage, I is the cell current, FR is the electrolyte flow rate, ΔT is the temperature difference from the electrolyte inlet temperature to the electrolyte outlet temperature, d is electrolyte density, Cp is the thermal capacity, V_g is the gas flow rate of the gaseous product, and Q is the reaction enthalpy of water electrolysis.

The excess heat was evaluated by HB.

3. RESULT AND DISCUSSION

One of the improved points of Cell-2 is setting of glass filters both side of the cell which enabled the compression of electrode beads. Due to this compression the cell voltage was stabilized. Figure.2 shows the comparison of the cell voltages of Cell-1 and Cell-2, when the electrolyses conducted on same conditions except the cell. The cell voltage of Cell-1 was stabilized for about first 10 hours, but the tendency to decrease greatly was observed later. On the other hand the cell voltage of Cell-2 was stabilized throughout electrolysis, and it became possible to suppress variation considerably compared with Cell-1. Although Pd plating on the electrode beads oxidized easily at the experiment using Cell-1, the oxidation of electrode was suppressed by the compression. Other improved points of Cell-2 were the cover of side wall with the glass wool to decrease the heat loss through the wall of the cell and changing the cell configuration to pass

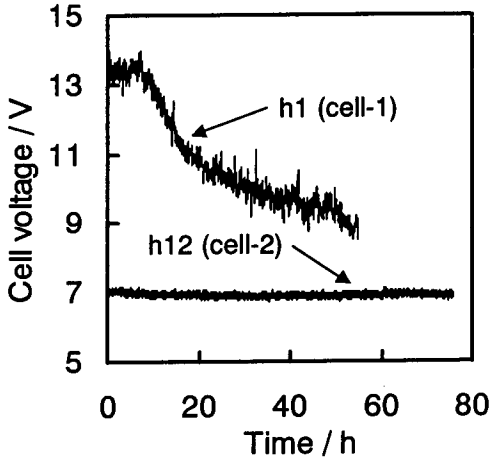

Fig.2 Cell voltage during electrolysis using Ni rods

the generated gas through the cell smoothly. Thus measurement date was stabilized, and accuracy and reliability improved considerably. Although there were some differences at every experiment, accuracy improved from about ±10% to about ±5% after the improvement.

First, the result of one experiment among the 23 experiments conducted this time is described. This experimental condition was that the electrolytic cell was Cell-2, the electrolyte was 1.0 mol/l Li_2SO_4-H_2O solution and electrode beads were Pd/Ni rods that were made by Pd chemical plating. Figure.3 shows the temperature difference (ΔT) and the cell voltage(V) in this experiment. Cell voltage and the temperature difference were stable, and the fixed value continued during electrolysis. In other experiments using the Cell-2 the same tendency was observed. Figure.4 shows heat balance that was calculated from these data. HB# became from 80 to 86%, and HB became from 101 to 103%. HB was larger than 100% by 1-3% and a little excess heat was observed. However, when the account of excess heat was less than 5%, it was not able to conclude the excess heat. Therefore, the excess heat was not able to confirm in this experiment.

Table.1 shows the summary of this study. The experimental conditions and the heat balances of 23 experiments are shown. The heat balance was increased from 94 - 98% to 99 - 102% by changing the cell from Cell-1 to Cell-2, when the electrolyte was 1.0 mol/l Li_2SO4-H_2O solution and current was 1A. It was considered that the heat recovery was improved by the wall insulator. Next, when K_2CO_3-H_2O solution was used as electrolyte, heat balance decreased slightly, compared with the experiments in Li_2SO_4-H_2O solution. In these experiments the current efficiency was down to 70% of the theoretical value. The promotion of H_2 and O_2 recombination might be a main reason for this low heat balance. The electrode beads used in these experiments had the difference in shape, number of plating layer, and the processing methods. But the difference of heat balance was not observed. Therefore the heat balance was not affected by the material of beads.

In 6 experiments out of 23 experiments heat balance over 100% was observed. But the observed excess heat was less than

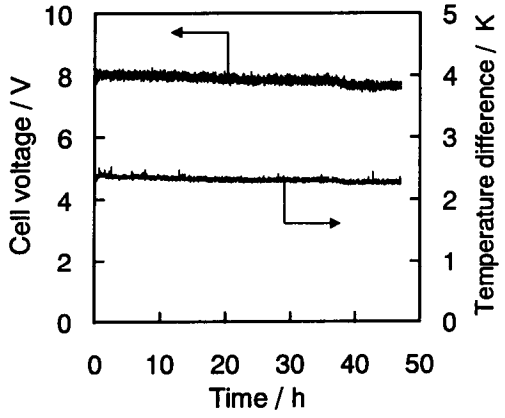

Fig.3 Cell voltage and Temperature difference during electrolysis in Li_2SO_4-H_2O solution using Pd/Ni rods cathode (h8)

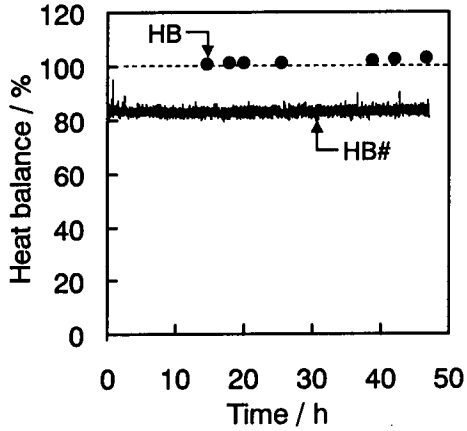

Fig.4 Heat balance during electrolysis in Li_2SO_4-H_2O solution using Pd/Ni rods cathode (h8)

the accuracy (5%). Therefore we have not observed the clear excess heat in these experiments. In order to confirm the small excess heat (<5%), we are trying to improve the accuracy by suppressing on estimating the heat loss through the cell.

4. CONCLUSION

By improving a cell accuracy of heat measurement was improved considerably. Although the small excess heat was observed in 6 experiments out of 23 experiments in the various experimental conditions, the clear difference of heat balance was not observed and a clear excess heat that was observed before has not been observed.

Reference

1) M.Fujii, et al: Abst.JCF3, p.2-3 (2001).

Table.1 Heat balance of 23 experiments

No	Cell	Electrode beads	Electrolyte	Current(A)	Voltage(V)	Ave.HB (Ave.HB#)	Time(h)
h1	Cell-1	Ni rods	1.0mol/l Li_2SO_4-H_2O	1.0	8.5~14.1	95 (81)	54.9
h2	Cell-1	Ni rods	1.0mol/l Li_2SO_4-H_2O	1.0	9.1~14.4	94 (82)	55.4
h3	Cell-1	Ni rods	1.0mol/l Li_2SO_4-H_2O	1.0	9.0~21.4	97 (85)	76.7
h4	Cell-1	Pd / Ni rods	1.0mol/l Li_2SO_4-H_2O	1.0	8.5~9.7	98 (83)	46.2
h5	Cell-1	Pd / Ni rods	1.0mol/l Li_2SO_4-H_2O	1.0	12.4~14.9	96 (85)	47.1
h6	Cell-1	Pd / Ni rods	1.0mol/l Li_2SO_4-H_2O	1.0	14.3~17.3	96 (86)	73.8
h7	Cell-1	Pd / Ni rods	1.0mol/l Li_2SO_4-H_2O	1.0	12.3~15.7	97 (86)	173.1
h8	Cell-2	Pd / Ni rods	1.0mol/l Li_2SO_4-H_2O	1.0	7.5~8.2	102 (83)	47.1
h9	Cell-2	Pd / Ni rods	1.0mol/l Li_2SO_4-H_2O	1.0	7.5~8.1	99 (80)	51.3
h10	Cell-2	Pd / Ni rods	1.0mol/l Li_2SO_4-H_2O	1.0	7.7~8.4	100 (82)	123.7
h11	Cell-2	Pd / Ni rods	1.0mol/l Li_2SO_4-H_2O	1.0	7.0~7.6	101 (82)	55.0
h12	Cell-2	Ni rods	1.0mol/l Li_2SO_4-H_2O	1.0	6.8~7.1	101 (80)	75.6
h13	Cell-2	Pd / Ni / Pd / Ni rods	1.0mol/l Li_2SO_4-H_2O	1.0	7.2~7.6	102 (82)	54.6
h14	Cell-2	Pd / Ni / Pd / Ni / Pd / Ni rods	1.0mol/l Li_2SO_4-H_2O	1.0	6.5~6.8	101 (79)	77.6
h15	Cell-2	Pd / Ni balls	1.0mol/l Li_2SO_4-H_2O	1.0	6.0~7.1	100 (76)	55.3
h16	Cell-2	Pd / Ni balls	1.0mol/l Li_2SO_4-H_2O	1.0	7.1~7.5	100 (80)	72.0
h17	Cell-2	Pd / Ni balls	1.0mol/l Li_2SO_4-H_2O	1.0	11.6~13.8	99 (87)	51.0
h18	Cell-2	Pd / Ni / Ceramic balls	1.0mol/l Li_2SO_4-H_2O	1.0	10.4~12.5	100 (87)	78.6
h19	Cell-2	Pd / Ni balls	1.0mol/l Li_2SO_4-H_2O	1.0	7.1~7.5	99 (80)	53.5
h20	Cell-2	Pd / Ni balls	1.0mol/l Li_2SO_4-H_2O	0.1	3.2	97 (63)	0~22.5
				0.5	5.1~5.3	99 (72)	22.5~43.4
				1.0	7.2~7.5	99 (80)	43.4~66.2
				2.0	10.1~11.1	100 (85)	66.2~94.3
				3.0	13.0~14.1	101 (91)	94.3~107.8
h21	Cell-2	Pd / Ni balls	1.0mol/l K_2CO_3-H_2O	1.0	4.7~4.9	97 (73)	51.7
h22	Cell-2	Pd / Ni balls	0.5mol/l K_2CO_3-H_2O	1.0	5.5~5.7	95 (79)	16.1
h23	Cell-2	Pd / Ni balls	0.5mol/l K_2CO_3-H_2O	1.0	5.6~5.9	96 (79)	95.7

Analysis of Production Elements on Pd Surface after Light and Heavy Water Electrolysis

T. Sato (1), S. Sasaki (1), T. Kubozono (1), S. Narita (1), H. Yamada (1) and T. Ohmori (2)
(1) Dept. of Electrical and Electronic Engineering, Iwate University, Morioka 020-8551 Japan
(2) Catalysis Research Center, Hokkaido University, Sapporo 060-0811, Japan

ABSTRACT

Pd cathode surface after light and heavy water electrolysis has been analyzed by time of flight secondary ion mass spectroscopy (TOF-SIMS). Marked increase in counts for mass numbers from 7 to 208 were observed on the Pd after electrolysis. These correspond to elements of Li, B, Mg, Al, K, Ca, Ti, Cr, Mn, Fe, Co, Ni, Cu, Zn, Ba and Pb. Most of the elements were observed for both light and heavy water electrolysis.

Keywords: light water electrolysis, heavy water electrolysis, nuclear transmutation, TOF-SIMS

1. INTRODUCTION

Various elements have been observed on several metallic cathode after light water electrolysis[1][2]. Those elements have been thought to be formed in a certain nuclear reaction on the surfaces. In this study, we paid attention to avoid contamination, which can be introduced during Pd sample preparation and during experiment. Light and heavy water electrolysis was carried out to analyze surface composition of Pd cathode after the electrolysis.

2. EXPERIMENTAL

Fig. 1 shows the electrolysis cell used. The cells were made of quartz and of polyethylene. These have a cylindrical shape with volume capacity of 200 cm^3 (quartz) and 550 cm^3 (polyethylene). The cells were designed carefully to avoid any possible contamination during sample preparation and the electrolysis. The pressure inside cell was kept to be slightly higher than atmospheric pressure during the electrolysis, though the electrolysis was carried out as an open system. A Pd foil (99.95% pure) of $5 \times 10 \times 0.1$mm and an 80-mesh Pt net were employed as the cathode and the anode for this experiment. The electrolyte solution was 0.5 M sodium sulfate (Merck sprapur reagents) solution. The volume of electrolyte solution was 150-500cm^3. The electrolysis was carried out in a constant current of 0.5 Amps. The constituting elements on the Pd electrode after electrolysis were identified by means of time-of-flight secondary ion mass spectrometry (TOF-SIMS). The SIMS measurement was carried out by Ga^+ ion irradiation. The spectrometry was also performed after 10s sputter cleaning of the Pd surface with the Ga^+ ion. Light water electrolysis was performed for 14 and 30 days, heavy water electrolysis for 14 days, as shown in Table. 1.

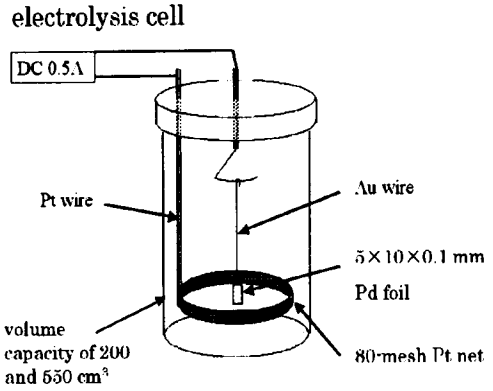

Fig. 1 electrolysis cell

3. RESULT and DISCUSSION

3.1 TOF-SIMS analysis for light water electrolysis

The composition analysis was performed after 10s sputter cleaning by Ga^+ ion beam at three areas, 40×40μm for each, randomly

	Electrolysis period	Electrolyte solution
Exp.1	14 days	0.5M, Na_2SO_4/H_2O
Exp.2	30 days	
Exp.3	14 days	0.5M, Na_2SO_4/D_2O

Table. 1 Condition of the electrolysis.

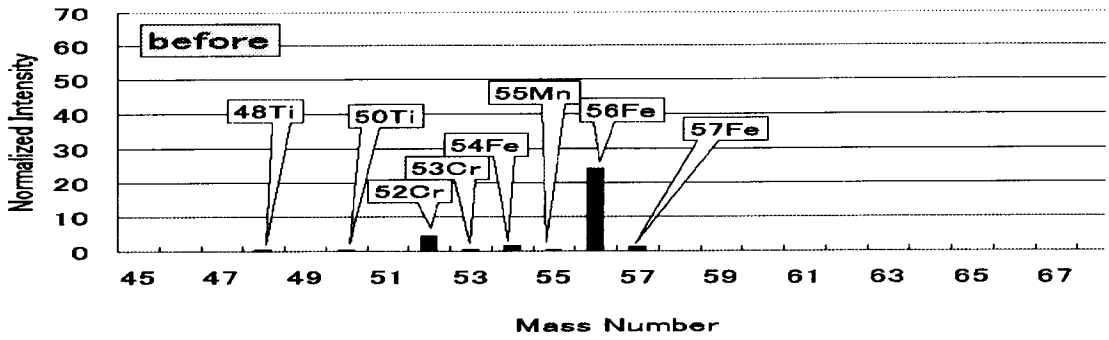

Fig. 2 TOF-SIMS spectrum of Pd immersed in the light water electrolyte.

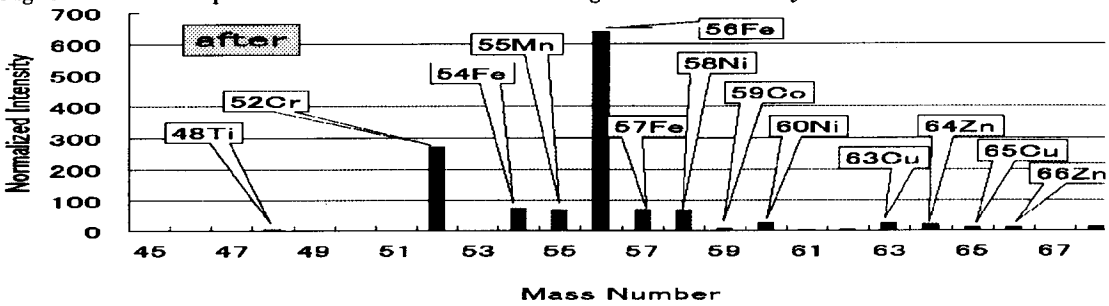

Fig. 3 TOF-SIMS spectrum of Pd after light water electrolysis for Exp. 1.

selected on the Pd surface. Fig. 2 shows a spectrum of a Pd surface for mass range 45-68 after immersing the Pd electrode in the electrolyte for 14 days without electrolysis. The intensity on the vertical axis does not indicate the counts measured and is changed to a normalized intensity for each mass. The normalized intensity defined here is 10^4 times the numerical value obtained by dividing count of mass of each element by total count of signals to normalize. Very low intensity for mass number corresponding to Ti, Cr, Mn and Fe is seen in Fig. 2. Therefore, very few amount of metal element is considered to exist on the Pd surface before electrolysis. Fig. 3 shows a similar spectrum of the Pd after electrolysis for 14 days. One can find marked increase in the intensities corresponding to elements Ti, Cr, Mn, Fe, Co, Ni, Zn and Cu. This Pd sample and that used in the immersing test were prepared from the same rod of Pd foil.

Similar spectra for mass range 130-139 are illustrated in Fig. 4 and 5 as Fig. 2 and 3, respectively. Almost no count for any mass

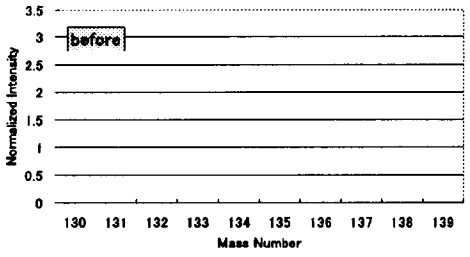

Fig. 4 TOF-SIMS spectrum of Pd immersed in the light water electrolyte.

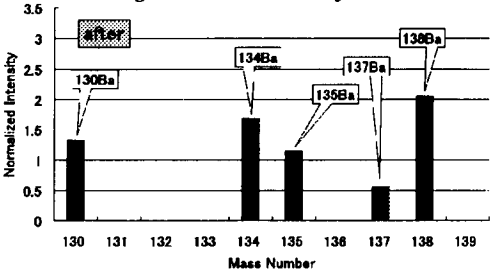

Fig. 5 TOF-SIMS spectrum of Pd after light water electrolysis for Exp. 1.

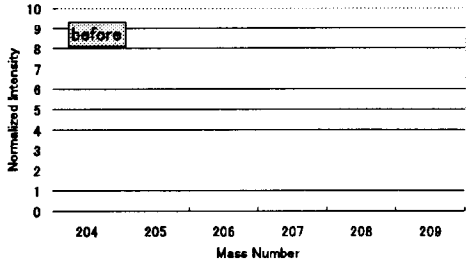

Fig. 6 TOF-SIMS spectrum of Pd immersed in the light water electrolyte.

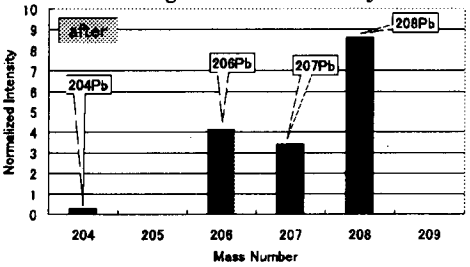

Fig. 7 TOF-SIMS spectrum of Pd after light water electrolysis for Exp. 1.

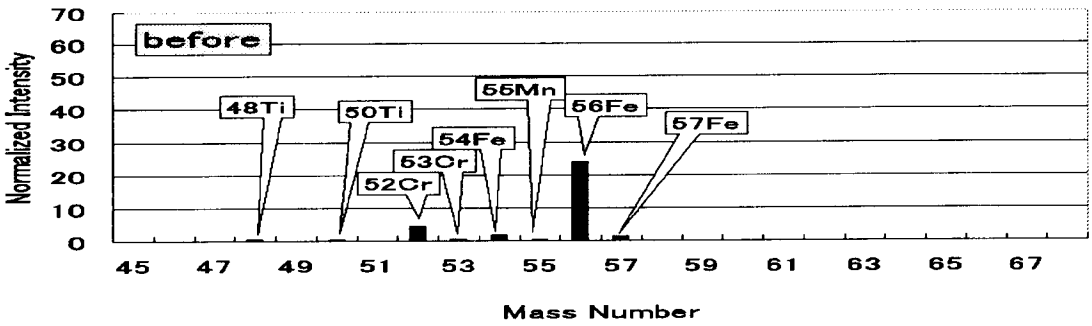

Fig. 8 TOF-SIMS spectrum of Pd immersed in the light water electrolyte.

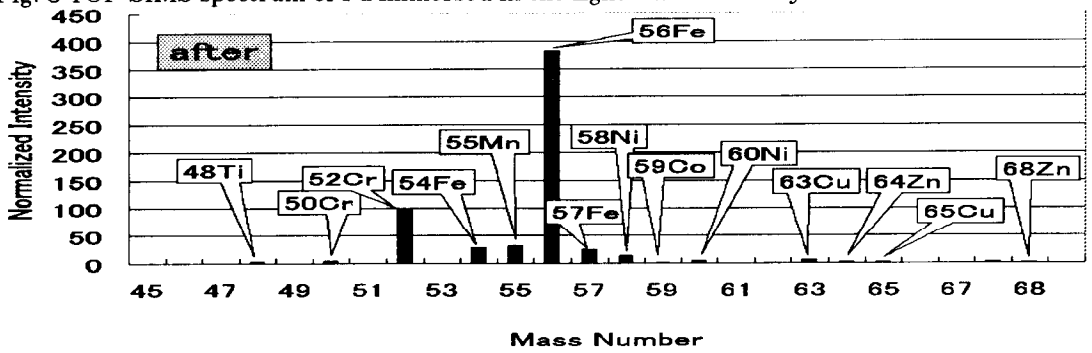

Fig. 9 TOF-SIMS spectrum of Pd after light water electrolysis for Exp. 2.

number is seen in Fig. 4, whereas the remarkable increase in the intensity for mass numbers 130-138 corresponding to Ba can be seen in Fig. 5. Fig. 6 and 7 represent similar spectra for mass range 204-209. Almost no count in the range is seen in Fig. 6. To the contrary, the significant intensity for mass numbers 206, 207, and 208, corresponding to Pb isotopes can be seen in Fig. 7.

The spectra of mass range 45-68 before and after electrolysis for 30 days are given in Fig. 8 and 9, respectively. Similar spectra mass range 130-139 and 204-209 before and after the electrolysis for 30 days are shown in Fig. 10-13. Almost same elements were detected as the case of the electrolysis for 14 days, as can be seen in these Figs.

Besides, considerable increase in amount of

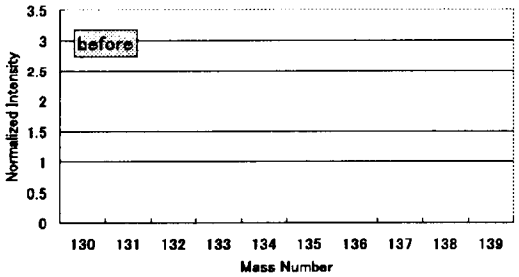

Fig. 10 TOF-SIMS spectrum of Pd immersed in the light water electrolyte.

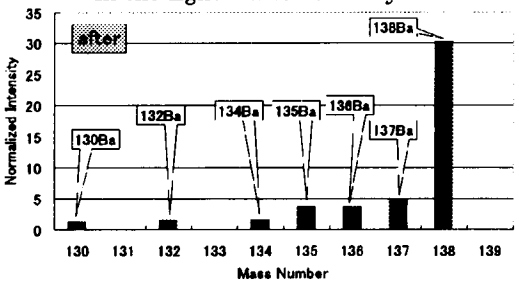

Fig. 11 TOF-SIMS spectrum of Pd after light water electrolysis for Exp .2.

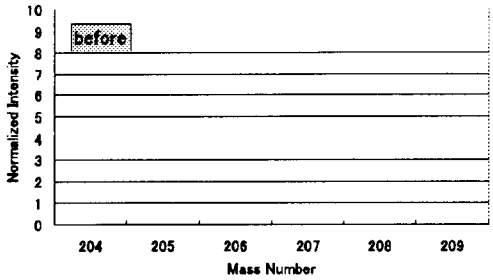

Fig. 12 TOF-SIMS spectrum of Pd immersed in the light water electrolyte.

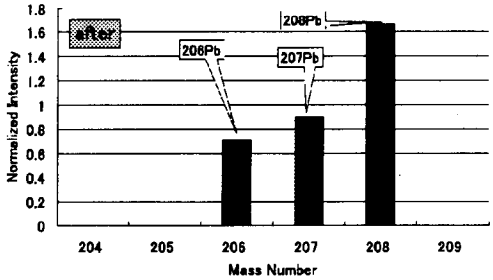

Fig. 13 TOF-SIMS spectrum of Pd after light water electrolysis for Exp. 2.

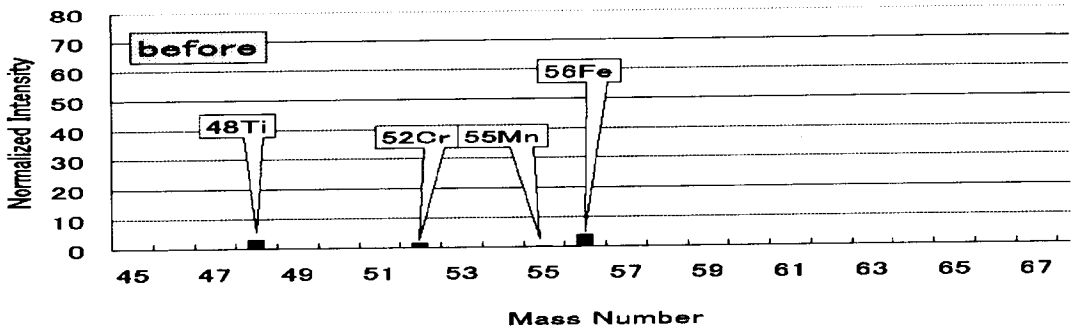

Fig. 14 TOF-SIMS spectrum of Pd immersed in heavy water the electrolyte.

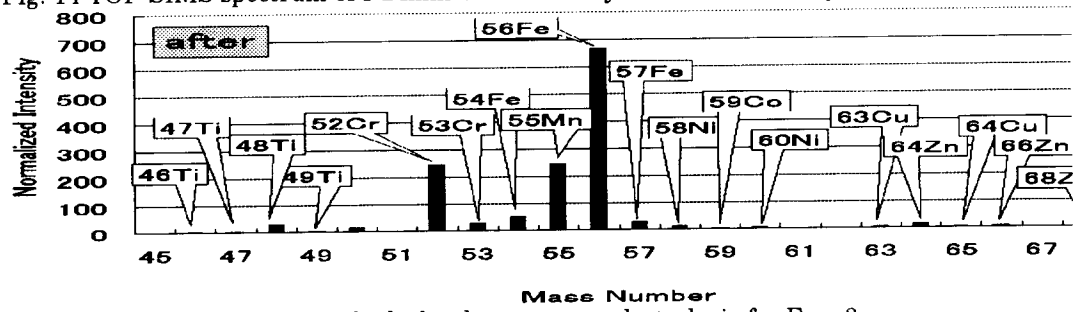

Fig. 15 TOF-SIMS spectrum of Pd after heavy water electrolysis for Exp. 3.

Ca and K were observed by TOF-SIMS. Inductively coupled plasma spectrometry (ICP) has revealed that a very small amount of Ca and K was contained in the electrolyte before electrolysis. Thus, those elements may be contaminants from the environment and the inner wall of test cell.

3.2 TOF-SIMS analysis for heavy water electrolysis

Fig. 14 and 15 show spectra of Pd before and after heavy water electrolysis for 14 days, respectively. One can find considerable increase in the intensities corresponding to elements Ti, Cr, Mn, Fe, Co, Ni, Zn and Cu after electrolysis. These elements agree with those observed after light water electrolysis. However, neither Ba nor Pb were detected after heavy water electrolysis at all. The elements detected at Exp. 3 are summarized in Table. 2 with those for light water electrolysis at Exp. 1 and 2. Whole results indicate that proton has an important role in nuclear transmutation as deuteron do on Pd surface during electrolysis.

4. CONCLUSION

Remarkable increase in amount of Cr, Mn, Fe, Ti and Cu were observed after light and heavy water electrolysis. Co, Ni and Zn are detected after electrolysis with both light and heavy water electrolysis; these elements were not observed before electrolysis. Ba and Pb are observed after light water electrolysis; these elements were not observed after heavy water electrolysis. The elements that were not detected at all before electrolysis but detected on Pd after electrolysis would be produced by nuclear transmutation during electrolysis. However, these elements might be also impurities possibly coming from electrolyte solution, electrodes and environment.

5. REFERNCES

[1] T. Ohmori et al., Fusion Tech., Vol. 31, p. 210 (1997)

[2] T. Ohmori et al., Fusion Tech., Vol. 33, p. 367 (1998)

	Cr	Mn	Fe	Ti	Cu	Co	Ni	Zn	Ba	Pb
Exp. 1	◎	◎	◎	○	○	☆	☆	☆	☆	☆
Exp. 2	◎	○	◎	○	○	○	☆	☆	☆	☆
Exp. 3	◎	◎	◎	○	○	☆	☆	☆	—	—

◎:10≦after/before ○:3≦after/before＜10 ☆:No count before electrolysis

Table. 2 Results of element detection.

Nuclear Reaction Occurring in Light Water Electrolysis on Gold and Cobalt Cathode Electrode

S. Sasaki(1), T. Sato(1), T. Kubozono(1), S. Narita(1), H. Yamada(1) and T. Ohmori(2)

(1) Dept. of Electrical and Electronic Engineering, Iwate University, Morioka 020-8551 Japan
(2) Catalysis Research Center, Hokkaido University, Sapporo 060-0811, Japan

ABSTRACT

Au and Co cathode surface after light water electrolysis have been analyzed by time of flight secondary ion mass spectroscopy (TOF-SIMS). More marked increase of Fe and Cr were observed for Au than for Co cathode after electrolysis. Increasing count intensity of Mg accompanied with decreasing that of Al was observed after electrolysis for Co cathode. Precise analysis of the TOF-SIMS suggests a change in natural isotopic abundance for K took place during the electrolysis.

Keywords : Light water electrolysis, Nuclear transmutation, Isotopic distribution ratio

1. INTRODUCTION

The nuclear transmutation reactions have been investigated by heavy water electrolysis with Pd [1] and Pt [2] cathodes. On the other hand, proton has been considered to play similar role as deuteron in low energy nuclear reaction on solid. Along with this idea, the studies for light water electrolysis have been performed with Ni [3], Au [4, 5] and W [6] cathodes. Elements production has been recognized as the evidence of the nuclear reaction under the electrolysis. Among several methods to identify producing elements, high mass resolution of time of flight secondary ion mass spectroscopy (TOF-SIMS) allows separating the producing new elements from ions fragmentation at the same nominal masses. In this study, elements on the Au and Co electrode before and after light water electrolysis have been investigated by TOF-SIMS.

2. EXPERIMENTAL

In this experiment, two electrolytic cells made of quartz and polyethylene were used. The advantage of using polyethylene cell is that there are fewer possibilities for the electrolyte to be contaminated by contaminants from the inner wall of test cell during electrolysis. These cells have a cylindrical shape with volume capacity of 200 cm^3 (quartz) and 500 cm^3 (polyethylene). Au (99.95% pure) and Co (99.9% pure) foils of $0.1 \times 0.5 \times 10$ mm as the cathode and a 80-mesh Pt net as the anode were employed for the test. The electrolyte was 0.5 M sodium sulfate (Merck suprapur reagents) solution. The volume of electrolyte solution was ~ 150 cm^3 for both cells. The electrolysis was usually carried out mostly for 14 days at a constant DC current of 0.5 Amps. Elements composition of the surface of cathode sample with and without electrolysis was analyzed by TOF-SIMS. The SIMS measurement was carried out by Ga^+ ion irradiation. The spectrometry was also performed after 10s sputter cleaning of the cathode surface with the Ga^+ ion.

3. RESULT and DISCUSSION

3.1 SIMS analysis before and after electrolysis

The composition analysis was performed after 10s sputter cleaning by Ga^+ ion beams at three areas, 40×40 μ m for each, randomly selected on the cathode surface. The mass composition has been found to be almost same over whole analyzed areas. Fig. 1 shows spectrum of Au surface for mass range 49-62 after immersing the Au electrode in the electrolyte without electrolysis for 14 days. Fig. 2 gives a similar spectrum of the Au after electrolysis for 14 days. The Au electrodes were prepared from the same rod. The mass numbers shown on the horizontal axis are not in exact liner scale. The intensity on the vertical axis does not indicate the counts

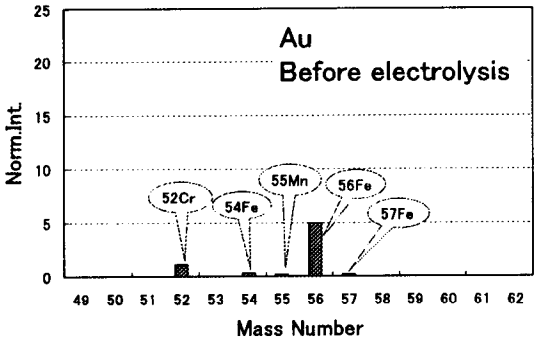

Fig. 1 TOF-SIMS spectrum for Au immersed in the electrolyte.

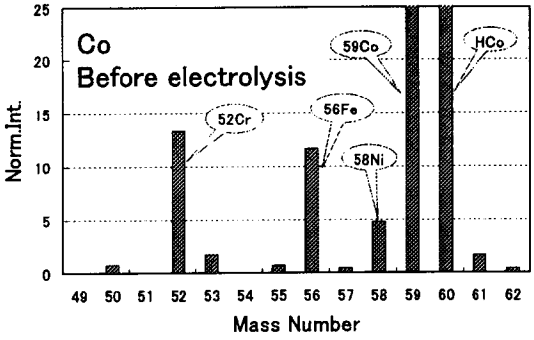

Fig. 3 TOF-SIMS spectrum for Co immersed in the electrolyte.

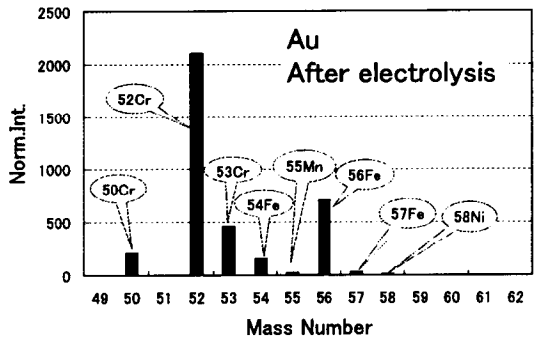

Fig. 2 TOF-SIMS spectrum for Au after electrolysis.

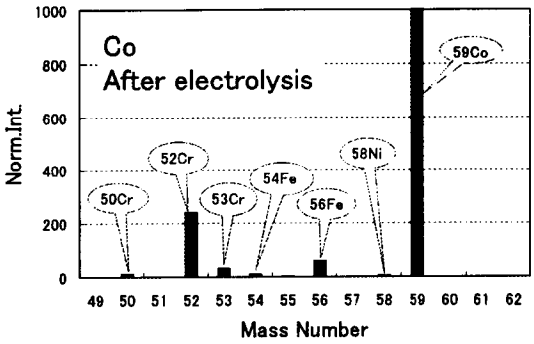

Fig. 4 TOF-SIMS spectrum for Co after electrolysis.

measured and is changed to a normalized intensity for each mass. The normalized intensity means counts per total 10,000 counts. Note that the unit scale of the vertical axis of Fig. 2 is 100 times that of Fig. 1. Very low intensity for mass numbers corresponding to Cr, Mn and Fe are seen in Fig. 1. Very few amount of metal element is considered to exist on the electrode surface before electrolysis. To the contrary, marked increase in the intensity for mass numbers 50−53, 51, 54−57, 55 and 58−60 is seen in Fig. 2, though the counts for mass number 51 and 60 are low to be identified in the figure. These mass numbers correspond to metal elements of Cr, V, Fe, Mn and Ni, respectively. Besides, increasing intensities of mass number 63 and 65, corresponding to Cu, were observed after electrolysis. Moreover, counts for mass number 58, corresponding to ^{58} Ni was detected as a new element.

Similar spectra for Co before and after electrolysis for 14 days are illustrated in Fig. 3 and 4, respectively. Very small amount of contaminants Cr, Fe and Ni before electrolysis is seen in Fig. 3. Considerable increases in counts corresponding to elements Cr, Fe and Ni were also observed after electrolysis, as seen in Fig. 4. Furthermore, counts for mass number 51 corresponding to V were detected after electrolysis.

Cathode	element	After/Before
Au	Fe	~140
	Cr	~1900
Co	Fe	~5
	Cr	~20

Table 1 Ratios of SIMS intensity after electrolysis to that before electrolysis for Fe and Cr.

The increasing ratio of the intensities after to that before electrolysis for each element is different between Au and Co electrodes. Table 1 shows the ratios for elements Fe and Cr detected. The Au

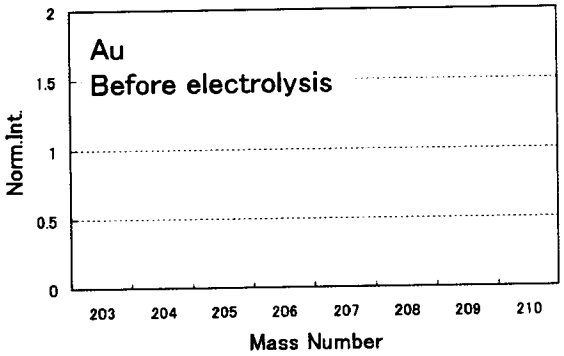

Fig. 5 TOF-SIMS spectrum for Au immersed in the electrolyte.

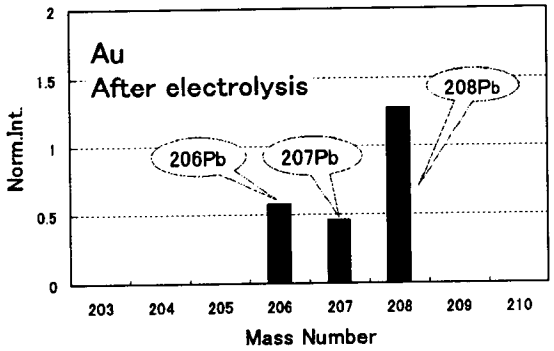

Fig. 6 TOF-SIMS spectrum for Au after electrolysis.

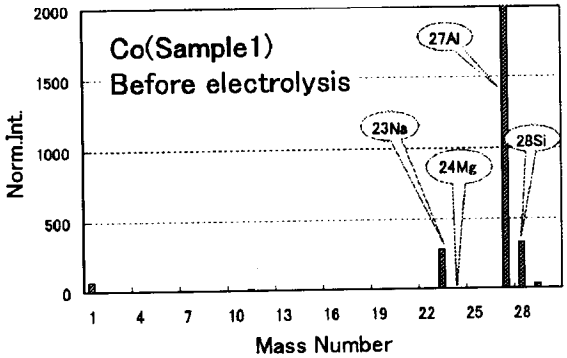

Fig. 7 TOF-SIMS spectrum for Co immersed in the electrolyte.

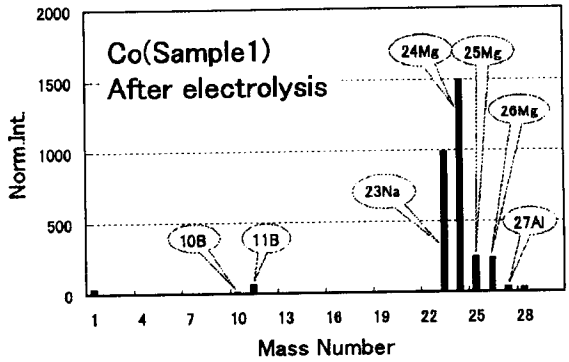

Fig. 8 TOF-SIMS spectrum for Co after electrolysis.

system would produce more amounts of elements than the Co system.

SIMS spectra for mass range 203－210 before and after electrolysis are give in Fig. 5 and 6, respectively. No intensity is seen for this range before electrolysis as shown in Fig. 5. On the other hand, element Pb was sometimes detected on Au electrode after electrolysis as shown in Fig. 6, even though the intensities are low. This

	Before (Norm.Int)	
	Mg	Al
Co Sample1 (Quartz Cell)	2	2851
	2	3111
	2	3261
Co Sample2 (Polyethylene cell)	9	676
	11	900
	3	732
Co Sample3 (Quartz cell)	2	2851
	2	3111
	2	3261

Table 2 Normalized intensity of Mg and Al before electrolysis.

	After (Norm.Int)	
	Mg	Al
Co Sample1 (Quartz cell)	1501	39
	1439	36
	1485	32
Co Sample2 (Polyethylene cell)	284	29
	303	32
	212	29
Co Sample3 (Quartz cell)	85	216
	48	175
	109	143

Table 3 Normalized intensity of Mg and Al after electrolysis.

suggests that a transmutation with increasing mass number beyond that of Au to reach that of Pb occurred during the electrolysis. However, these elements would be also impurities possibly coming from electrolyte solution and environment.

3.2 The relation of count intensities between Al and Mg

The SIMS spectra of Co cathode before and after electrolysis are given in Fig. 7 and 8, respectively. Relatively high intensity of ^{27}Al and low intensity of ^{24}Mg are seen in Fig. 7. Of particular interest is that the intensity of ^{27}Al decreased and that of ^{24}Mg increased during electrolysis as shown in Fig. 8.

The normalized intensities for Mg and Al before electrolysis are given in Table 2. Those after electrolysis are shown in Table 3. The data in these Tables were obtained by the SIMS analysis with three Co samples. One can easily find the decreasing Al with increasing Mg during electrolysis from the Tables. Some amount of Al on the Co might be changed to element Mg during the electrolysis.

3.3 Isotopic distribution ratio

By precise comparing the mass number of ^{41}K with that of $^{25}Mg^{16}O$, it is found that mass number 41 does not correspond to $^{25}Mg^{16}O$. The ratios of normalized intensities of ^{41}K to that of ^{39}K were obtained before and after electrolysis with those three Co samples. The ratios are given in Table 4. Natural abundance of ^{41}K divide by that of ^{39}K equals 0.072, which is shown as the natural ratio in the bottom of Table 4. Symbol "×" indicates the fail detection of ^{41}K. The ratios before and after electrolysis range 0.074—0.171 and 0.147—0.339, respectively. The value of natural ratio is fairly equals to those in the range obtained before electrolysis. However, the ratio after electrolysis is fairly larger than the natural one. It might mean that the reaction process for producing ^{41}K during the electrolysis is different from that of ^{41}K on the earth. In other words, the change in the ratio would indicate an evidence of anomalous nuclear reaction occurring on the Co electrode during electrolysis.

	Before	After
Co Sample1 (Quartz)	0.120	0.205
	0.077	0.147
	0.082	×
Co Sample2 (Polyethylene)	0.091	0.194
	0.171	0.251
	0.074	0.204
Co Sample3 (Quartz)	0.120	0.339
	0.077	0.307
	0.082	×
Natural	0.072	

Table 4 Ratio of the intensity for 41K to that for 39K

4. CONCLUSION

Elements Cr, Fe and Ni were commonly observed for both Au and Co electrolysis system. However, more marked increase of Fe and Cr were observed for Au than for Co cathode. The normalized intensity of SIMS count for Al decreased with that for Mg increased during the electrolysis. The ratio of the intensity of ^{41}K to that of ^{39}K was obtained, which gives different ratio from the natural vale.

The increasing and decreasing amount of elements in conjunction with change in natural isotopic abundance indicate a possible nuclear transmutation under the electrolysis. The results show that proton as well as deuteron could have an important role in nuclear reaction on metal solid.

5. REFERENCES

(1) J. Dash et al. , Fusion Tech. , Vol. 26, p. 299 (1994)
(2) T. Mizuno et al. , Proc. 7th Int. Conf. on Cold Fusion, p. 253 (1998)
(3) R. Bush and R. Eagleton, Fusion Tech. , Vol. 26, p. 344 (1994)
(4) T. Ohmori et al. , Fusion Tech. , Vol. 31, p. 210 (1997)
(5) T. Ohmori et al. , Fusion Tech., Vol. 33, p. 367 (1998)
(6) T. Mizuno et al., Proc. 8th Int. Conf. on Cold Fusion, p. 75 (2000)

UNEXPECTED DETECTION OF NEW ELEMENTS IN ELECTROLYTIC EXPERIMENTS WITH DEUTERATED ETHYL-ALCOHOL, PD WIRE, SR AND HG SALTS.

Francesco CELANI[1], A. Spallone[1], P. Marini[2], V. di Stefano[2], M. Nakamura[2], A. Mancini[3], G. D'Agostaro[4,1], E. Righi[1], G. Trenta[1], P. Quercia[5,1], C. Catena[4,1], V. Andreassi[1], F. Fontana[6], D. Garbelli[6], L. Gamberale[6], D. Azzarone[6], E. Celia[7], F. Falcioni[7], M.Marchesini[7], E. Novaro[7].

(1) INFN-LNF, Via E. Fermi 40, 00044 Frascati (Rome)–Italy; (2) EURESYS, Via Lero 30, 00129 Rome–Italy; (3) ORIM srl, Via Concordia 65, 62100 Piediripa (Mc)–Italy; (4) ENEA-Casaccia, Via Anguillarese 301, 00060 Rome–Italy; (5) ASL-RmH, Via E.Fermi 1, 00044 Frascati (Rome)–Italy; (6) Pirelli Labs S.p.A.,Viale Sarca 222, 20126 Milan-Italy; (7) Centro Sviluppo Materiali S.p.A., Via di Castel Romano 100, 00128 Rome-Italy.

Abstract: The insoluble powder recovered at the bottom of our electrolytic cell, after several electrolytic deuterium loading/deloading cycles, was analysed by an ICP-MS analyser. The electrolyte was constituted of a deuterated hydro-alcoholic solution; Sr and Hg salts were added to such a solution at micromolar concentration; the cathode was a long and thin Pd wire. The ICP-MS analyses of the insoluble powder were motivated from the recent results of Y. Iwamura and collaborators at Mitsubishi Heavy Industries-Researh Center (Yokohama, Japan) showing reproducible "transmutation" of Sr into Mo (isotopic composition different from natural one) and Cs into Pr, when a special multilayer Pd sheet was subjected to a prolonged Deuterium gas flowing. Some of our results look partially in agreement with Y. Iwamura report. Other unexpected elements were also detected with an isotopic distribution close to the natural one. The production of stable isotopes by *Selective Channel Photofission*, according to the model of A.Takahashi (Osaka University, Japan), can help for understanding. Further works, hopefully also from other Laboratories, are needed to clarify this kind of results.

Keywords: PdDx, electrolytic hydro-alcoholic solution, Pd thin-long wire, Sr and Hg salts, "transmutation".

1. INTRODUCTION

Large and unexpected amounts of some foreign elements (Fe, Ti, Cu, Zn...) have been recently found on the surface of proper metallic cathodes (e.g. Pd) when electrolysis is performed with D2O based electrolytes1,2). The quantity of such foreign elements is in general too high to be considered as impurities galvanically deposited on the cathode. Furthermore, the isotopic mass ratios of these foreign elements are significantly different from the natural ones. This fact, in particular, has been explained by assuming that some nuclear reactions occur when Deuterium (D) is adsorbed on or absorbed into the Pd cathode, as pointed out from Akito Takahashi3).

At present, the electrolyte employed in our experiments is typically constituted by a solution of, both heavy, ethyl alcohol/water (93:7 by volume) containing very small amounts of specific inorganic ions. Our loading procedure is based on a series of D loading/deloading cycles (i.e. the Pd wire is alternatively set as cathode and anode). After a certain number of loading/deloading cycles a ***black powder*** appears at the bottom of the cell as a precipitate. The main component of this powder has shown to contain Pd, probably as PdO, which is produced during the deloading phase of the cycle when the Pd wire is anodic. If some *foreign elements* are formed during the cathodic phase of the cycle (D loading), it is very probable they are mainly present on the surface where the D/Pd ratio is higher. Therefore, when the Pd wire surface is subsequently oxidised, some of the *foreign elements* may remain entrained within the black powder. Taking into consideration the pioneering work by T. Mizuno[1)] and G.H.Miley[2)] and in particular the recent, very

reliable and reproducible results obtained by Y. Iwamura[4], we decided to check the presence of *foreign elements* in the black powder by means of a high resolution ICP-MS analyser.

2. EXPERIMENTAL CONDITIONS.

As reported in recent papers (ICCF8, JCF3, ICCF9), we adopt the following experimental conditions:

a) Electrolytic solution: 750ml, heavy ethyl alcohol (C_2H_5OD) and heavy water (D_2O) mixture (93:7 by volume).

The following salts and acids have been added to this kind of solution: $SrCl_2$:3–10*10^{-5}moles; $HgCl_2$:2–3*10^{-5}moles; D_2SO_4: 1–2*10^{-5}moles; DCl: 1--10*10^{-5}moles; $Ba(OH)_2$: 0--1*10^{-5}moles.

b) Electrodes: Cathode: Pd wire (l=60cm, ϕ=50μm), U-shaped so as to be contained into a borosilicate glass 3.3 (EU standard GH1), graduated cylinder (l=40cm, ϕ=5cm); Anode: U-shaped Pt wire (l=60cm, ϕ= 0.5mm);

c) Electrolysis operating condition: DC@10mA, Anode-Cathode distance and Voltage: 5cm, 50—250V;

d) Loading measurement (wire electrical resistance method): Pd wire electrical resistance measured trough the voltage drop, along the Pd wire, produced by AC current (10kHz, square wave) of 18mA ($J=1000A/cm^2$).

e) Solvent components of the solution (C_2H_5OD, D_2O) are vacuum distilled (45°C) and on line filtered (100nm, MILLIPORE type VVLP, PTFE filter): properply modified, by us, Rotavapor system (model R-134 BÜCHI). These operations allow for:

1) *control* over the composition of the electrolyte (necessary because of the very low concentrations of the electrolytes added, typical of our method) and strong reduction of all the impurities normally dissolved in the two liquids. Such impurities, even if present in very small amount, could be galvanically accumulated on the cathode and be mistaken for *foreign elements*. After the double distillation procedure the electrical conductivity of the two solvent components of the electrolytic solution was reduced from about 100μS to less than 1μS, for D_2O, and from 2μS to 0.05μS, for C_2H_5OD, respectively. As a reference, typical distilled H_2O, in the same specific experimental conditions of measurement, shows a conductivity of about 3μS. In particular, a strong reduction of $KMnO_4$ and Iron ions, usually present in heavy water, is required: the presence of such substances significantly inhibits the D-loading, ensuing in lower D/Pd ratios;

2) *elimination* of the two new species of bacteria (*Ralstonia* and *Stenotrophomonas detesculanense*), discovered by us in D_2O in 1999[5]. We experienced that such bacteria negatively affect the D/Pd loading[6].

3. EXPERIMENTAL RESULTS.

By adopting the above experimental conditions, during the D-loading phase (Pd is cathode) a thin coating containing Hg, Pt and Sr sulphate is formed on the Pd wire surface. Pt ions (a drawback because they lower the cathodic overvoltage) are produced because of the anodic corrosion of the Pt wire. Pt metal is galvanically deposited on the Pd wire, together with Hg. Sr ions, because of the local alkalinization due to the cathodic D^+ discharge, precipitate as $SrSO_4$ on the cathodic surface. Such a coating, which basically characterises our D loading method, significantly increases the cathodic overvoltage of the Pd wire. R/Ro values<1.7, at 25°C, (D/Pd>0.93) can currently be achieved[7].

During the deloading phase of the cycle (Pd wire as an anode) the coating and a consistent amount of Pd (probably as PdO) detaches from the wire and precipitates as a black powder. Accordingly, it was found that Pd, Pt, Hg, and Sr are the main constituents of such a precipitate.

Y. Iwamura and co-workers reported[4] that Sr, electrochemically applied on a multi-layer Pd sheet, was progressively and surprisingly "transmuted" into Mo when D gas was forced to flow through the multi-layer sheet. Taking into consideration that a thin layer of Sr is also present in our Pd cathodes, we thought that our procedure, even if consistently different from that of Y. Iwamura, might allow for a reproduction of their results.

In the Y. Iwamura experiment a low work-function material (e.g. CaO) is sputtered together with Pd on a Pd sheet so as to form a 1000Å layer. The presence of a low work-function material seems to be essential for the Sr→Mo "transmutation". On the other hand, as pointed out by A. Takahashi and co-workers (**JCF4-22,** in press), such nuclear reactions in the D-Pd system should presumably occur in sites where the D/Pd ratio is particularly high, that is at the CaO-Pd-Sr interface. *Now, considering the much higher loading ratio currently achieved by our electrolytic technique, with respect to those allowed for by the gas loading procedure, it is possible that the Sr→Mo "transmutation" also can occur on our cathode and therefore that Mo be present in the black powders found at the bottom of our electrolytic cell.*

4. ELECTROLYTIC DEUTERIUM LOADING/DELOADING CYCLES

The Pd wire and the components of the electrolyte (D_2O; C_2H_5OD; $HgCl_2$; $SrCl_2$; D_2SO_4; $Ba(OH)_2$) were previously ICP-MS analysed in order to account for their impurities content with particular attention to the presence of Mo. Two experiments have been performed with two different Pd wires, under the following loading conditions: electrolytic current: 10mA; temperature: 26°C; time: 24--96h. Best R/Ro

obtained at the end of the loading phases: experiment #1: R/Ro=1.68; experiment #2: R/Ro=1.74.

Deloading phase. Electrolytic current=2mA, for about 2 hours. (temperature: 25°C). When a R/Ro value of 1.1 is reached, the current is raised to 10mA for about 10 minutes. The latter procedure is necessary for a complete deloading of the Pd wire. We observed, after some loading/deloading cycles, that a significant residual stress remains on the Pd wire (i.e. the minimum R/Ro after deloading was higher than the starting one). We noted that the amount of residual *stress (0.2-4%) increased more when an higher loading value was achieved during the D loading phase.*

Both the experiments reported in this paper consisted in five D loading/deloading cycles and the total time was about 2 weeks. In experiment #1 the black powder, deposited at the bottom of the cell, was collected together with 100cc of solution, evaporated to dryness, solubilized by aqua regia and submitted to ICP-MS analysis. In experiment #2 only the solution was collected, evaporated to dryness and solubilized by aqua regia for ICP-MS analysis.

5. ICP-MS RESULTS

The analyses were performed at the Laboratories of "Centro Sviluppo Materiali" by a high resolution ICP-MS instrument (HP&YOKOGAWA Analytical Systems, model 4500, 1996) calibrated at "low power plasma" in order to reduce possible spectroscopic interference's (polyatomic, oxide, and doubly charged ions), apart isobaric.

Calibration factor: 1count=$6*10^{10}$atoms. All the counts, reported in the following tabels, have been corrected for all the "blanks" and the interference effects, if any. Detection limit: $6*10^{11}$atoms. In the tabels are reported the counts pertinent to the suggested isotopes for ICP-MS analysis and selected for reference and their natural percent abundance. In some cases and in particular for the main constituents of the black powder we were forced to use isotopes different from ones suggested because of instrumental overflow.

Element:	^{23}Na(100)	^{47}Ti(7.3)	^{55}Mn(100)	^{57}Fe(2.2)	^{63}Cu(69.2)	^{66}Zn(27.9)	^{88}Sr(82.6)	^{93}Nb(100)	^{98}Mo(24.1)
Counts:	$1.2*10^5$	30	400	< 10	$7.2*10^3$	760	$7.6*10^3$	110	26

Tab. **5.1a)** Typical impurities in heavy ethyl-alcohol/water (93:7 by volume), 100ml, after re-distillation.

Element:	^{47}Ti(7.3)	^{57}Fe(2.2)	^{66}Zn(27.9)	^{90}Zr(51.5)	^{93}Nb(100)	^{98}Mo(24.1)	^{137}Ba(11.2)
Counts:	$6.2*10^3$	$2.0*10^3$	< 10	490	204	32	$1.2*10^4$

Tab. **5.1b)** Analysis of $SrCl_2$. ^{84}Sr(0.56): $1.4*10^7$ counts.

Element:	^{47}Ti(7.3)	^{57}Fe(2.2)	^{66}Zn(27.9)	^{88}Sr(82.6)	^{90}Zr(51.5)	^{93}Nb(100)	^{98}Mo(24.1)
Counts:	6310	$1.3*10^3$	400	$7.2*10^3$	380	10	80

Tab. **5.1c)** Analysis of $HgCl_2$. ^{202}Hg(29.9): $5.8*10^6$ counts.

Element	^{47}Ti(7.3)	^{57}Fe(2.2)	^{63}Cu (69.2)	^{66}Zn(27.9)	^{90}Zr(51.5)	^{93}Nb(100)	^{98}Mo(24.1)
Counts:	120	200	$2.4*10^3$	<10	$8.9*10^3$	< 10	11

Tab. **5.1d)** Analysis of the virgin Pd wire. ^{102}Pd(1.0): $7.0*10^6$ counts (about 30cm of wire).

Fe	Ir	Na	Pd	Cu	Ca	Re	Mg	Rh	Al	Zr	Ti	Mn	Cr	Au
20	9.1	9.0	7.3	5.1	4.2	3.4	3.2	3.2	2.8	6.9	1.1	0.2	1.3	1.9

Tab. **5.1e)** Analysis of the Pt wire (ICP-MS assay performed by the Pt supplier). Impurities in ppm.

Element:	^{102}Pd (1.0)	^{195}Pt (33.8)	^{84}Sr (0.56)	^{204}Hg (6.9)	^{138}Ba (71.7)
Counts:	$2.3*10^6$	$1.5*10^6$	$1.1*10^6$	$7.2*10^6$	$2.3*10^5$

Tab. **5.2** Main constituents in the Experiment #1, ***black powder***

Element:	^{47}Ti(7.3)	^{57}Fe(2.2)	^{63}Cu (69.2)	^{66}Zn(27.9)	^{90}Zr(51.5)	^{93}Nb(100)	^{98}Mo(24.1)
Counts:	$1.5*10^4$	$3.0*10^5$	$8.7*10^3$	$2.4*10^4$	$4.6*10^4$	$5.6*10^5$	$3.4*10^3$

Tab. **5.3** ***Other elements*** **(unexpected)** in the Experiment #1, ***black powder.***

* We inform that Ti, Fe, Zn, Nb, for cross check purposes, were also analysed, because of their relevant amount. by means of another less sensitive analytical tecnique: ICP-OES analysis (Perkin-Elmer, model OPTIMA3300 XL-DV, 2000). Sensitivity: ≈10ppb (about 1000 times lower than ICP-MS).

* We inform that we made other analysis on *Pd wires* before and after electrolysis by SEM-EDAX instrument (at Pirelli Labs). In some "spot areas" of after electrolysis wires, "new" elements like Ti, Fe, Zn were detected.

6. COMMENTS ON THE ELEMENTS IN TAB. 5.3

Each of them shows relevant excess counts with respect to the values of "the blank" obtained by summing up the contributions taken from Tab. 5.1a) to Tab. 5.1e), properly "weighed" for the amount used in the experiment, as detailed in § 2 . The anomalous presence of Ti, Cu, Fe, and Zn, has been reported by other researches[1,2)]. The presence of Mo seems to align with the results of Y. Iwamura. At present it is not known to us if Nb, which was found in the black powder at relatively remarkable amount, has been reported in the literature as *foreign elements*. Having assessed the relevant excess amount of the elements shown in paragraph 5.3, we turned to the examination of their isotopic distribution. We found that the isotopic distributions of Ti, Cu, Fe, Zn and Zr were very close to the natural one. Accordingly, it would be concluded, in spite of their relevant amount, that the presence of these elements in the black powder was due to a contamination. *At present, we cannot explain the origin of such a heavy contaminationy.*

Mass, Nat. Ab.	92(**14.8**)	94(**9.3**)	95(**15.9**)	96(**16.7**)	97(**9.6**)	98(**24.1**)	100(**9.6**)
Coun. New ab	2771(**16.4**)	3097(**18.4**)	2044(**12.1**)	2703(**16.0**)	1319(**7.8**)	3461(**20.5**)	1327(**8.7**)

Tab.**6.1** Isotopic distribution of Mo in black powder, Exp.#1 (Mass&Nat. abundance/Counts&New abundance).

The counts from the mass number 92 to 100 can be attributed to a some Mo contamination in the black powder. However, a significant deviation of the isotopic distribution from the natural one appears at the mass number 94 (natural abundance: 9.3%; found: 18.4%). Such a deviation could be explained by supposing that some foreign ^{94}Mo was "produced" during the electrolysis. The amount of our foreign Mo (expressed as atoms/cm^2) is similar to that found by Y. Iwamura, but the mass number is different (94 versus 96). At present no satisfactory explanation of such a discrepancy is available.

7. ICP-MS analysis of residue obtained after distillation of electrolytic solution.

In the electrolytic solution, after distillation, we have recovered (in consistently lower amounts), the same elements previously found in the *black powder*. No relevant anomalies in the isotopic distribution were detected even for Mo. Isotopic distribution was as following:

Mass, Nat. Ab	92(**14.8**)	94(**9.3**)	95(**15.9**)	96(**16.7**)	97(**9.6**)	98(**24.1**)	100(**9.6**)
Coun. New ab	1600(**13.4**)	1190(**10.0**)	1870(**15.7**)	1940(**16.2**)	1150(**9.6**)	3020(**25.3**)	1138(**9.6**)

Tab. 7 Isotopic distribution of Mo soluble, Exp. #2 (Mass&Nat. abundance/Counts&New abundance).

8. CONCLUSIONS

Several, unexpected, new elements were detected after loading/deloading electrolytic cycles in the above mentioned experimental conditions. Most of these elements haave been collected in the insoluble *black powder* that precipitates during the anodic phase of the cycle. Among such foreign elements, Ti, Fe, Zn, Nb were found to be the most abundant components. All of these show an isotopic distribution close to the natural one, so some sort of contamination, at present not yet identified, can not be rouled out. Regarding the presence of Mo, we found that a clear isotopic anomaly occurs at the mass number 94, and not at mass 96 as reported by Y. Iwamura. Further work is necessary: in order to reconfirm our results and to explain the differences with respect to the Y. Iwamura experiments.

Acknowledgment:

* We would like to notify that Dr. Naoto Asami and Prof Kazuaki Matsui, now at Institute of Applied Energy of Tokyo (Japan), *were the first people that realised about NON-inorganic pollution of heavy water during Cold Fusion experiments* (NHE Project, 1999, Sapporo, Japan): their observations were for us starting points for further analysis and stimulated us to strong changing of experimental set-up.

* We are indebted to Prof. Piergiorgio Sona at CESI (Milan, Italy) because very long, stimulating discussions and warnings about our, unusual, experimental set-up and electrolytes.

* We deeply thank Prof. Akito Takahashi (Osaka Univ.), because useful suggestions and criticism related to the experimental set-up and *invaluable help* on *data analysis* about the *new elements* that seems have been found.

References:

1) T. Mizuno et al.: Denki Kakagu **64** (1996) 1160 (in Japanese).
2) J. Miley et al. :J. New Energy **1** (1996) No.3, 5.
3) A. Takahashi et al. Jpn. J. Appl. Phys. **40** (2001) 7031 and ICCF9 (in press).
4) Y. Iwamura et al. Jpn. J. Appl. Phys. **41** (2002) 4642 and ICCF9 (in press).
5) D'Agostaro, G.A.F., Celani, F.J.V.A., (.....) and Nakamura, M.: National Centre Biology Information: LOCUS: AF280433;1537 bp DNA linear BCT 19-JAN-2002, DEFINITION: *Ralstonia detusculanense;* ORGANISM: Ralstonia detusculanense Bacteria; Proteobacteria; beta subdivision; Ralstonia group; Ralstonia. Submitted 20-JUN-2000 http://www.ncbi.nlm.nih.gov; **5a)** D'Agostaro, G.A.F., Celani, F.J.V.A., (....) and Nakamura, M.: National Centre Biology Information: LOCUS: AF280434; 535 bp DNA linear BCT 19-JAN-2002 DEFINITION: *Stenotrophomonas detusculanens;* ORGANISM: Stenotrophomonas detusculanense Bacteria; Proteobacteria; gamma subdivision; Xanthomonas group; Stenotrophomonas. Submitted 20-JUN-2000 http://www.ncbi.nlm.nih.gov.
6) F.Celani, A.Spallone et al.:"High hydrogen loading into thin palladium wires through precipitate of alkaline-earth carbonate on the surface of cathode: evidence of new phases in the pd-h system and unexpected problems due to bacteria contamination in the heavy water.",Proceedings of the "8th International Conference on Cold Fusion", Lerici, Italy 21-26 May 2000; - Conf. Proc. Vol. 70 pg 181-190 Edited by F. Scaramuzzi; Compositori– SIF, Bologna, 2000; Italy. ISBN 88-7794-256-8
7) F.Celani, A. Spallone et al.: "Electrochemical H-D loading of Palladium wires by hydro-alcoholic electrolytes related to the new discovered *Ralstonia* bacteria into heavy water"., **JCF3-5,** 3rd Meeting of Japan CF_Research Society, October 25-26, 2001; Yokohama National University. http://fomcane.nucl.eng.osaka-u.ac.jp/jcf/.

Positive and negative energy evolution and new element production in critical electrolysis with Palladium electrode in K_2CO_3/H_2O solution

T.Ohmori, S.Narita*, H.Yamada*, T.Mizuno** and Y.Aoki**

Catalysis Research Center, Hokkaido University
* Department of Electrical and Electronic Engineering, Iwate University
** Graduate School of Engineering, Hokkaido University

ABSTRACT

Positive and negative energy evolution was observed in the H_2O electrolysis with two types of Pd electrodes. The positive energy (excess energy) was in the range from 2 to 12 W, being observed with all the untreated Pd and a few cold worked Pd electrodes. The negative energy (endothermic reaction) was -3 – 0 W, being observed with most of the cold worked Pd electrodes. Among the cold worked electrodes evolved negative energy, one cold worked electrode generated negative energy almost over the whole period of the electrolysis, the other electrodes generated positive energy along with negative one. Fe, Sn, Cd and Zn were detected with the untreated and cold worked electrodes generated positive energy while Pt, Au, Hg and Pb were detected with the cold worked electrodes generated negative energy. The isotope distribution of Pd atoms in the neighborhood of the electrode surface was disturbed to a great extent. The isotope distributions of product atoms of Pt and Hg were also deviated from the natural isotopic abundance.

1. INTRODUCTION.

According to the previous work [1], it is expected that excess energy evolved during the electrolysis in H_2O and D_2O solutions increases with electrolysis current density. We recently observed several 10 W of excess energy during plasma electrolysis with use of W and Re electrodes [2-4]. However, in plasma electrolysis, the effective duration of the electrolysis was limited to 10 or 20 minutes because of the high heat of the violent reaction disintegrates the electrode material.

In the present study we tried to measure excess energy and analyze new elements produced on two types of Pd electrodes during electrolysis at an extremely large current density, just below the threshold value at which plasma electrolysis occurs (we refer to this as critical electrolysis).

2. EXPERIMENTAL

We used two types of Pd electrodes. One is an untreated Pd sheet and the other is a cold worked Pd sheet prepared by way of scraping its surface with a cleaned Pyrex-glass fragment. The electrode area is ca. 0.8 cm^2. The counter electrode is a Pt gauze (1 cm × 7 cm, 80 mesh). The electrolytic cell is made of fused quartz glass. The volume is 240 ml. Electrolyte solution is 2 M K_2CO_3 prepared from Merck sprapur reagent and Milli-Q water. The volume is 220 ml in the maximum condition. Electrolysis was conducted for 20 days.

The element and isotope analysis in the electrode surface layers after the critical electrolysis was carried out by Auger electron spectroscopy (AES) and Time of flight-type secondary ion mass spectroscopy (TOF-SIMS).

3. RESULTS AND DISCUSSION

3-1 Excess energy measurement

During electrolysis, every 12 hours the volume of the electrolyte solution decreased to ca. 120 ml by the decomposition and vaporization of H_2O. Milli-Q make-up water was supplied every 12 hours on most days. When make-up water was added the solution temperature dropped. After it recovered heat measurement was conducted for 6-8 h, while the solution volume remained above 160 ml. Excess energy, E_{ex}, was estimated by the following equations,

$$E_{ex} = W(T)_{cal} - (E - 1.48)I \quad (1)$$

$$W(T)_{cal} = W(T)_{T=220\text{-}190} - \kappa \Delta V \quad (2)$$

where $W(T)_{cal}$, E, I, $W(T)_{T=200\text{-}190}$, ΔV, and κ are, respectively, electric power calculated from the calibration curve shown in Fig.1, input potential, electrolysis current, electric power calculated from the calibration curves obtained in solutions above 190 ml, the volume of decrease of solution from 190 ml, and a correction factor

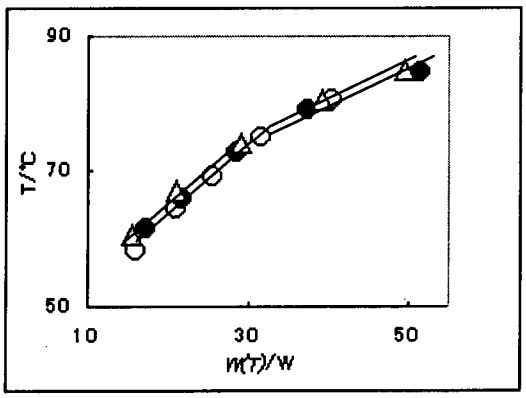

Figure 1. Calibration curves: solution volume (○) 220 ml, (●) 190 ml, (△) 160 ml

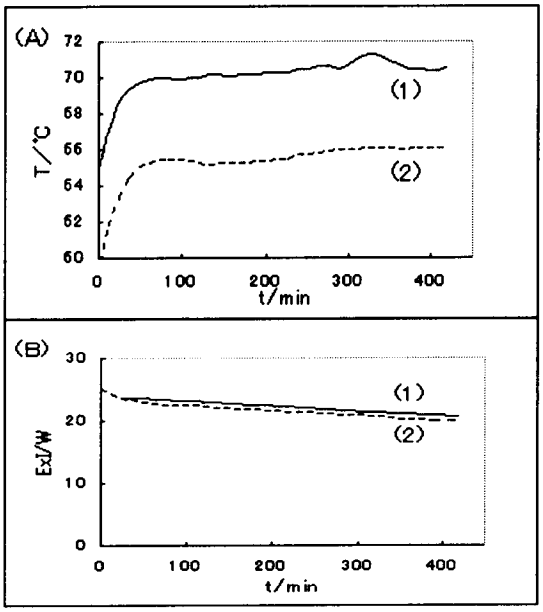

Figure 2. Variations of solution temperature (A), and input electric power (B), with electrolysis time obtained from 18350 min after starting electrolysis: (1) untreated electrode (electrode 114), (2) cold worked electrode (electrode 113)

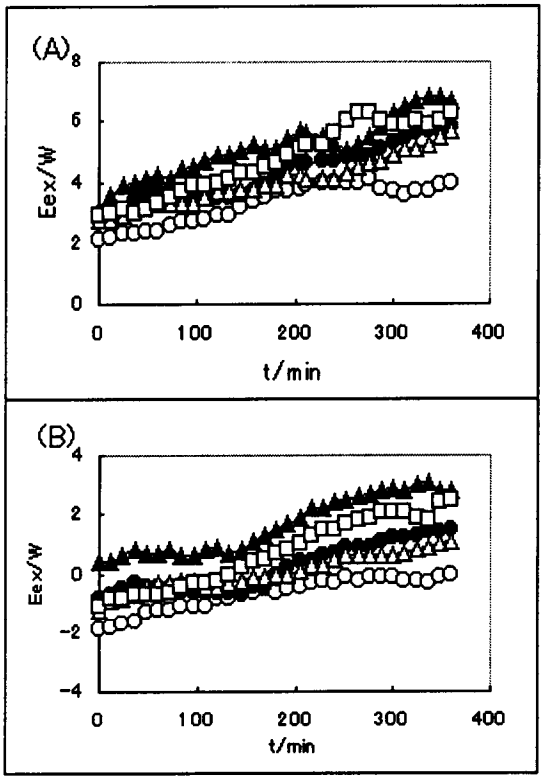

Figure 3. Positive and negative energies observed in the various time regions after starting electrolysis for (A) untreated electrode (electrode 114) and (B) cold worked electrode (electrode 113): (○) 3945, (●) 9665, (△) 18350, (▲) 25540, (□)29870 min after starting electrolysis

required for when the volume of solution decreased to less than 190 ml. The correction factor is 0.063-0.087 W/ml, based on the assumption that the deviation of the calibration curve, which begins to appear below 190 ml, is proportional to ΔV.

Figure 2 shows an example of the heat measurement during electrolysis with two cathodes: a fresh cold worked electrode, and a fresh untreated electrode prepared from the same Pd sheet, electrolyzed at almost the same power level. In both electrolyses fresh Pt gauzes prepared from the same material were employed as counter electrodes. A clear difference in the temperature of solution is seen between the two systems. The temperature of the cell with the fresh untreated electrode was 70 -71℃, or ca. 5℃ higher than the cell with the fresh cold worked electrode. Even from this simple example, it is clear that excess energy evolved at least on the fresh untreated Pd electrode in the critical electrolysis. In fact, the excess energy estimated from this figure amounts to 2.8 – 5 W for the untreated electrode and -1 – 1 W for the cold worked electrode, namely, negative energy was observed over certain periods during electrolysis with the latter electrode. It is evident that such a difference in the energy evolution depends on whether the electrode is subjected to cold work treatment or not. Figure 3 shows the excess energies observed with these electrodes in the various time regions after as many as 20 days of electrolysis (28000 minutes). For the untreated Pd electrode considerable amounts of excess energy ranging from 2 to 6 W were always observed. The excess energy increased steadily with the electrolysis in times after make-up water was added. Whereas for the cold worked Pd electrode both "positive" excess energies and "negative" excess energy (hereafter, we will refer to these energies merely as "positive energy" and "negative energy", respectively) were observed. Within 3 days after starting electrolysis, the energy is always negative (endothermic), after which it passes through 0 and turns positive with increasing time.

In the present study excess energy measurement was performed with use of seven cold worked electrodes and six untreated Pd electrodes. For the untreated Pd electrodes positive energies ranging from 2 to 12 W were observed without exception. On the other hand, for the cold worked electrodes, both positive and negative energies were observed for four electrodes, negative energy alone for one electrode, and positive energy alone for the residual two electrodes. Figure 4 shows negative energies observed with the cold worked electrode evolved almost negative energy alone (for convenience, it will be referred to as "electrode evolved negative energy alone"). The negative energy reaches ca. - 2 W within 2 h after the onset of the measurement. The observation of positive and negative energies suggests that two types of nuclear transmutations, i.e. exothermic and

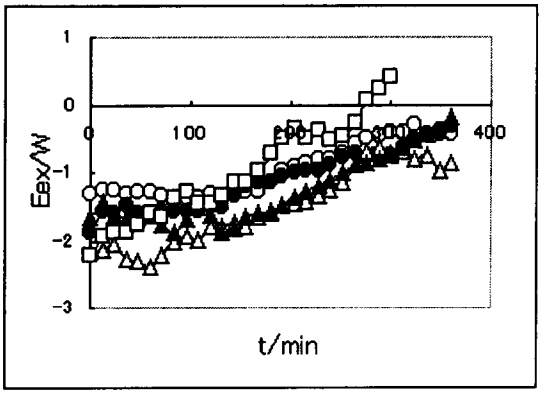

Figure 4. Negative energies observed in the various time regions after starting electrolysis for a cold worked electrode (electrode 108): (○) 1415, (●) 10100, (△) 19770, (▲) 20175, (□) 28855 min after starting electrolysis

endothermic, can occur on the cold worked electrode and their pathway is likely to depend on the condition of the crystallographic disturbance of the electrode induced by the cold work treatment.

3-2 Identification of product elements

The element analysis on the electrode after the critical electrolysis for 20 days was made by AES. Figure 5 shows AES spectra obtained for three types of electrodes, i.e. untreated electrode, cold worked electrode evolved both positive and negative energies, and that evolved negative energy alone. The kinds of elements produced on/in these electrodes depended on whether the energy evolved was either positive or negative, or both. For the cold worked electrode evolved negative energy alone shown in Fig. 4 only a strong Pt signal was detected. For the untreated electrode that evolved positive energy alone, the major signals were Fe and K and, in addition, small signals of Sn, Cd and Zn were detected. Similar product elements were detected for two cold worked electrodes that evolved only positive energy. However, to our surprise, no Pt signal was detected for electrodes that evolved positive energy. For the cold worked electrodes evolved both positive and negative energies strong Pt signal and weak Fe signals were detected.

The distribution profiles of the product elements in the bulk of the cold worked electrode that evolved only negative energy and the untreated electrode obtained by AES spectra are shown in Fig.6. The surface concentration of Pt produced on/in the former electrode reaches ca. 90 at. % which decreases nearly linearly with sputtering time, becoming close to 0 at around 4.5 min. On the other hand, for the latter electrode Fe is mainly distributed (22 at. % is the maximum), and it also becomes negligible at around 4.5 min. The maximum concentration of Sn and Zn are 7 at. % and of Cd is 1 at. %. K is distributed only in the vicinity of the electrode surface. No Pd is found in the layers close to the surface of the electrode. Moreover, for this electrode, O is

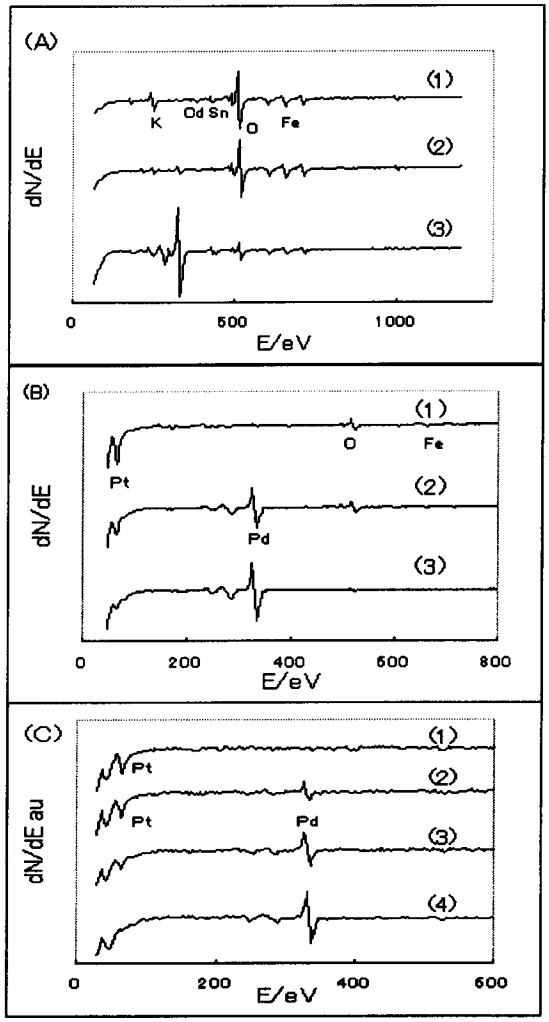

Figure 5. AES spectra of untreated electrode (electrode 114) (A), cold worked electrode evolved both positive and negative energies (electrode 113) (B) and cold worked electrode evolved negative energy alone (electrode 108) (C). Sputtering time (A) (1) 0, (2) 0.5 min, (3) 1 min, (B) (1) 0, (2) 5 min, (3) 9 min, (C) (1) 0, (2) 1 min, (3) 2 min, (4) 4 min

present in large amounts. It is probably bound to Fe, Zn, Sn and Cd atoms, hence the real concentration of these elements should be somewhat higher than those estimated from Fig.6. The depth of the face of the electrode obtained by sputtering for 4 minutes was estimated at 250 ± 30 mono-layers by use of the equation described in [5]. Therefore, the approximate amounts of Pt produced on/in the cold worked electrode and Fe produced on/in the untreated electrode yield, respectively, $(2.0\pm0.5) \times 10^{17}$ atom and $(3.2\pm0.5) \times 10^{16}$ atom.

Along with the production of Pt a considerable amount of Au (12-14 % of Pt) was produced. This was confirmed on/in the cold worked electrodes evolved negative energy by TOF-SIMS analysis (in the AES spectra the signal of Au was not identified by the strong Pt signal). As an

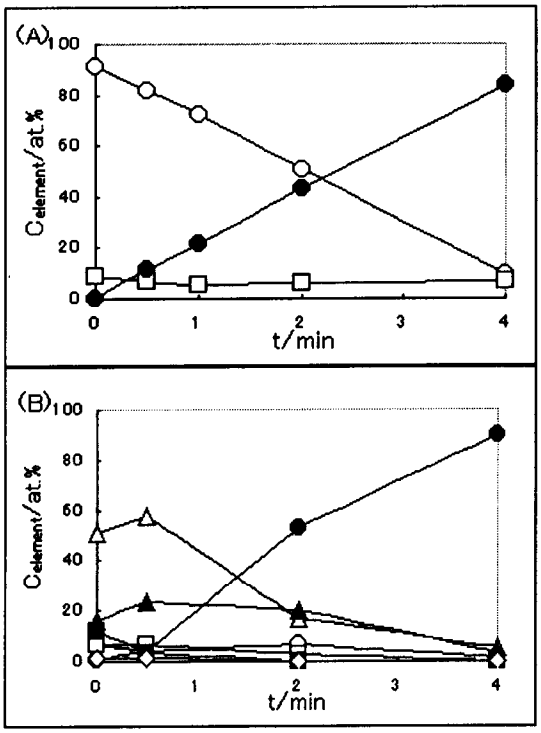

Figure 6. Distribution profile of product elements in the bulk of the electrode after electrolysis, (A) cold worked electrode evolved negative energies alone (electrode 108), (○) Pt, (●) Pd, (□) O, (B) untreated electrode (electrode 114), (○)Sn, (●) Pd, (△) O, (▲) Fe, (□) Zn, (■) K, (◇) Cd

example, the signals of TOF-SIMS detected in the mass numbers ranging from 194 to 198 for the cold worked electrode that evolved only negative energy are listed in Table 1. One can see that the electrode retains Au as much as 14 % of Pt. The fact that an appreciable amount of Au is produced along with Pt suggests that Pt atoms found in the cold worked electrode do not come from the counter electrode but are newly produced during the critical electrolysis.

3-3 Isotope distribution of Pd and Pt atoms

The isotope distribution of Pd atoms in the surface layers of the electrode after the critical electrolysis was markedly different from its natural isotopic abundance. In addition, Pt atoms produced on/in the cold worked electrodes that

TABLE 1
TOFF-SIMS Signal Intensities of Pt and Au (electrode 108)

Signal mass	Count	Element	Difference between signal and element masses
193.9629	3640	194Pt	< 0.001
194.9677	6224	195Pt	0.003
195.9673	4165	196Pt	0.002
196.9758	2563	197Au	0.008
197.9734	1688	198Pt	0.006

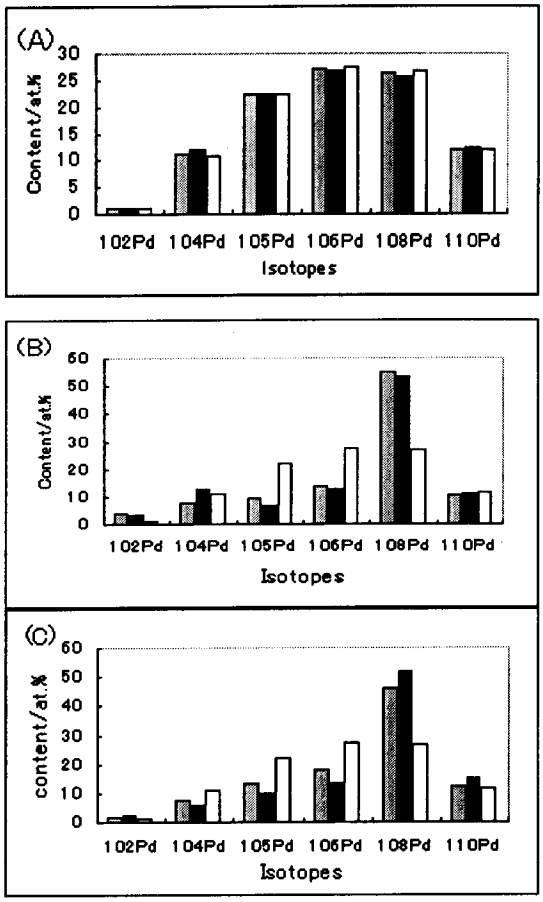

Figure 7. Isotopic distribution of Pd atoms in the surface layers of the electrodes, (A) fresh cold worked electrode before use, sputtered for 30 s, (B) cold worked electrode evolved negative energy alone, sputtered for 30 s (electrode 108), and (C) cold worked electrode evolved both positive and negative energies, sputtered for 120 s (electrode 107). In each three sets of the bars the left and middle bars show found values at the different spots of the electrode and the right bar shows natural isotopic abundance.

evolved negative energy alone and those that evolved positive and negative energies have anomalous isotope distribution. Figure 7 shows the isotope distribution of Pd atoms in the surface layers of these electrodes and fresh cold worked electrode before use. The isotope distribution of Pd of the fresh electrode is very close to the natural isotopic abundance. Whereas the contents of ^{108}Pd for the electrode evolved negative energy alone and that evolved both positive and negative energies increase pronouncedly, being ca. 2 times its natural isotopic abundance. The abundance of ^{105}Pd, ^{106}Pd and ^{110}Pd decreases. For Pt atoms, the content of ^{194}Pt falls to ca. 3/4 of its natural isotopic abundance, while the other Pt isotopes are above their natural values (Fig. 8). Besides Pt and Au, small amounts of Hg and Pb are detected by TOF-SIMS. The isotope distribution of Hg atoms was markedly deviated from its natural isotopic abundance (the content of ^{202}Hg observed

was below 2 at %), while the isotope distribution of Pb was close to its natural isotopic abundance. The analysis of the isotope distribution of Pd and product elements for untreated Pd electrodes is presently under way (in the preliminary experiments the result similar to that shown in Fig. 7 has been obtained).

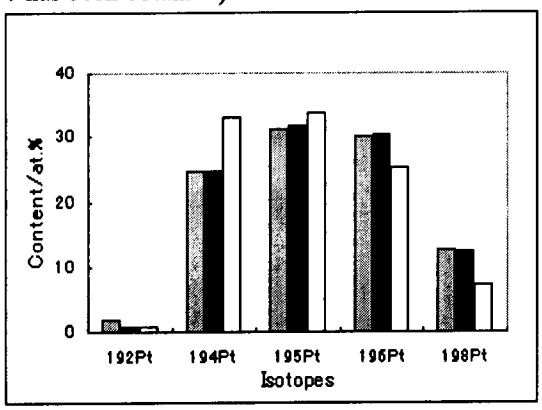

Figure 8. Isotopic distribution of Pt atoms present in the surface layers of the cold worked electrode evolved negative energy alone (electrode 108, no sputtered). In each three sets of the bars the left and middle bars show found values at the different spots of the electrode and the right bar shows natural isotopic abundance

3-4 Reaction routes

It is evident from the results obtained (1) that positive and/or negative energies evolve depending on whether the electrode is subjected to a cold worked treatment or not, (2) that Fe, Sn, Cd and Zn are produced for untreated electrodes and cold worked electrodes that evolved positive energy alone, (3) that Pt, Au, Hg and Pb are produced for cold worked electrodes that evolved negative energy alone, (4) that a small amount of Fe is produced in addition to Pt, Au, Hg and Pb for cold worked electrodes that evolved both positive and negative energies. Possibly, for the untreated electrodes, Pd atoms would interact with several H atoms to form Sn or Cd initially which disintegrate to form Fe or Zn. These processes should be exothermic, generating positive energies. On the other hand, for the cold worked electrodes evolved negative energy, two Pd atoms would interact with each other to form Pb initially, which in turn disintegrate to form Pt, Au and Hg. In this case the former endothermic fusion reaction would generate a negative heat balance.

However it should be noted that these phenomena are observable only on the Pd electrode under critical electrolysis. For a Pd electrode under the conventional electrolysis, for example, at a current density of 1 A/cm^2, the excess energies evolved is in the range from 0 to 0.6 W far smaller than those observed in the present study and no negative energy was observed [1,6]. In addition, the isotope distribution of Pd on the electrode after the electrolysis remained at natural isotopic abundance.

The anomalous isotope distribution of Pd of the electrode material and Pt, and the presence of Au, Hg and Pb, which are not significant contaminants in the electrolysis system, suggests strongly the occurrence of the endothermic nuclear transmutation under the critical electrolysis with the cold worked Pd electrode. The production of Fe, Sn, Cd, and Zn characteristic in the critical electrolysis with the untreated electrode and a few cold worked electrodes evolved positive energy alone reveals the occurrence of the exothermic nuclear transmutation.

REFERENCES

1. T.Ohmori and T.Mizuno, (1997) Current Topics in Electrochemistry, Vol.5, J.O'M. Bockris, E.J.Cairns, M.Froment, Z.Galus, Y.Ito, R.F.Savinell, Z.W.Tian, S.Trasatti and T.J.VanderNoot (Eds.), Re search Trends Trivandrum, 33-70
2. T.Ohmori and T.Mizuno, Proceedings of the 7-th International Conference on Cold Fusion, Vancouver, 279 (1998).
3. T.Ohmori and T.Mizuno, J.New Energy, **4**, 66 (2000).
4. T.Ohmori, (2000) Current Topics in Electrochemistry, Vol.7, J.O'M.Bockris, F.J.Cairn, M.Froment, Z.Galus, Y.Ito, R.F.Savinell, Z.W.Tian, S.Trasatti and T.J.VanderNoot (Eds.), Research Trends, Trivandrum, 101-118.
5. T.Ohmori, M.Enyo, T.Mizuno, Y.Nodasaka and H.Minagawa, Fusion Technology, **31**,210 (1997).
6. T.Ohmori, T.Mizuno, K.Kurokawa and M.Enyo, Int.J.of The Soc. of Mat. Eng. for Resources, **6**, 35 (1998).

Confirmation of anomalous hydrogen generation by plasma electrolysis

Tadahiko Mizuno, Tadashi Akimoto and Tadayoshi Ohmori
Hokkaido University, Kita-ku Kita-13 Nishi-8, Sapporo 060-8628, Japan
E-mail: mizuno@qe.eng.hokudai.ac.jp

Abstract: Direct decomposition of water is very difficult in normal conditions. Hydrogen gas is usually obtained by the electrolysis. Pyrolysis decomposition of water occurs at high temperatures, starting at ~3000°C. As we have already reported, anomalous hydrogen is sometimes generated during plasma electrolysis. Excess hydrogen usually appears once certain difficult conditions during high temperature glow discharge electrolysis are met. Here, we show that anomalous amounts of hydrogen and oxygen gas are generated during plasma electrolysis excess gas generation, presumably from pyrolysis. This is indirect proof that exceptionally high temperatures have been achieved. (Direct measurement of the reaction temperature has proved difficult.) Continuous generation of hydrogen above levels predicted by Faraday's law is observed when temperature, current density, input voltage and electrode surface meet certain conditions. Although only a few observations of excess hydrogen gas production have been made, production is sometimes 80 times higher than normal Faradic electrolysis gas production.

Key word: plasma electrolysis, hydrogen generation, current efficiency

1. Introduction

We previously reported anomalous hydrogen generation during plasma electrolysis [1,2]. Some researchers have attempted to replicate the phenomenon, but it is difficult to generate large excess hydrogen. Usually, the plasma state can be achieved fairly easily when voltage is increased to at least 140V at a high electrolyte temperature. Several researcher have tried to replicate tend to raise input voltage very high, to several hundred volts. But they have observed no excess hydrogen even at such high voltage, because they have not achieved the other conditions we specify.

During plasma electrolysis, so much vapor and the hydrogen gas are released from the cell that it becomes difficult to determine the heat balance. Measuring the enthalpy of the effluent gas is particularly difficult and complicated, and it has not been done heretofore.

It is even more challenging to measure enthalpy removed from the system in excess gas, but it is important to measure the power balance, to be sure one have replicated excess hydrogen, because without it one cannot expect excess hydrogen.

The amount of hydrogen and the oxygen generated by electrolysis is based on Faraday's law. The volumes of these gases are 0.116 cc/C for hydrogen and 0.0581 cc/C for oxygen at standard conditions [3,4]. The yield might exceed Faraday's law at very high temperatures, exceeding 3000°C, when direct pyrolysis can occur. However, the estimated temperature of ordinary glow discharge plasma at 100V is lower than this. Glow discharge occurs when electrolysis is performed at high input voltage (100V or more) in an aqueous solution [5,6,7,8]. A plasma forms, and a mixture of free hydrogen, oxygen and steam are formed on the surface of the cathode electrode. The generation of hydrogen at levels exceeding Faraday's law is observed when the conditions such as temperature, current density, input voltage and electrode surface are suitable [9,10,11,12]. The precise conditions are still not known, and controlling these conditions is difficult, so only a few observations of excess hydrogen have been made [13,14,15].

2. Experiment

2.1 Electrolysis cell

Figure 1 shows the schematic outline of the cell and measurement system [1,2]. The cell, made of Pyrex glass, is 10 cm diameter and 17 cm in height, and 1000 cc in capacity. The cap is Teflon rubber, 7 cm diameter. The cap has several holes, three for platinum RTDs (Resistance Temperature Detectors) to measure electrolyte temperature, two for a coolant water tube inlet and outlet (described below), one to vent the oxygen from the anode, and a dome to capture hydrogen gas from the cathode (described below).

2.2 Capture and measurement of hydrogen gas

The electrodes are isolated in separate

partitions within the cell, to prevent oxygen from mixing with hydrogen. A dome or funnel-like quartz glass dome surrounds the cathode, extending below it. It is 5 cm in diameter, 12 cm in length. The effluent gas from the cathode — a mixture of hydrogen from electrolysis, hydrogen and oxygen from pyrolysis, and water vapor from the intense heat — is captured inside the funnel as it rises up to the surface of the electrolyte. Oxygen from electrolysis is generated at the anode, outside the funnel. The anode is a platinum mesh wrapped around the funnel. Bubbles of oxygen rise from the anode to the surface and leave the cell through a separate vent hole.

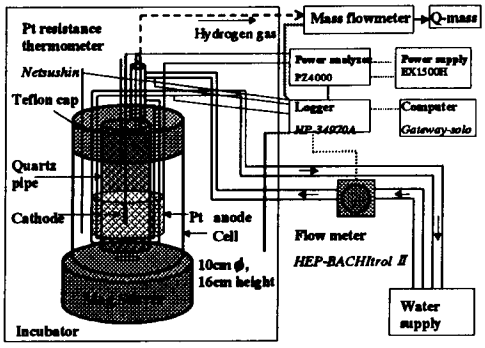

Fig.1: Detail of experimental setup.

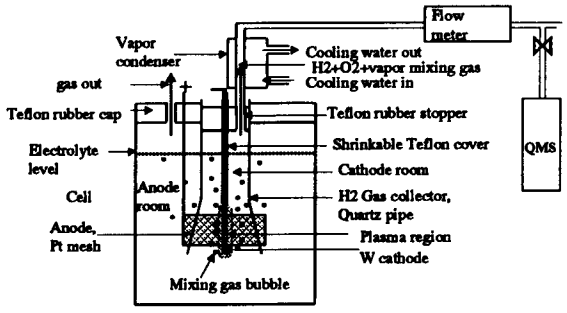

Fig.2: Detail for gas measurement system.

After the gas rises to the top of the funnel, it passes through a Teflon sleeve into a condenser. The water vapor condenses and falls back into the cell, and the hydrogen and oxygen continues through an 8-mm diameter Tigon tube and a gas flow meter (Kofloc Corp., model 3100, controller model CR-700). This is a thermal flow meter; the flow detection element is a heated tube. The minimum detectable flow rate is 0.001 cc/s, and the resolution is within 1%. The gas flow measurement system is interfaced to a data logger, which is attached to the computer.

After passing through the flow meter, part of the gas stream is diverted into a quadra pole mass spectrometer. A small, constant volume of the gas, typically 0.001 cc/s, passes through a needle valve and is analyzed by a mass spectrometer.

2.3 Power efficiency measurement

Two methods of power efficiency are performed simultaneously: flow and isoperibolic. Flow calorimetry is performed by circulating cooling water through a complicated circuit. The cooling water is tap water that begins by passing through a coiled copper tube immersed in a constant temperature bath. The cooling water then passes through a turbine flow meter (HEP-BATCHItrol II), and past the inlet temperature sensor RTD. From there, water goes through the outer chamber of the condenser above the cell. (Effluent gas from the cathode passes through the inner chamber. The water condenses and falls back into the cell, and the hydrogen gas continues on.) The cooling water tube then enters the cell to remove heat from the electrolyte solution. It is wound in a coil around the anode mesh and the funnel. The tube exits the cell, passes through the outlet temperature sensor RTD, and from there, it goes to the drain. Heat from both the condenser and the electrolyte is measured by comparing the inlet and outlet temperatures.

Isoperibolic calorimetry is performed by monitoring the temperature of the electrolyte solution with three RTDs, which are widely separated and placed at different levels in the solution. The solution is mixed with a magnetic stirrer.

The amount of the heat generation is estimated by combining the flow and isoperibolic data compared with the input electric power. The heat balance is still being investigated, and it will be described in a future paper.

2.4 Electrode and solution

The electrode was tungsten wire, 1.5 mm in diameter and 15 cm in length, the upper 13 cm of the wire covered with shrinkable Teflon, and the bottom 2 cm acted as the electrode. The

light water solution was made from high purity K_2CO_3 reagent at 0.2M concentration.

2.5 Power supply

The power supply was a Takasago model EH1500H. Input power was calibrated for each five seconds and measured with a Yokogawa PZ4000 meter. The sampling time was 40μs, during which 100 kb of data is collected.

2.6 Data collection

All data, including the flow rate of the cooling water, the temperature of the coolant at the inlet and outlet, the temperature at three locations in the cell and one location in the thermostatic chamber, the input voltage, current, and the amount of the hydrogen gas generation were recorded by a data logger (Agilent Corp., 34970A), and a computer for each 5s.

3. Results

A calibration is shown in fig.3. The temperature, input voltage and current were shown in fig.3A; the input voltage was 100 and 80V, the current was increased from 2.5 to 3.5A and the temperature stayed 80°C. Figure 3B shows the change in the amount of the hydrogen gas measured directly from hydrogen gas flow meter and the expected hydrogen flow from the electric current, based on Faraday's law. Over the entire 1000-seconds run, the value obtained from flow meter and the Q-mass system, i.e. the current efficiency, was same with expected amount calculated according to Faraday's law for the measured current.

The changes in current efficiency are calculated above for a two-value ratio (ε) of the hydrogen gas amount of flow meter and the input current, and in addition, the ratios of heat output to input electric power (power efficiency) are shown in Figure 3C. The power efficiency shows a small fluctuation of 93% ~ 103%, and the ε is 0.98~1.1 in this electrolysis condition. In the generated oxygen and vapor had not been detected and calculated in the measurement for the heat, other word, some of the heat may escape from the system. On the other hand, here, the larger value of ε as 1.1 comparing the theoretical one can be considered that some oxygen gas goes into the hydrogen collecting tube. One of the reasons of the leakage is caused from the structure of the open part of the bottom side; some of hydrogen

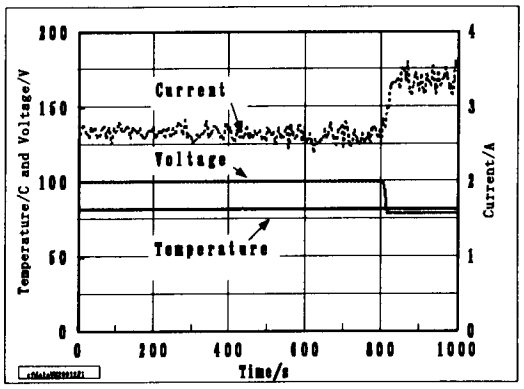

Fig.3A: Changes of input voltage, current and cell temperature for the calibration measurement.

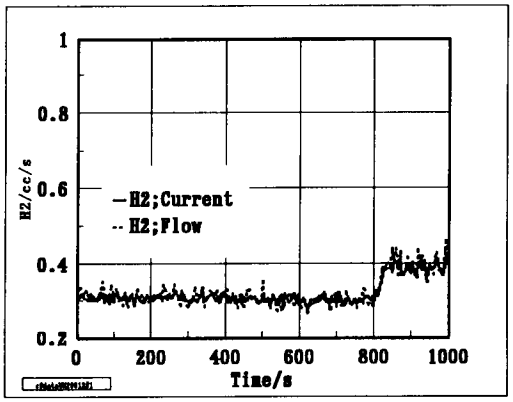

Fig.3B: Two rates of hydrogen generation measured by flow meter and estimation from current during normal electrolysis in fig.3A

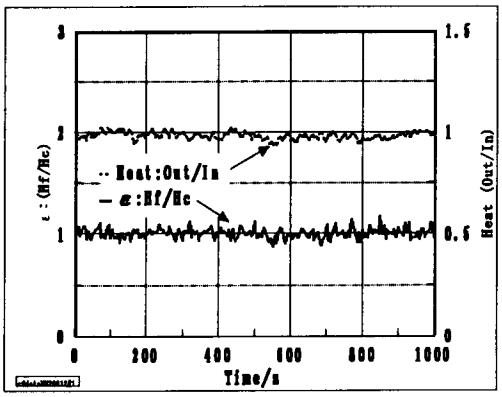

Fig.3C: Current and power efficiencies under fig.3A conditions

gas escaped from the cathode room, on the other hand, oxygen gas does into the cathode room where the capturing pipe surrounding the

cathode electrode and refuse into anode room of the cell caused from strong stirring by the magnetic element. It is understood that the recovery changes by the generation rate of gas and stirring because if the stirring was ceased then the value of recoverystayed at 100%.

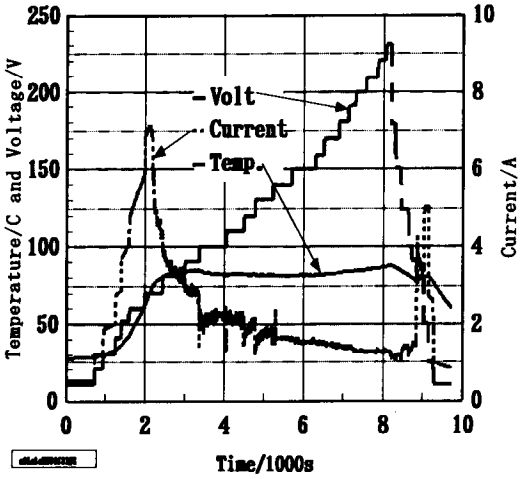

Fig.4A: Input changes for electrolysis.

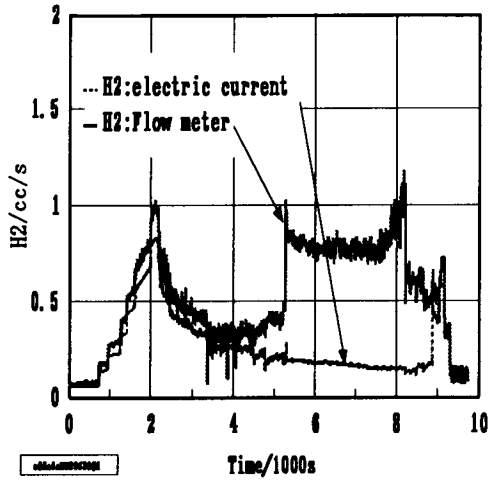

Fig.4B: Change in hydrogen generation.

A typical result exceeding Faraday's law is shown in Figure 4. In this case, the plasma electrolysis occurred at 2A/cm^2 of input current at 120V and 80°C in electrolyte temperature, as shown in Figure 4A. The rate ε is shown in Figure 4B. Here, ε exceeded unity when the plasma electrolysis started; the gas generation much increased with the input voltage.
The power efficiency graphs (Figure 4B) show almost 100%. However, in the experiment, heat recovery for oxygen evolution was not measured. So, we can only conclude that partial power efficiency was close to 100%. In same graph, the current efficiency of hydrogen gas generation are shown; the efficiency reached 8 (that is, 800% of the expected Faradic value), and it continued during plasma electrolysis at 230 V. Faraday's law predicts that 2440 cc should have been produced during the entire test run, but 5100 cc was measured (2662 cc excess). When we consider only hydrogen produced during periods when plasma formed, Faraday's law predicts 905 cc, and the measured amount was 3240 cc (2335 cc excess; 2.6 times the predicted value).

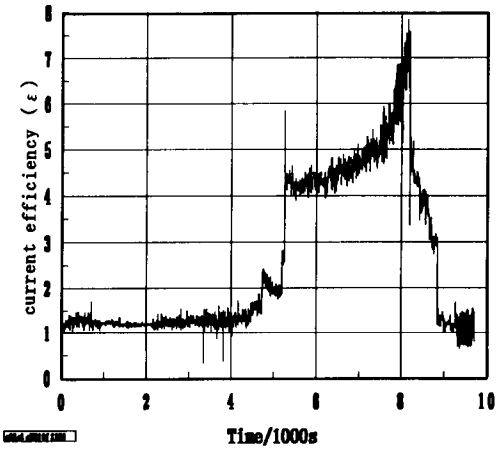

Fig.4C: Change of current efficiency(ε).

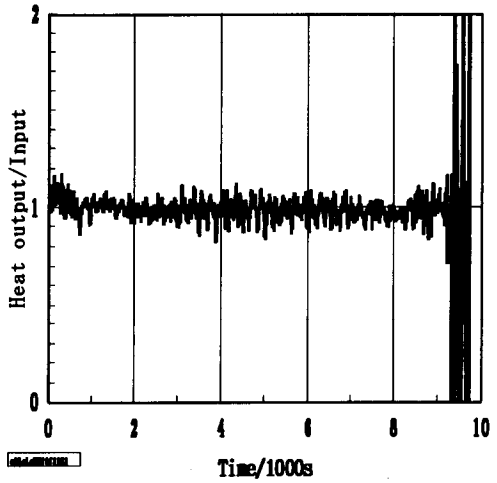

Fig.4D: Change in power efficiency.

The relationship between current efficiency of hydrogen gas generation (ε) to voltage is shown in figure 5. Here, we can see that efficiency is strongly dependent on input voltage. Other parameters such as input current, duration time of the hydrogen generation and cell temperature do not show any strong correlation to ε.

4. Conclusions

It is difficult to determine the exact relationship between the current efficiency, ε and other factors. However, the data strongly suggests that one of the key factors is the input voltage, as shown in Figure 5 of the ε and V relationship. Here, it can be understand that the ε has a tendency of increase with input voltage. One point of ε value in the figure shows up to twice of the theoretical value of unity; the point was obtained by the result of plasma electrolysis. On the other hand, the ε is remaining at unity for all of the other normal electrolysis. It can be predicted that that if the input voltage were increased to several hundred volts, then the ε would far exceed unity.

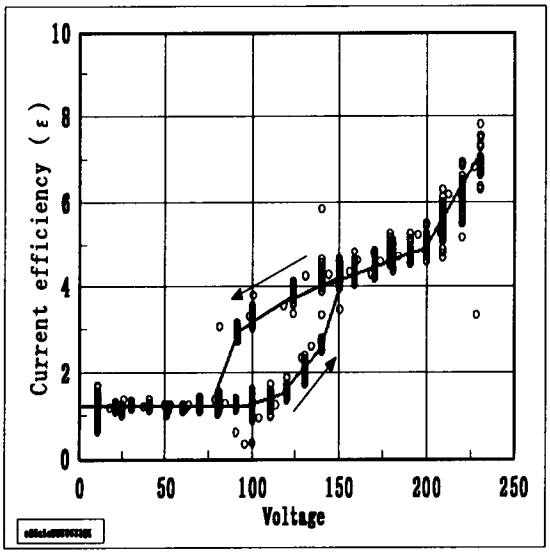

Fig.5: Voltage dependency for efficiency.

References:

(1) "Production of Heat during Plasma Electrolysis in Liquid", Tadahiko Mizuno, Tadayoshi Ohmori, Tadashi Akimoto, Akito Takahashi, Jpn J. Appl. Phys., Vol.39, No.10 (2000) 6055-6061.

(2) "Neutron Evolution from a Palladium Electrode by Alternate Absorption Treatment of Deuterium and Hydrogen", Tadahiko Mizuno, Tadashi Akimoto, Tadayoshi Ohmori, Akito Takahashi, Hiroshi Yamada and Hiroo Numata, Jpn J. Appl. Phys, Part 2, No.9A/B, Vol.40 (2001) L989-L991.

(3) "Creation of new energy by photocatalyst: Technology of clean hydrogen fuel production from solar light and water", Arakawa, H., Reza Kenkyu Vol.25 (6), (1997) 425-430.

(4) "Photo electrochemical hydrogen production", Richard Rocheleau, Anupam Misra, Eric Miller, Proc., 1998 US-DOE, Hydrogen Program Review, NREL/CP-570-25315.

(5) E. M. Drobyshevskii, Y. A. Dunaev and S. I. Rozov, Sov. Phys. Tech. Phys., Vol.18 (1973) 772

(6) V. M. Sokolov, Sov. Phys. Tech. Phys., Vol.29 (1984) 1112

(7) E. P. Koval'chuk, O. M. Yanchuk and O. V. Reshetnyak, Phys. Lett. A, Vol.189 (1994) 15

(8) E. M. Drobyshevskii, B. G. Zhukov, B. I. Reznikov and S. I. Rozov, Sov. Phys. Tech. Phys., Vol.22 (1977) 148

(9) A. Hickling and M. D. Ingram, Trans. Faraday Soc., Vol.60 (1964) 783

(10) A. Hickling, "Electrochemical processes in glow discharge at the gas-solution Interface" , Modern Aspects of Electrochemistry No.6, ed. by J. O'M. Bockris and B. E. Conway, Plenum Press New York (1971) 329-373

(11) S. K. Sengupta and O. P. Singh, J. Electroanal. Chem., Vol.301 (1991) 189

(12) S. K. Sengupta and O. P. Singh and A. K. Srivastava, J. Electrochem. Soc., Vol.145 (1998) 2209

(13) Jasnogorodski I. S., Elektrolytishes Harten, (1951)

(14) Polakowski N. H., Met. Plogr., 67(1955) 98

(15) Shigeo Ohwaku and Kazuo Kuroyanagi, "Electrolytic Hardening-Immersion method report 1" Jpn. J. Met. Soc., 20 (1955) 63-70

Studies of Photon Source for Multi Photon Induced Fission under Plasma Electrolysis

Masayuki Matsunaka, Tomoo Ohishi and Akito Takahashi

Department of Nuclear Engineering,
Graduate School of Engineering,
Osaka University
Yamadaoka 2-1, Suita, Osaka, 565-0871, JAPAN

Abstract

We performed plasma electrolysis experiment with tungsten cathode and potasium carbonate solution, aiming at measurements of X-rays and γ-rays during plasma electrolysis. The measurement under plasma discharge has been troubled by electromagnetic noises, but in this work, noise reduction was performed by wave form analysis and significant counts of bump was observed in low energy region.

Keywords: plasma electrolysis, multi-photon absorbtion, photo fission, x-ray burst

1. Introduction

There are many reports that excess heat and nuclear transmutation were observed by CF experiments.[1] Mizuno reported the detection of anomalous elements which related with production of excess heat in the plasma electrolysis experiment.[2]

In order to explain the observed results, the Multi Photon Induced Fission / Selectrive Channel Scission (MPIF/SCS) model was proposed.[3] Mizuno's experiment was analyzed by this theoretical model, and analytical results showed good agreement with experimental results.[4] The MPIF/SCS model supposes the existence of intense bursts of photons with energy less than 5 MeV, which induce nuclear collective excitation of cathode metal nuclei by multi-photon absorbtion to lead to fission channel. For example, we require photon source emitting random bursts of 1-100 keV photons (X-ray region) in short pulse (less than 10^{-9}s) with very high peak flux (more than 10^{28} photons cm^{-2} s^{-1}). We have thought that the plasma region produced in thin layer (probably less than 1 micro-meter) close to cathode by electric discharge in electrolyte may provide such photon source due to mechanism similar to X-ray laser generation, and then excite cathode metal nuclei to make them fission.

The aim of this work is to search if there are such X-ray bursts from plasma electrolysis experiments. Therefore, we have performed measuremetns of X-rays and γ-rays during plasma electrolysis. At the begining of experiment, the electromagnetic noises were too many to find radiation signals sharing possible X-ray energy spectrum. The noises were drastically reduced after applying wave form analysis system, and a bump spectrum, which is thought to be a set of radiation signals, appeard near 50 keV region.

2. Experimental Setup

2.1 Electrolysis System

Figure 1. is schematic view of electrolysis system. The electrolysis was performed using direct current power supply and controled by electrolytic voltage.

The cathode was 5 mm $\times$ 5 mm square plate of tungsten. The thickness of plate was 0.3 mm. For the lead rod, 1.2 mm diameter tungsten rod was used. The lead rod was covered with tightly fitted Teflon sleeve. The plate was attached to lead rod by spot welding. Nilaco tungsten (purity 99.95%) was used.

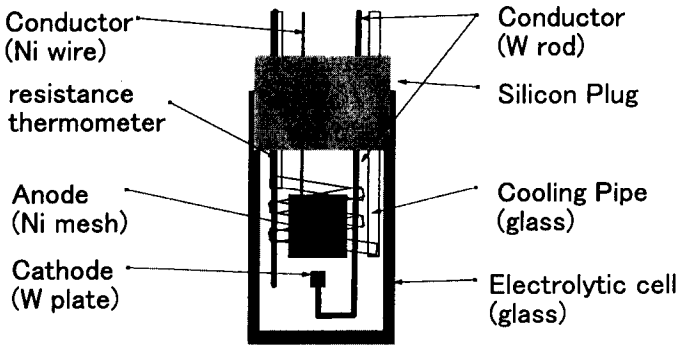

Fig. 1: schematic view of elctrolytic cell

The anode was 25 mm diameter × 33 mm long cylinder made of nickel mesh. The lead rod was 1 mm diameter of nickel wire and was covered with Teflon sleeve. The open type glass cell was used as electrolytic cell. The inside diameter of electrolytic cell was 6.5 cm, and the thickness of wall was 2.5 mm.

The electrodes, platinum resistence thermometer and coolant pipe made of glass were set up through sillicon plug, and the plug was put in the glass cell. The arrangements were adjusted so that the cathode plate existed in the center of the anode cylinder of electrolytic cell.

The electrolyte was 0.2 molar potassium carbonate solved in light water. Its amount was 250 ml.

2.2 Measurements setup

The X-ray was measured by using a HPGe semiconductor detector. The detector was set at 4.5 cm apart from the surface of electrolytic cell. The radiation signals from HPGe semiconductor detector were processed through circuit of modules, and finally counted by Multi Channel Analyzer (MCA). The measured energy range was from 5 to 150 keV. The information about X-ray energy spectrum and time variation of X-rays (measurement in Multi Channel Scaler mode: MCS) were also obtained.

At the same time, measurement of visible lights emitted during plasma electrolysis was performed. Because it is expected that the result in observing light from plasma region gives information to understand discharge mechanism. The monochrometer was used for measuring visible light. The measured light range was from 200 to 700 nm. This measurement required 500 seconds because of its mechanical design.

The electrolytic voltage and current were also recorded by using pen recorder.

2.3 Electrolytic Modes

There were three types of electrolytic mode in our study. The first mode was preparatory electrolysis, which carried out in low voltage (about 40 V) in order to adjust the electrolyte temparature. The target temparature was 70 degrees Centigrade. The second mode electrolysis was carried out with varying voltage in order to confirm the discharge condition. Because some different discharge states existed, and noteworthy state called as plasma discharge was one of them. The discharge state changed due to increase of electrolytic voltage. The third mode electrolysis was for measuring the radioactive rays and the light spectrum. Power supply was used carried out in constant voltage mode.

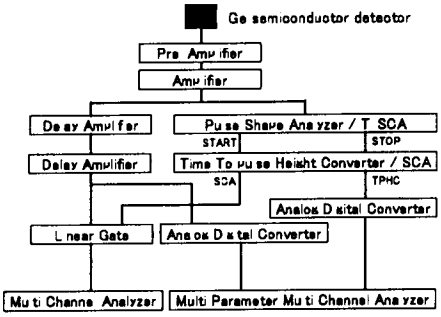

Fig. 2: schematic view of modules

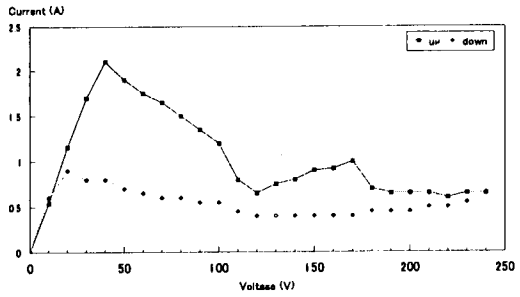

Fig. 3: variation of electrolysis current

2.4 Wave Form Analysis

In order to reduce electromagnetic noises, wave form analysis was applied on the measurement of X-rays. As shown in section 3, the electromagnetic noises from plasma region are too much, so we had to adopt the technique to kill noises.

Figure 2 shows signal processing circuit. For noise reduction, we use the fact that the decay time of radiation signal differs from that of electromagnetic noise signal. It is usually supposed that decay time of radiation signal is much longer than that of noise signal.

To explain shortly, right side series modules of Fig. 2 work for wave form analysis, and left side series modules work for energy analysis of signals with gating signals from the wave form analysis.

3. Experimental Results

3.1 Electrolysis Procedure

Figure 3 shows the relationship between electrolytic voltage and electrolytic current. The "top" curve indicates the relationship when increasing voltage, and the "bottom" curve indicates the one when decreasing voltage. Here, we explain changings of the state in the electrolytic cell when electrolysis was carried out on the second mode. The voltage was changed by 10 V step, and the parameter values were recorded.

The current increased lineary with increase of voltage at the region from start point to 40 V. After 40 V, current decreased gradually till 100 V. The electrolysis state was normal till this point. When the voltage became 110 V, the current dropped down to 0.8 A, and discharge was started. Till 170 V, following voltage increase, the current was increased and the discharge region had expanded. When the voltage became 180 V, the current dropped again down to 0.7 A. The discharge state shifted to plasma discharge. The current was almost constant between 180 V and 240 V. The plasma discharge was continued and emitted intense light. The value 240 V was maximum of power supply we could use. In this case, the relationship between electrolysis state and current value in decreasing voltage was not clear. Though figure shows tendency that the current at decreasing voltage is lower than that at increasing voltage.

3.2 Time Variation

It was confirmed that the condition of plasma electrolysis in this system was that the electrolytic voltage was over 180 V, by the second mode electrolysis. Therefore, the electrolytic voltage for measuring radiation and visible light was defined as 200 V. Figure 4 shows time variation of parameters when measurements were carried out. However the "Ge MCS" is the data not analyzed by wave form analysis. Maybe it contains a lot of noise counts.

Figure 4 indicates some features. The first feature is that the MCS counts has close correlation with current. The second feature is that both of them slowly decrease and they are finally saturated. The third feature is that both of the MCS counts and current are sensitive to voltage change.

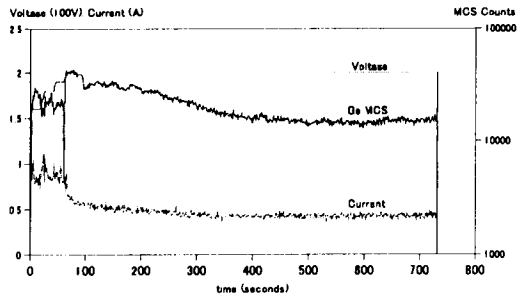

Fig. 4: time variation of parameters

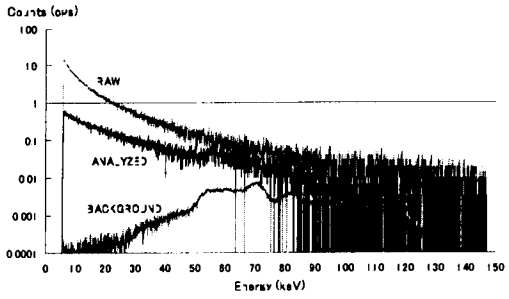

Fig. 5: Energy Spectra of each condition

3.3 X-ray Energy Spectra and Light Spectra

The measurements of X-ray energy spectrum and light spectrum were carried out when the voltage was constant. In this case, it was the period from 100 to 700 seconds in Fig. 4.

The measured results by HPGe detector are shown in Fig. 5. The "RAW" and "ANALYZED" line denote the direct output from amplifier and the output through the wave form analysis circuit, respectively, during plasma electrolysis. The "BACKGROUND" line is the energy spectrum as natural background which had been measured before performing electrolysis. The measuring times of raw, analyzed and background were each 100, 300 and 30143 seconds, respectively.

The shape of the raw spectrum was so broadly monotonous that any remarkable structure were not found. Maybe almost all of them were attributed to electromagnetic noises. We cannot get any information from this spectrum owing to too many noises, even though some radiation signals might have been counted.

The "analyzed" spectrum was also a broad spectrum. However noises were almost reduced by the wave form analysis, but it may contain still a component of noises. Differred from raw spectrum, we can find a bump in the region from 50 to 60 keV. It is not very clear, but there is possibility that the radiation signals had been counted there. Someone may point out that similar bump is appeared in the background spectrum. But the peak at 70 keV in the background was not appeared in the "analyzed" spectrum. The bump in the "analyzed" spectrum is therefore regarded as real radiation (X-ray) signals.

The result of measured light emission is shown in Fig. 6. The background measurement was carried out two times. But they are not drawn in Fig. 6 due to their very small values. They were less than 25 counts in the each wavelength. It is possible to say that the almost background counts for measuring light spectrum were circuitly thermal noises originated from measuring instruments but negligible.

In the spectrum of emitted light, it seems that the shorter wavelength ingredient contained about twice as the longer wavelength ingredient, though the emitted light contained all measured wavelengths. There are seen some peaks and bumps in the spectrum, but there is some room for further consideration to understand peaks. The measurement was carried out by scaning wavelength in one nanometer step using a set of monochrometer and photomultiplier. In this experiment, the scaning time of each wavelength was one second. So the measuring time was required for 500 seconds. This is too long for measuring the state of plasma discharge. We have ever observed that the intense emission of white light sometimes occurs during plasma electrolysis intermittently (bursts). That emission was possible to be recorded as peak and bump shapes.

4. Discussion

As described above, we obtained interesting result in the noise reduced X-ray energy spectrum using wave form analysis method. But the significant counts were probably still buried in electromagnetic noises. So we suppose here some possibities about understanding the significant counts of bump.

We think that the obtained significant counts of bump is one of evidence of X-ray sourd

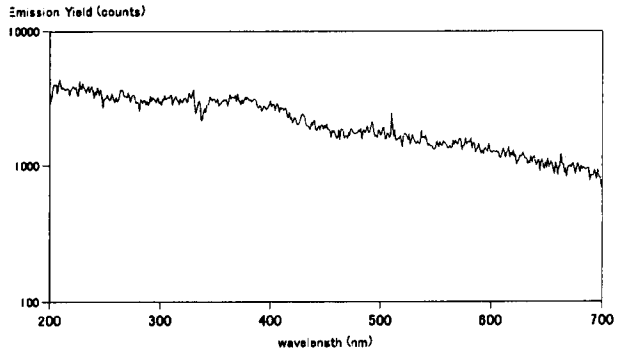

Fig. 6: Spectrum of Visible Light

for Multi Photon Induced Fission under plasma electrolysis. In this point of view, there are two possibilities of the significant counts. The first possibility is that the photons emitted from thin plasma layer were counted. The mechanism of occuring photon emission in the electrolytic cell is not clear, but we think that it may be possible for plasma region which produced by electric discharge in electrolyte to emit large amount of photons at a burst due to the mechanism similar to X-ray laser generation. If it have been confirmed that the photons are emitted at a burst and high peak flux, it would be possible to excite cathode metal nuclei and make them fission.

The second possibility is that the significant counts are bremsstrahlung X-rays emitted by deceleration of charged particles. As such charged particles, the scission fragments produced by fission of cathode metal nuclei are thinkable if the multi-photon induced fission of cathode metal nuclei have been assumed. The scission fragments would be produced in surface of cathode plate and have highly kinetic energy. They may lose their energy for an instant in electrolyte and convey electrons may emit photons as bremsstrahlung X-rays. But only a few X-rays are reachable to detector even if large amount of bremsstrahlung X-rays have been emitted, because almost all X-rays near 50 keV region would be absorbed before overcoming a wall of electrolyte.

In order to obtain more evidence, it is needed to improve radiation-identification. The further experiment which uses filtering technique with various K-shell edge absorption for X-rays is under developing for this purpse.

5. Conclusion

We have performed measurements of X-rays, γ-rays and light spectrum under plasma electrolysis. The detection accuracy was increased by using wave form analysis. As a result, significant counts in X-rays were obtained near 50 keV region. Identification of this significant counts in X-ray energy spectrum is under way using the filtering technique. If emission of X-ray is confirmed, further experiment will be needed to investigate whether the X-ray emission is in burst or not. At the same time, it is also important to measure light spectrum in order to understand the mechanism of plasma discharge under electrolysis of liquid.

REFERENCES

[1] T. Mizuno, T. Ohmori, T. Akimoto and A. Takahashi: *Jpn. J. Appl. Phys.*, **39** (2000) 6055

[2] T. Mizuno, T. Ohmori, K. AZUMI, T. Akimoto and A. Takahashi: *Italian Phys. Soc. Conf.* **70** *(Proc. ICCF8)*, (2000) pp.75-80.

[3] A. Takahashi, M. Ohta and T. Mizuno: *Jpn. J. Appl. Phys.*, **40** (2001) 7031; Also see *Italian Phys. Soc. Conf.* **70** *(Proc. ICCF8)*, (2000) pp.397-402.

[4] M. Ohta and A. Takahashi:*Proc. JCF4* (in this issue).

REACTION YIELD ENHANCEMENT UNDER DEUTERIUM ION IRRADIATION OF DEUTERATED Au/Pd SAMPLES

M. Miyamoto, Y. Awa, N. Kubota, A. Taniike, Y. Furuyama and A. Kitamura*
Department of Nuclear Engineering, Kobe University of Mercantile Marine
5-1-1 Fukaeminami-machi, Higashinada-ku, Kobe 658-0022, Japan
*kitamura@cc.kshosen.ac.jp

Abstract: To investigate possible anomaly in nuclear reactions in solids, deuterium ion irradiation of deuterated Au/Pd samples have been performed with extensive measurements of reaction products and *in situ* characterization of the samples including ERDA and RBS. The deuterium density in the sample with a modified composition under irradiation has been found to grow up to a value three times greater than that in $PdD_{0.86}$, and the D(d,p)t reaction rate to become two orders of magnitude greater than the calculated one. We speculate that the formation of the mixed layer of Au and Pd gives rise to enhancement of the reaction rate, maintaining significantly high deuterium density.

Keywords: D(d,p) reaction rate enhancement, Au/Pd, deuterium density, *in situ* accelerator analyses

1. INTRODUCTION

A variety of deuterium-induced reaction in metal deuterides with some yield anomaly has been reported in recent years. Three-body reactions, *i.e.*, DD(d,^{4}He)pn, DD(d,^{4}He)d and DD(d,^{3}He)t, have been claimed to take place with great enhancements of the reaction rate in TiD_x[1-3]. Nuclear transmutations in a variety of samples have also been reported by many authors, which includes experiments on forced permeation of D through a multi-layered film of Pd and Cs[4].

In these reports, the deuterium densities of the samples have not always been made clear during these reactions. The three-body reaction probabilities were measured with the titanium deuterides, however, the deuterium density under irradiation was assumed. In some experiments of nuclear transmutation, the deuterium densities in the samples reached the saturation value.

Measurements of the local deuterium density in samples should be effective to identify the anomaly and clarify the origin of anomalous enhancements of the reaction rate[5]. In this paper, we present experimental results on the D(d,p)t reaction rate and deuterium density measured *in situ* with accelerator analyses under deuterium irradiation of gold-evaporated palladium (Au/Pd) samples.

2. EXPERIMENTAL PROCEDURE

A schematic of the experimental system is shown in Fig. 1. The sample is irradiated with atomic/molecular deuterium ion beams extracted from a 30-kV duoplasmatron ion source. The beams bombard the front surface of the sample in vacuum whose rear surface is exposed to deuterium gas in a reservoir. The sample can be

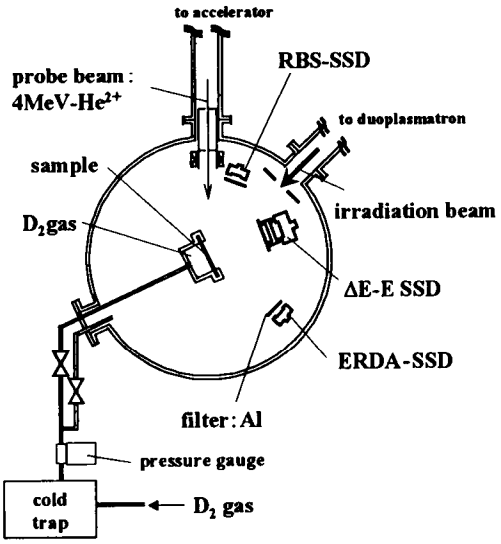

Fig.1. Experimental system.

characterized *in situ* by means of accelerator analyses, *i.e.* Elastic Recoil Detection Analysis (ERDA), and Rutherford Backscattering Spectroscopy (RBS), during/after irradiation. Four solid state detectors (SSDs) are prepared around the sample to detect products of deuterium-induced reactions at 110° and scattered/recoil particles for characterization at 160° and 34° with respect to the analyzing accelerator beam. In particular, the ΔE-E counter telescope technique is employed at 110° for simultaneous measurements of mass and energy. Thin aluminum films are mounted on all SSDs to shield them from thermal radiation by the beam heating of the sample.

In the present experiments, some Pd samples coated with vacuum-evaporated Au layers have been prepared. The Au layer prevents deuterium reemission into vacuum due to recombination on the Pd surface, which is expected to keep the deuterium density high in the Pd bulk. The typical thickness of the Au layer is several tens of nm as measured with ^{4}He-RBS method.

3. RESULTS AND DISCUSSION

The DD reaction rate in palladium has been measured with use of the ΔE-E counter telescope. Here, we introduce a normalized yield Y_n in order to evaluate the difference between the measured reaction rate and the theoretical one. The Y_n is defined as the ratio of the measured reaction rate Y_m to the calculated reaction rate Y_c;

$$Y_n \equiv Y_m / Y_c.$$

The Y_m is expressed as follows:

$$Y_m = (\Delta Y_{ROI}/N_i) \times (4\pi/\Delta\Omega),$$

where ΔY_{ROI} is the measured proton yield of the D(d,p)t reaction during bombardment of N_i incident deuterons, and $\Delta\Omega$ is the solid angle of the detector. The TRIM85N code[5] is used to calculate the reaction rate of the D(d,p)t reaction for a given composition of target atoms and thickness.

Figure 2 shows evolution of the Y_n for the D(d,p)t reaction during 15-keV D_2^+ irradiation of the Au(20nm)/Pd sample up to a fluence of 6.6×10^{18} /cm^2. In the phase 1 up to the fluence of 2.9×10^{18} /cm^2, the sample was irradiated after

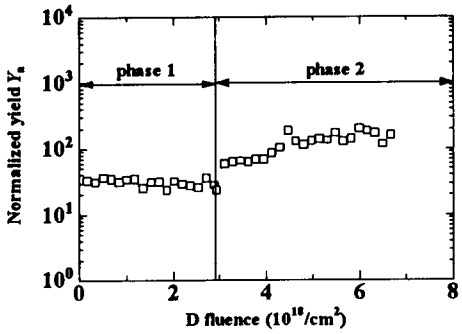

Fig.2. Evolution of Y_n during 15-keV D_2^+ irradiation of the Au(20nm)/Pd sample.

deuterium loading by exposure to D_2 gas at a pressure of 1.0×10^5 Pa for 3 hours. The phase 2 followed a 12-hours rest during which the reservoir was evacuated and 2-hours exposure of the rear surface to D_2 gas at a pressure of 1×10^5 Pa. The sample was irradiated up to the fluence of 6.6×10^{18} /cm^2 under the same condition as in the phase 1. The Y_n using Y_c for a target composition of $PdD_{0.86}$ has reached the maximum value of 200 in the phase 2.

For examining effect of Au coating and reproducibility of the qualitative feature, we irradiated the Au(70nm)/Pd sample under the same condition with that in the phase 1. Figure 3 shows the evolution of the Y_n for the D(d,p)t reaction up to a fluence of 1.1×10^{19} /cm^2. Being consistent with the previous result, the Y_n exceeds unity greatly, and even approaches 10^3.

In both cases, the Y_c has been calculated for the target with the atomic composition of $PdD_{0.86}$ to avoid complexity introduced when dynamic change in thickness and composition of the Au/Pd layer is taken into account. The Y_c would be even greater when the target is assumed to be a compound of Au and Pd, since the greater energy loss of incident deuterons in the Au layer reduces

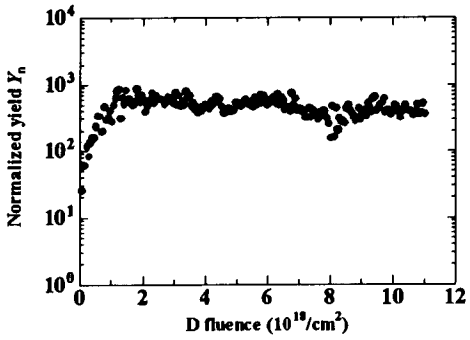

Fig.3. Evolution of Y_n during 15-keV D_2^+ irradiation of the Au(70nm)/Pd.

Table 1. Reaction probabilities calculated with TRIM85N for targets irradiated with 15-keV D_2^+.

target composition	reaction probability(/ion)
$PdD_{0.86}$	1.5×10^{-13}
$PdD_{2.7}$	3.9×10^{-13}
Au(20nm)/$PdD_{0.86}$	2.3×10^{-14}
Au(70nm)/$PdD_{0.86}$	1.8×10^{-18}

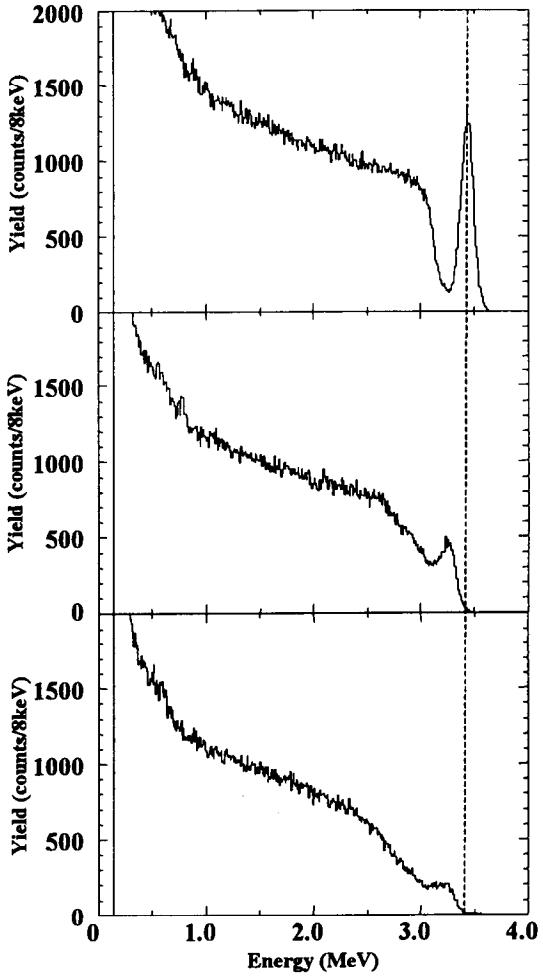

Fig.4. Energy spectra of RBS taken at the fluence of zero (upper), 4.5×10^{18} /cm^2 (middle) and 1.1×10^{19} /cm^2 (lower). The broken line represents the detection energy of ^{4}He scattered by Au atoms on the sample surface.

the probability of nuclear collision. As can be seen in Table 1 listing reaction probabilities calculated with TRIM85N, the Y_c could be an overestimated value by more than one order of magnitude.

Under D_2^+ irradiation, the samples have been analyzed by means of RBS and ERDA methods using a 4-MeV ^4He beam. The typical energy spectra of RBS made at the fluence of zero, 4.5×10^{18} /cm^2 and 1.1×10^{19}/cm^2 are shown in Fig. 4. The continuum spectrum below 3.1 MeV corresponds to the Pd(α,α)Pd scattering, and the spectrum with the peak near 3.4 MeV corresponds to the Au(α,α)Au scattering. With the progress of the D_2^+ irradiation, the Au(α,α)Au scattering yield decreases and its spectral shape is also deformed. In addition, the slope of the spectral edge formed by the Pd(α,α)Pd scattering becomes smaller. The decrease in the Au(α,α)Au scattering yield can be caused either by the sputtering loss of the Au atoms or by formation of a mixed layer of Au and Pd. The peak flattening and the edge moderation, however, can be explained only by mixing of Au, Pd and possible other elements. The lattice defects including the mixing of the layers could trap more deuterium than the interstitial sites, which could lead to high density of deuterium in the sample.

The deuterium depth profiles are shown in Fig.5, which are deduced from energy spectra measured with ERDA at the same fluence as in the case of RBS. The deuterium density increases with increasing irradiation fluence. The maximum deuterium density of 1.8×10^{23}/cm^3 reached at the fluence of 1.1×10^{19} /cm^2 corresponds to the $PdD_{2.7}$, which is extraordinarily higher than the saturated deuterium density of 5.8×10^{22} /cm^3 corresponding to $PdD_{0.86}$. Using the Y_c of 3.9×10^{-13}/deuteron for $PdD_{2.7}$, the Y_n of 200 has been obtained. Hence we infer that some mechanisms to enhance the reaction rate or the reaction cross section are working in this mixed layer of Au and Pd loaded with extraordinarily high density of deuterium.

To examine effects of sample conditions, we have also irradiated a Pd sample without Au coating under the same condition as in the case of the Au/Pd sample. Figure 6 shows the evolution of the normalized yield Y_n for the D(d,p)t reaction up to a fluence of 6.4×10^{17} /cm^2. The Y_n for the

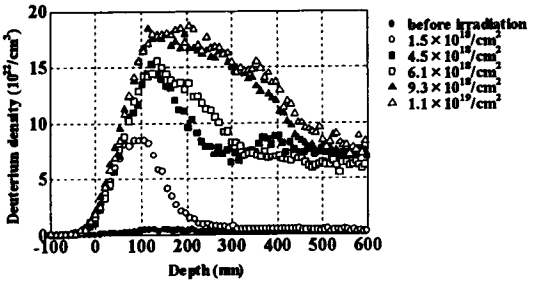

Fig.5. Evolution of the depth profile of deuterium density in the Au(70nm)/Pd sample during irradiation.

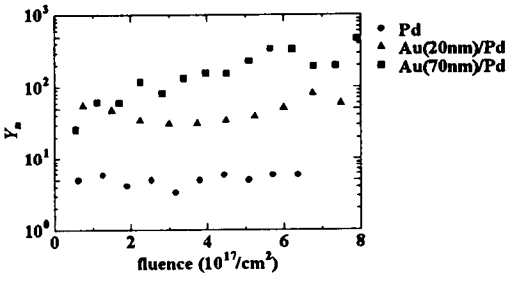

Fig.6. Comparison of normalized yields obtained for the Pd, the Au(20nm)/Pd and the Au(70nm)/Pd sample.

Au/Pd sample has been ten times greater than that of the Pd sample without Au coating. The existence of Au seems to be essential for the enhancement of the reaction rate.

On the other hand, to check possible effect of clustering of the incident beam deuterons, irradiation with molecular and atomic ion beams, *i.e.*, 26-keV D_2^+ and 13-keV D^+ beams, was performed with the Pd sample of 1-mm thickness.

The evolution of the Y_n for the case of D^+ bombardment is compared in Fig.7 up to a fluence of 6.4×10^{17} /cm^2. Since the TRIM85N code takes no account of clustering and of the charge state of the incident particle, the same value of the Y_c is used for both cases of the 26-keV D_2^+ and the 13-keV D^+ irradiation. The Y_n for 26-keV D_2^+ irradiation is 10 times larger than that for 13-keV D^+. Since this result is a preliminary one, we need further experimental evidence to confirm possible anomaly even for a pure Pd target.

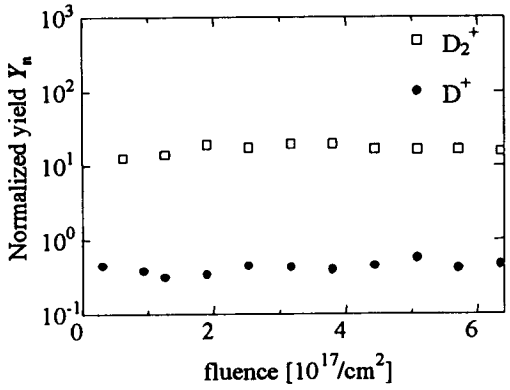

Fig.7. Evolution of Y_n in the case of irradiation with 26-keV D_2^+ (open squares) and with 13-keV D^+ (dots).

4. SUMMARY

The normalized yield Y_n reaching the maximum value of the order of 10^2 has been recorded under the 15-keV D_2^+ irradiation of Au-evaporated Pd samples which has formed the mixed layer of Au and Pd in the near-surface region. The deuterium density in the sample about three times higher than the deuterium saturation density of $PdD_{0.86}$ has been simultaneously measured. We speculate that the formation of the Au/Pd-mixed layer retaining the high deuterium density induces the enhancement of the reaction rate.

REFERENCES:

[1] A. Takahashi, *et al.*; Fusion Technol., 34 (1998) 256.

[2] J. Kasagi, *et al.*; J. Phys. Society Japan, 64 (1995) 777.

[3] A. Takahashi et al.; Fusion Technol., 34, (1998) 256

[4] Y. Iwamura , *et al.*; J. Appl. Phys. 41 (2002) 4642-4650.

[5] A. Kitamura, *et al.*; Fusion Technol., 29 (1996) 372.

Analysis of Nuclear Products in Hydrogen Penetration through Palladium

H.Onodera, S.Narita, H.Yamada, H.Suzuki, N.Tanaka, T.Nyui

Department of Electrical and Electronic Engineering, Iwate University

Abstract

Elemental analysis was employed for the palladium sample through which the hydrogen gas penetrated. We analyzed sample surface by Time-of-Flight secondary ion mass spectroscopy and searched for newly produced elements during the gas permeation process. Significant increase of the counts for Cr, Fe, and Cu were found after the experiment. These elements could have been produced by nuclear transmutation.

Keywords: Pd, hydrogen penetration, nuclear transmutation, Cr, Fe, Cu, Secondary ion mass spectroscopy

1. Introduction

Various results about anomalous nuclear reaction in solids have reported in several types of experiments. The controlled gas out-diffusion with palladium (Pd) deuteride or hydride in the evacuated chamber is one of the unique method [1,2]. It was developed by Yamaguchi *et al.* and called "in vacuo" method. They observed the excess heat and helium production, which was thought to be a possible result of a nuclear reaction. Iwamura *et al.* has reported observation of nuclear transmutation in deuterium permeation experiment with Pd film complexes, which consist of a thin Pd layer, alternating CaO and Pd layers and bulk Pd [3,4]. They recently have found a certain rule of nuclear transmutation, that is, 8 mass number and 4 atomic number increase in the process. The phenomenon was observed with good reproducibility. These results suggest that there is a key to understand the reaction in the mobility of D (or H) atoms in Pd lattice. In the study described here, we performed the experiments on hydrogen penetration through Pd and search for nuclear products as a result of the nuclear transmutation process. This method has an advantage of minimizing contamination to the sample, which is preferably used in investigating small amount of elements. This study would provide us information to understand transmutation process systematically. In addition, we would consider the possibility of nuclear transmutation in not deuterium but hydrogen system as some researchers have claimed in various experiments [5,6].

2. Experiment

The Pd plate (99.95% pure) sample ($0.1 \times 12.5 \times 12.5$mm) was rinsed with acetone and pure water, then washed by aqua regia to remove impurities on the sample surface. No hydrogen gas was loaded to the sample before experiment. Fig.1 shows a schematic view of the experimental apparatus. The Pd plate was set into a stainless steel holder placed between two chambers as shown in Fig.2. The upper chamber is filled with hydrogen gas at a pressure up to 10 atm, and the lower is evacuated by a diaphragm pump (ULVAC:DAM-010). The gas atoms are driven through the Pd sample to the evacuated chamber by the pressure gradient. Fig.2 shows the sample holder and flowing path of the hydrogen gas. The lower sample holder has several holes where the gas flows. The gas was kept flowing for about 2 weeks, then sample was taken out from the holder. Before the element analysis, the sample was heated to 400℃ to purge the hydrogen atoms remaining in. Finally the sample surface was analyzed by Time-of-Flight secondary mass spectroscopy (TOF-SIMS) (ULVAC-PHI:TFS-2100). TOF-SIMS has a good sensitivity for a small quantity of the elements on the sample with high resolution in mass number although it is difficult to deduce the absolute quantities from its output data alone. The primary ion in TOF-SIMS was Ga^+ and measured area was 40×40 micron square. In order to take into account the contamination from the

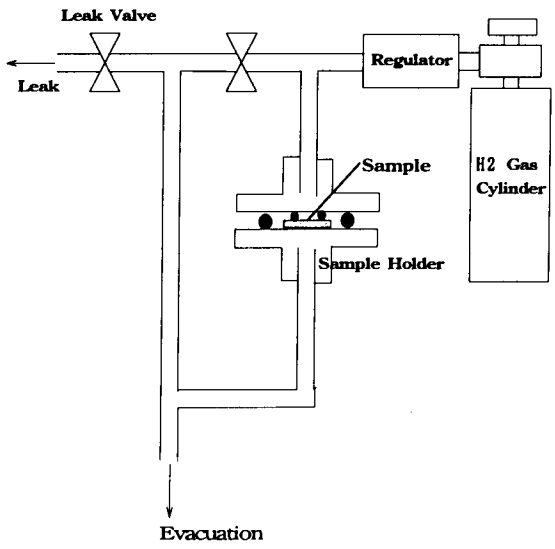

Fig.1 Experimental setup

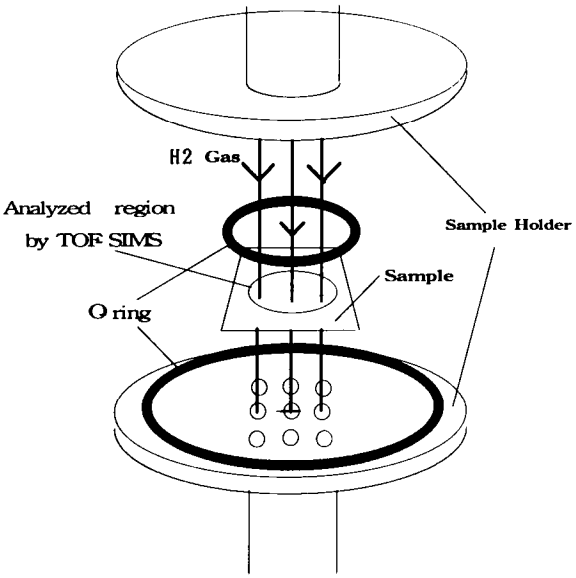

Fig.2 Sample holder. Hydrogen flows from upper chamber to lower chamber penetrating the Pd sample.

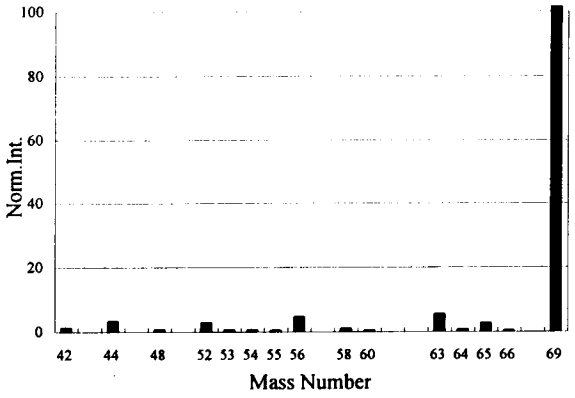

Fig.3 Normalized count intensity for mass number 40-70 for the sample before experiment.

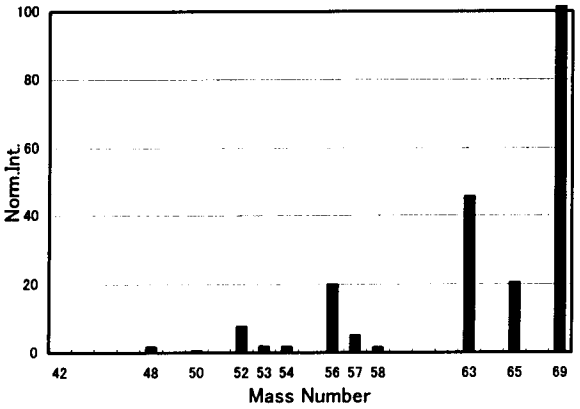

Fig.4 Normalized count intensity for mass number 40-70 for the sample after experiment.

environment, we prepared the control sample ("before sample"), which was set into and removed from the holder without flowing the hydrogen gas, and compared the composition of the elements on the sample between them to specify newly produced elements during the experiments. TOF-SIMS is capable of analyzing all the elements with their isotopes. We also analyzed the isotopic compositions for the elements detected.

3. Results and discussion

In TOF-SIMS analysis, three randomly selected areas (40 μ m $\times$ 40 μ m) of each sample were analyzed. We did not see significant difference in the mass spectrum for every area. In this study, we do not discuss absolute quantities of the elements, since we have difficulties in quantitative analysis with the TOF-SIMS method. Instead, we use a normalized intensity that is defined here as the count of the secondary ions of each element divided by the total count of ions recorded, and multiplied by 10000.

Fig.3 shows a typical mass spectrum obtained for the Pd surface of the "before sample" in the mass number range of 40 $-$ 70. Note that the mass numbers shown on the horizontal axis are not in proportional scale. A large signal on mass number 69 is for Ga which was used as a primary ion in TOF-SIMS.

Fig.4 shows a spectrum of the sample after the gas penetration. Increasing of the intensity for mass numbers 52, 53, 56, 63 and 65 can be seen. These mass numbers correspond to Cr (^{52}Cr, ^{53}Cr), Fe (^{56}Fe) and Cu (^{63}Cu, ^{65}Cu), respectively. The TOF-SIMS system is capable of removing the surface layers of the sample by Ga sputtering for surface cleaning and measurement of depth distribution. Fig.5 and Fig.6 show mass spectrum after 10s sputter cleaning by Ga^+ ion beam for the same area as Fig.3 and Fig.4, respectively. Increase in the intensity for mass numbers 52, 56, and 63 can be seen in Fig.6. These correspond to ^{52}Cr, ^{56}Fe and ^{63}Cu, respectively. We also found elements of mass number 55, 57, 58 and 65 only after experiments, which correspond to ^{55}Mn, ^{57}Fe, ^{58}Ni and ^{65}Cu, respectively.

Table 1-3 show the normalized intensity for the isotopes of Cr, Fe, and Cu at three areas on the sample with sputtering before and after gas penetration. Note that selected areas before experiment (a, b, c) are different from those analyzed after experiment (A, B, C). In Table 1, small amount of normalized count intensities for Cr isotopes was seen, and significant increase was observed at all three areas after experiment. Almost no count for mass number corresponding to Cr was seen before experiment, and increasing the intensity was found after experiment. For Fe and Cu isotopes, the normalized intensities were also increased apparently after experiment, as shown in Table 2 and 3. These results suggested that Cr, Fe, and Cu could have been produced during the gas penetration.

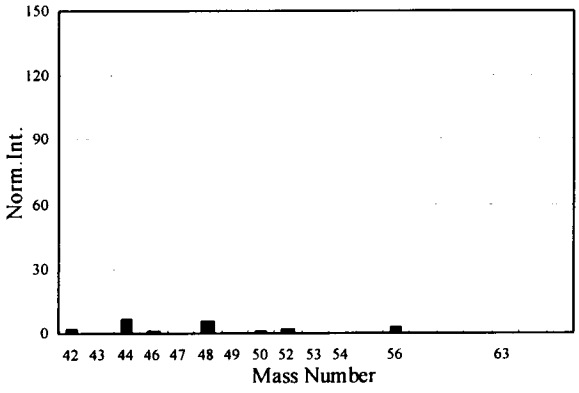

Fig.5 Normalized count intensity for mass number 40-70 for the sample before experiment. (10s sputter)

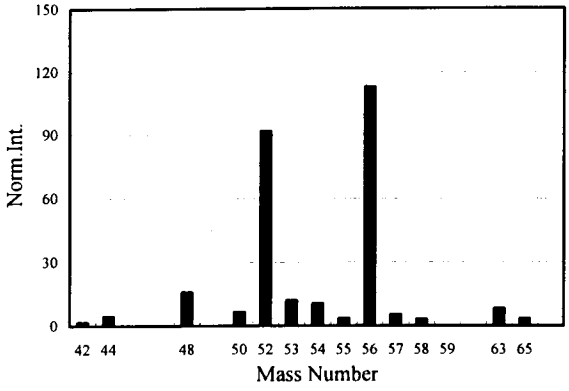

Fig.6 Normalized count intensity for mass number 40-70 for the sample after experiment. (10s sputter)

Before gas penetration

area	a	b	c
^{50}Cr	0	0	0
^{52}Cr	1.9	2.3	5.9
^{53}Cr	0.1	0.2	0.6

After gas penetration

area	A	B	C
^{50}Cr	3.6	6.5	10.8
^{52}Cr	27.3	91.8	29.0
^{53}Cr	3.4	12.0	3.7

Table 1 Normalized count intensity for the isotopes of Cr at three areas on the sample with sputtering before and after gas penetration. (10s sputter)

Before gas penetration

area	a	b	c
^{54}Fe	0.2	0.4	0.2
^{56}Fe	3.1	5.5	2.5
^{57}Fe	0	0	0

After gas penetration

area	A	B	C
^{54}Fe	2.7	10.5	3.8
^{56}Fe	28.6	113.1	42.7
^{57}Fe	1.6	5.3	2.4

Table 2 Normalized count intensity for the isotopes of Fe at three areas on the sample with sputtering before and after gas penetration. (10s sputter)

Before gas penetration

area	a	b	c
^{63}Cu	0.2	0.4	0.3
^{65}Cu	0	0	0

After gas penetration

area	A	B	C
^{63}Cu	9.5	8.2	12.9
^{65}Cu	5.2	3.4	5.4

Table 3 Normalized count intensity for the isotopes of Cu at three areas on the sample with sputtering before and after gas penetration. (10s sputter)

	^{50}Cr	^{52}Cr	^{53}Cr
natural ratio	4.45	85.82	9.73
A(After)	10.40	79.65	9.94
B (〃)	5.88	83.25	10.80
C (〃)	24.80	66.77	8.42

Table 4 Isotopic ratio of Cr (10s sputter)

	^{54}Fe	^{56}Fe	^{57}Fe
natural ratio	5.84	91.75	2.12
A(After)	8.22	86.84	4.94
B (〃)	8.13	87.76	4.11
C (〃)	7.82	87.23	4.95

Table 5 Isotopic ratio of Fe (10s sputter)

	^{63}Cu	^{65}Cu
natural ratio	69.17	30.83
A(After)	64.79	35.21
B (〃)	70.51	29.49
C (〃)	70.34	29.66

Table 6 Isotopic ratio of Cu (10s sputter)

	^{102}Pd	^{104}Pd	^{105}Pd
abundance	1.02	11.14	22.33
a(Before)	1.13	11.15	22.73
b (〃)	1.09	11.41	22.37
c (〃)	1.06	10.51	23.01
A(After)	0.98	10.84	22.82
B (〃)	1.06	11.42	22.10
C (〃)	1.17	11.01	22.86

	^{106}Pd	^{108}Pd	^{110}Pd
abundance	27.33	26.46	11.72
a(Before)	27.35	26.26	11.36
b (〃)	27.48	25.78	11.84
c (〃)	27.42	26.60	11.38
A(After)	27.23	26.43	11.69
B (〃)	26.76	26.88	11.75
C (〃)	27.31	26.24	11.40

Table 7 Isotopic abundance of Pd (10s sputter)

Table 4-6 show the isotopic ratio of Cr, Fe and Cu. In the isotopic ratio of Cr, difference from the natural one was observed in one of the three areas (Table 4), while no anomaly was seen for Fe and Cu (Table 5, 6). Table 7 shows isotopic abundance of Pd from SIMS data. The ratios both for "before" and "after" sample are consistent with natural ones.

4. Conclusion

We performed the hydrogen penetration experiment with Pd sample, and elements on the sample were surveyed before and after experiment. Increase in amount of Cr, Fe, Cu have been observed by making the hydrogen penetrate through Pd. These elements were possibly produced during the gas penetration. Mn and Ni were also detected on deeper regions revealed by the Ga^+ sputtering for 10s. These elements might have been produced by nuclear transmutation. The present results have strongly suggested that the reaction could have occurred in hydrogen system as well as deuterium system.

REFERENCES

[1]E.Yamaguchi, T.Nishioka, *Jpn.J.Appl. Phys.*, L.666 (1990)

[2]E.Yamaguchi, H.Sugiura, *Proceedings of 7-th International Conference on Cold Fusion,* p.420 (1998)

[3]Y.Iwamura, T.Itoh and M.Sakano *Proceedings of 8-th International Conference on Cold Fusion,* p.141 (2000)

[4]Y.Iwamura, M.Sakano and T.Itoh, *Jpn.J.Appl.Phys.*, Vol.41, pp.4642-4650 (2002)

[5]J.Dufour, D.Murat. X.Dufour and J.Foos, *Proceedings of 8-th International Conference on Cold Fusion,* p.153 (1998)

[6]T.Ohmori *Proceedings of 9-th International Conference on Cold Fusion* (2002)

Observation of Heat Evolution with Palladium Hydride in the Evacuated Chamber

N.Tanaka, S.Narita, H.Yamada, T.Nyui, H.Monma, M.Baba, E.Yamaguchi*

Department of Electrical and Electronic Engineering, Iwate University
*The 21st Century Public Policy Institute

ABSTRACT

The controlled gas out-diffusion method was employed to study nuclear reaction in matter using palladium hydrides with heterostructure (Pd:H/MnO*x* and Pd:H/Au) of various thickness. Anomalous heat evolution was observed during the experiment with explosive gas release from the sample. Time-resolved mass spectra by quadrupole mass spectroscopy showed that the released gas contained some amounts of T and ^{3}He might have been produced simultaneously with the heat evolution.
Keywords: Pd hydride, heat evolution, helium, tritium.

1. INTRODUCTION

Observation of heat evolution with deuterium or hydrogen loaded palladium (Pd), which can be easily recognized as a result of the anomalous nuclear reaction, has been reported in several different experiments [1-4]. Among them, Yamaguchi et al. reported excess heat production in the controlled gas out-diffusion method with Pd deuteride in the evacuated chamber ("in vacuo" method) [5, 6]. Yamada et al. suggested the possibility of tritium (T) production in similar experiment [7]. The method has advantages in the following respects: (i) gas diffusion from the sample can be stimulated by supplying electric current directly to the sample, (ii) temperature, pressure in the chamber, composition of diffused gas, radiation etc. can be measured simultaneously, (iii) contamination to the sample can be minimized, which enables high accurate analysis of nuclear products on the surface.

In this experiment, we examined the "in vacuo" method using Pd hydrides with heterostructure Pd/MnO*x* and Pd/Au by changing the thickness of Pd bulk and the films. Yamaguchi et al. have claimed that the heterostructure was one of the essential keys to trigger the phenomenon. Gas diffusion out of the sample can be blocked partially by MnO*x* layer and entirely by Au layer. Using such different materials, which gives the variety in motion of H atoms in Pd lattice, is helpful to understand the mechanism of the phenomenon. For Pd/Au sample, it can be washed by aqua regia even after depositing Au layer since it is hard to be affected by the acids. This process can remove the impurities on the sample contaminated in the process of film deposition and make a highly accurate analysis of the surface. This is an advantage for detecting small amount of nuclear products on the surface possible. The purpose of this study is finding the condition for the heat evolution and clarifying the mechanism of the reaction.

2. EXPERIMENT

2.1 SAMPLE PREPARATION

We prepared the square plate samples ($0.3\times12.5\times12.5$mm^3 or $0.1\times12.5\times12.5$mm^3) of Pd with 99.95% purity. It was washed by acetone and aqua regia. After that, one side of the Pd surface was coated with MnO*x* or Au film of $\sim$ 40nm thickness by sputtering in an argon working gas at 0.7 Torr. Then, the sample was loaded with hydrogen gas under 10atm pressure for 72 hours. The hydrogen gas for this experiment was of research grade in the purity. According to the specifics data given by the supplier, T and He components were not detected in the gas. The loading ratio (H/Pd) was measured to be about 0.7, typically.

2.2 EXPERIMENTAL SETUP

After loading with the gas, the sample was set into the stainless steel vacuum chamber. The chamber has a cylindrical shape with volume of 880cm^3 and can be evacuated by a turbo-molecular pump. The sample in the chamber can be observed through a quartz window during the experiment. The pressure in the chamber was measured by an ionization vacuum gauge (ANELVA: MIG-430). A DC power supplier supplied constant current to the sample through chrome steel clips in the chamber. A thermocouple was set on the rear side of the

sample opposite to the surface covered with the MnO*x* or the Au film to measure the sample temperature with an accuracy of ±1℃.

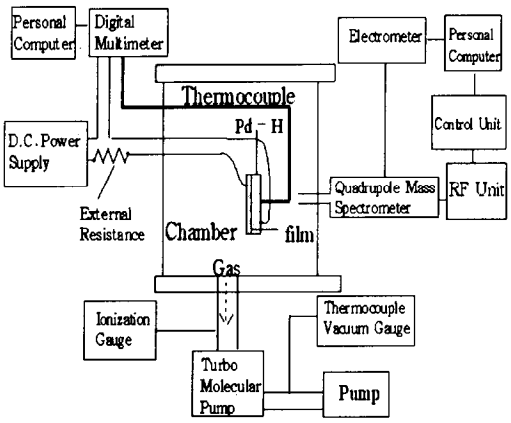

Fig1. Experimental apparatus

The gas in the chamber was analyzed by a quadrupole mass spectrometer (Q-mass) (ANELVA: AQA-100R). Current, voltage, and pressure in the chamber were observed simultaneously. The experimental apparatus is shown in Fig.1.

After evacuating the chamber to a pressure below 10^{-4}Pa, temperature and pressure in the chamber measurements were started. Composition of diffused gas for mass number less than 8 was analyzed. Then, the sample was supplied with an electric current of ~4A. The experiment continued for about 24-100 hours. The sample was taken out from the chamber after the current was stopped and weighted to estimate how much H atoms remained in.

3. RESULTS AND DISCUSSION

A typical time dependence of the surface temperature and the pressure in the chamber for the Pd:H/MnO*x* (0.3mm-thick Pd and 40nm-thick MnO*x*) sample is shown in Fig.2. The loading ratio for this sample was measured to be 0.75. Unexpected heat evolution started at ~2 hours after initiation of electric current supply, then it continued for about an hour. We observed such temperature increase in 9 out of 11 runs. Fig.3 shows a typical result for Pd:H/Au (0.3mm-thick Pd and 40nm-thick Au) sample. Temperature increased steeply at ~3.5 hours then dropped down gradually. For this case, the heat evolution was supposed to be continued for a short period. The difference in the temperature

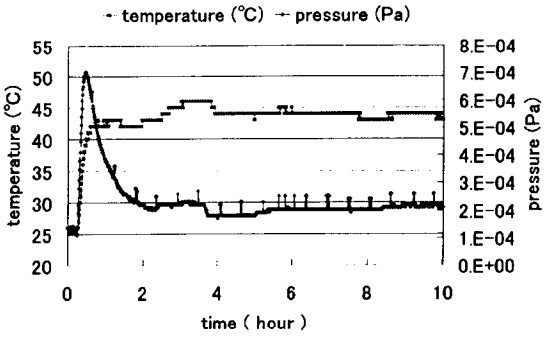

Fig.2 Typical time dependence of the temperature and pressure for Pd:H/MnO*x* (Pd:0. 3mm, MnO*x*: 40nm).

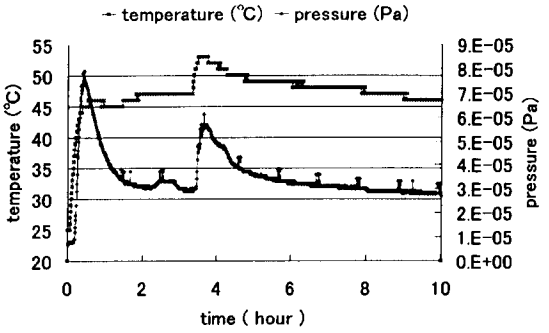

Fig.3 Typical time dependence of the temperature and pressure for Pd:H/Au (Pd:0. 3mm, Au: 40nm).

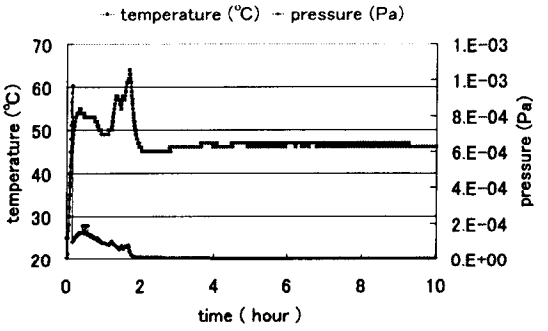

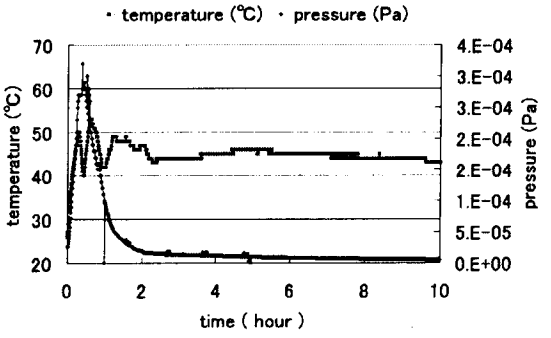

Fig.4 Tow typical time dependence of the temperature and the pressure for Pd:H/Au (Pd:0.1mm, Au:40nm).

The difference in the temperature behavior could be caused mainly by the difference in permeability of H atoms between MnO*x* and Au film. We observed the heat evolution in 7 out of 8 measurements for Pd:H/Au sample. For both types of sample, it was not due to Joule heat since voltage and current measured did not indicate a significant change before and after temperature rise.

Fig.4 shows two typical results for thinner samples (0.1mm Pd and 40nm Au film). Anomalous heat evolution was also observed for these samples. Our results showed that the heat evolution for the thinner sample happened earlier comparing with 0.3mm Pd sample, and more than once in a few hours. We are still investigating the effect of sample thickness to the temperature behavior. We will discuss this matter later. After the experiment, they were bent biaxially by uniform expansion of the side deposited MnO*x* or Au.

As shown in Fig2-Fig4, the pressure in the chamber showed explosive release of the gas simultaneously with the heat evolution. After the experiment, no gas remained in the sample. For the Pd:H/MnO*x* and Pd:H/Au sample, Fig.5 and Fig.6, respectively, show the temporal variation of the ion currents corresponding to the mass number of 1-6,12,16 and 18 measured with the Q-mass at the time around the temperature increase. The increase of ion currents for mass number 1-3 was observed, which was clearly coincident with gas release from the sample. The mass number 1 and 2 should correspond to H and H_2, respectively, and small amount of D, which might have existed originally in the Pd or the hydrogen gas itself as impurity. The mass number 3 corresponds to H_3, HD, T, and/or ^{3}He. If the atoms with the mass number of 3 were originated only from H and D, the ion current should show the same behavior or smaller increase than that for mass number 1 and 2. However the ion current for mass number 3 showed slightly larger increase. Hence, the atoms with the mass number of 3 include not only H_3 and HD but also T and/or ^{3}He. The ion currents for mass number of 4,5 and 6, which correspond to D_2 and/or HT, DT and T_2, respectively, also increased. This was another evidence of T production. Q-mass measurements of the partial pressure in the chamber at the beginning of the experiment revealed absence of the molecules with the mass number 4-6. Consequently, it was possible that T or both T and ^{3}He were produced concurrently with the heat evolution. The Q-mass used in the present experiments cannot distinguish T from ^{3}He.

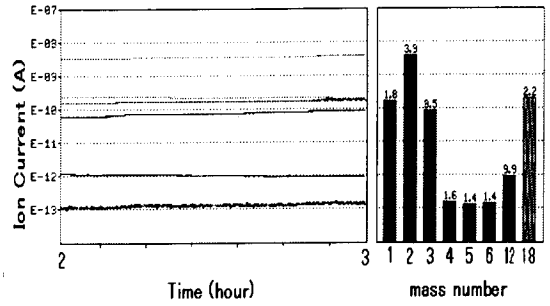

Fig.5 Time behavior of ion currents for mass number 1-6, 12, 18 for Pd:H/MnOχ (Pd:0.3mm, MnO*x*:40nm).

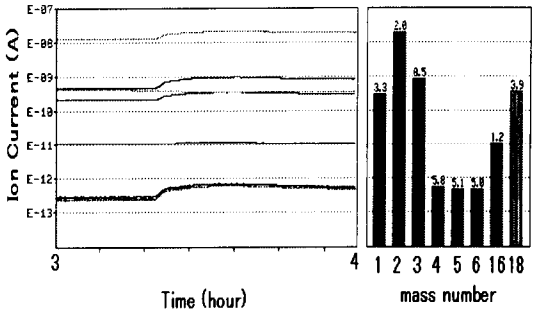

Fig.6 Time behavior of ion currents for mass number 1-6, 16,18 for Pd:H/Au (Pd:0.3mm, Au:40nm)

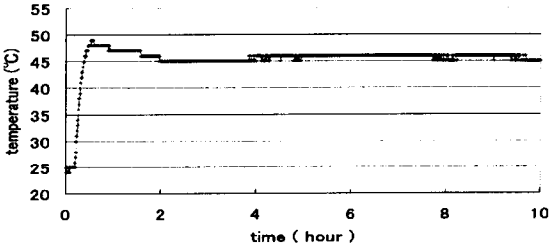

Fig.7 Time dependence of the temperature for Pd/Au (Pd:0.3mm, Au:40nm thickness)

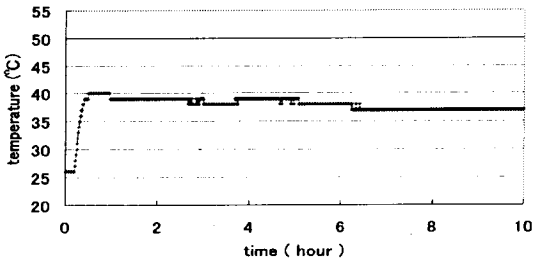

Fig.8 Time dependence of the temperature for Pd:H sample without MnO*x* nor Au layer.

Fig.7 shows temperature behavior for Pd/Au (0.3mm Pd and 40nm Au) without loading hydrogen. After temperature increase in the initial stage by Joule heat, no anomaly was observed. Also we performed several experiments using plain Pd:H (0.3mm Pd) sample, that is, without sputtering MnO*x* nor Au film. A typical time dependence of the surface temperature is shown in Fig.8. No anomalous heat evolution was observed. For the sample, the loading ratio was measured to be 0.73. The same results were obtained for the plain Pd with 0.1mm thickness. It turned out that the heterostructure is necessary to induce the phenomenon in this system. Yamaguchi et al. claimed that the heat evolution was related to structural phase transition in the Pd, and the heterostructure played an important role in the process, that is to provide high stress field [6]. Our result, that is no anomaly was observed for just Pd:H sample, supported their prediction. This speculation may also explain the difference in temperature behavior between 0.3mm and 0.1mm thickness samples, which was described above.

4. CONCLUSION

We have successfully confirmed the reproducible anomalous heat evolution in the controlled gas out-diffusion ("in vacuo") method with heterostructure Pd hydride sample, Pd:H/MnO*x* and Pd:H/Au. Analysis of the time resolved mass spectra has clarified that the heat evolution was reated to the generation of the atoms with the mass number of 3, which could correspond to T and/or ^{3}He. We will try to distinguish these in the future study.

Further numerous experiments are needed with various conditions (for example, changing thickness of film, type of heterostructure, etc.) to understand the mechanism of the phenomena. We also need to understand transformation of sample during the experiment, which is supposed to be concerned with the heat evolution process. In the future study, we will evaluate the excess power from the temperature rise assuming some calorimetric models. This is highly desirable for utilizing the power. In addition, we will search for nuclear products by analyzing the sample surface before and after experiments, which can give us a proof of the nuclear transmutation.

REFERENCES

[1] M.Fleischmann, S.Pons, J.Electroanal. Chem., 261, p.301 (1989)
[2] M.McKubre et al., Proceedings of 8-th International Conference on Cold Fusion, p.3 (2000)
[3] G.Miley et at., Proceedings of 8-th International Conference on Cold Fusion, p.169 (2000)
[4] G.Agelao et al., Fusion Technology, 38, p.224 (2000)
[5] E.Yamaguchi, T.Nishioka, Japanese J. Appl. Phys., L.666 (1990)
[6] E.Yamaguchi, H.Sugiura, Proceedings of 7-th International Conference on Cold Fusion, p.420 (1998)
[7] H.Yamada et al., Proceedings of 8-th International Conference on Cold Fusion, p.241 (2000)

Gamma Ray Measurement and Surface Analysis on Deuterated and Hydrated Palladium Electrode under DC Glow-like Discharge.

Naoki SATO, Ryotaro ITO, Alban ARAPI, Daiju KATO,
Shinya NARITA, Minoru ITAGAKI and Hiroshi YAMADA
Faculty of Engineering, Iwate University, Morioka 020-8551, Japan

ABSTRACT
The gamma rays with different energy from deuterated palladium electrodes subjected to DC glow-like discharge is reported. Elements as well as their isotopic distribution on/in the Pd cathodes before and after experiments were investigated by time-of-flight secondary ion mass spectrometry (TOF-SIMS). Barium was detected on the Pd hydride cathodes after DC glow discharge experiment.
KEYWORDS: glow-like discharge, gamma ray, isotopic distribution, nuclear reaction.

1. INTRODUCTION

The possibility of inducing nuclear reactions at low temperature in solid-state materials has been widely investigated for several years by the electric discharges experiments. Previously we have reported observation of the low-energy gamma emissions with 70-110 keV and the detection of the significant amount of Be on/in Pd cathode during DC glow discharge[1, 2]. Gamma emissions in the energy range of 0.1-3MeV and excess heat were observed in experiments with a high current glow discharge.[3] As electric discharges method involves less contamination than other methods, the attention is given on element analysis which gives an important information in this study. For this reason each sample's composition was analyzed before and after DC discharge by TOF-SIMS. Anywhere only elements that were not introduced at all to the Pd samples before experiments are considered as strong evidence of occurrence of nuclear reaction. In this study, we report the detection of the emissions of gamma rays with different energy during the glow-like discharge and the transmutation of elements in the Pd cathode exposed to the electric discharges.

2. EXPERIMENT

The experiments were carried out by DC glow discharge and DC glow-like discharge with palladium (Pd) metal as a cathode in hydrogen or deuterium atmosphere. The Pd sample (0.1mm in thickness, 99.95% pure) used for the experiment was cut in size of 10x10mm. Each Pd sample was washed with aqua regia for 100s and then its composition was analyzed by TOF-SIMS. This analysis allowed us to know the accurate composition of impurity elements on/in the flesh Pd cathode. Absorption of proton or deuteron in the Pd electrodes was performed by the gas loading method, which allowed less impurities to be involved in the sample than other ones. The samples were put into the loading chamber. The chamber was evacuated at 10^{-3}Torr and then filled with hydrogen or deuterium at 5 or 10atm, respectively, for ~48[h]. The loading ratio was determined to be 0.6-0.7 by measuring mass change of the samples. Then the samples were moved out of the chamber and placed in a discharge test cell.

Fig. 1 shows the discharge test cell. The cell is made of Pyrex glass, which consists of two parts, adhered closely by silicone grease (Dow Corning) that is capable of keeping the discharge space in a vacuum of required pressures. Two adapters and valve were jointed to the upper part of the cell. An Au foil was used as the anode and a Pd foil as the cathode. The cathode was supported by an Au wire with a quartz cylinder surrounding it to avoid any movement of the samples during the experiments. The gap distance between two electrodes was 10mm. The advantage of using Pyrex glass material compared with metal is that there are fewer possibilities for palladium

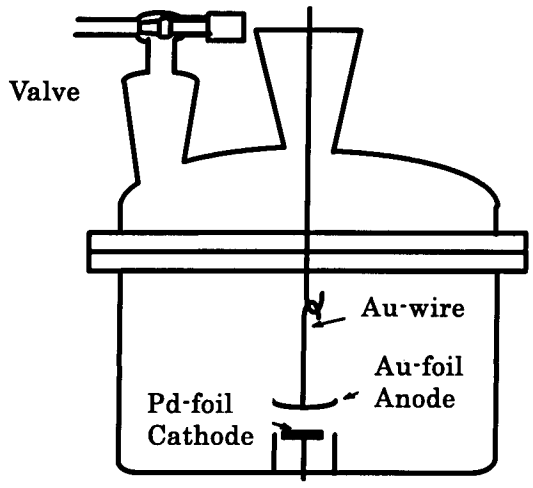

Fig.1: Discharge test cell

samples to be contaminated during the sputtering process by DC glow discharge and DC glow-like discharge.

The samples were exposed to DC glow-like discharge with currents of 2-4mA, voltage of 4000-6000V and pressure of ~1atm for a duration time of 60min. and DC glow discharge with currents of ~2mA, voltage of 600-800[V] and pressure of 3-30Torr for duration times of 30, 60, 90min. In total, 30 Pd cathode samples for the D-Pd system and 20 Pd cathode samples for the H-Pd system were exposed to DC glow-like discharge. Moreover, the DC glow discharge experiments were performed 37 times and 23 times for both D-Pd and H-PD systems, respectively. A NaI scintillation counter was used to detect the gamma ray emitted from the samples. The counter was set perpendicular to the wall of the cell. After the DC glow-like discharge treatment and DC glow discharge treatment, the composition of the Pd samples were investigated again by TOF-SIMS.

3. RESULTS and DISCUSSION

3.1 GAMMA RAY MEASUREMENT

Fig.2 shows a gamma ray spectrum for background. The spectrum of background was measured without discharging for 60min. Although the background spectrum is rather noisy, changers in the energy spectra shown below are observed only under the limited conditions, and their magnitude is much greater than the fluctuation level. The energy calibration was executed by using two gamma-ray sources such as ^{57}Co (122.0keV) and ^{137}Cs (661.5keV).

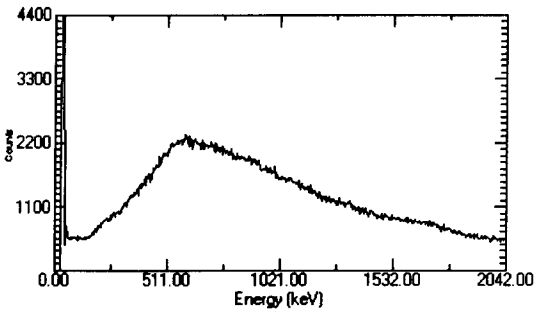

Fig.2: Gamma ray spectrum for background. A vertical axis shows the counts and a horizontal axis energy.

During DC glow-like discharge experiments using deuterium gas, spectra that

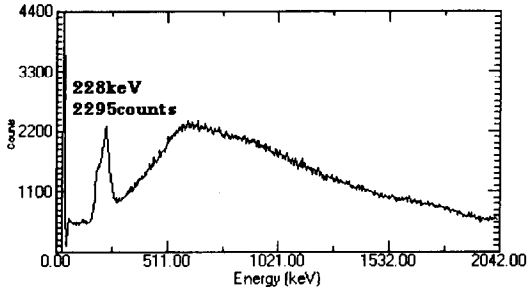

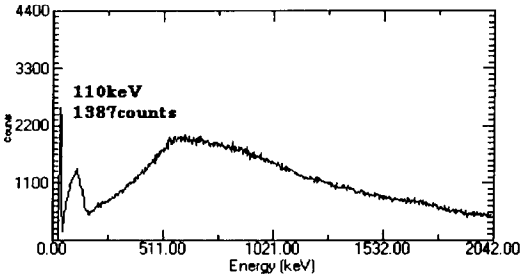

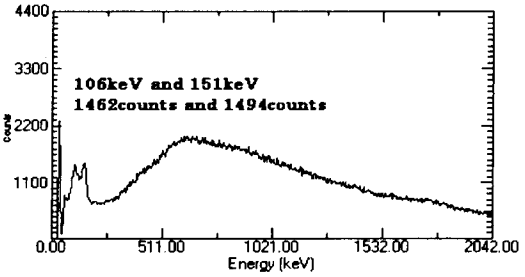

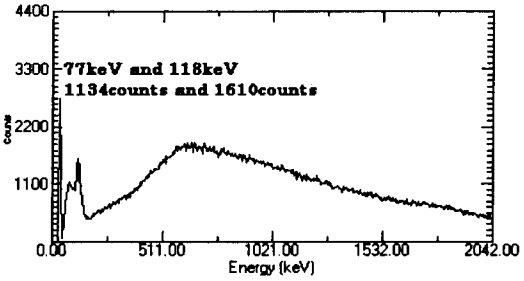

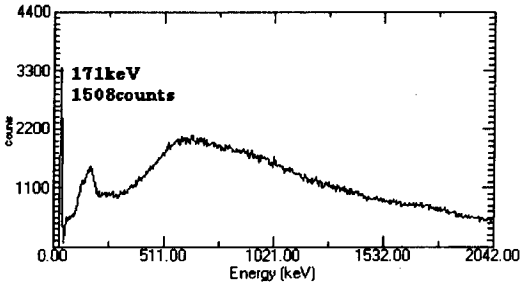

Fig.3: The anomalous peaks in the gamma ray spectrum.
The peaks correspond to 228keV, 110keV, 106 and 151keV, 77 and 118keV, and 171keV

are different from the background were observed in 5 out of 30 runs. The spectra are shown in Fig.3. The anomalous peaks in the gamma ray spectra correspond to 228keV, 110keV, 106 and 151keV, 77 and 118keV, 171keV. These peaks were registered in 10-20min after DC glow-like discharge has started. The same experiments were performed for the H-Pd system, which showed gamma ray spectra similar to the background one. Note that we did not detect any gamma ray emissions during DC glow discharge experiments for a H-Pd system. Moreover, when no-loading Pd sample were exposed to the DC glow-like discharge with deuterium or air gas (the so-called blank experiments), such anomalous spectra were not observed at all. It is thought that these signals could not be noise introduced by the electric discharges and that some nuclear reactions, producing gamma ray, took place during DC glow-like discharge experiment. Furthermore, since such signals were not observed at all for H-Pd system, deuterium might have played an important role in the generation of the gamma ray during the nuclear reactions.

3.2 SURFACE ANALYSIS

The surface composition of palladium cathode was analyzed before and after DC glow discharge or DC glow-like discharge experiments by TOF-SIMS. The analysis of the element composition was made at the different areas (40x40μm for each) on/in the Pd cathode samples with the result that the composition was found to be almost the same for every area. Note that the selected areas before the experiment are different from those analyzed after the experiment. The analysis was made using count intensities or normalized intensities of signals, but not real quantities of the elements. The normalized intensity defined here is 10^4 times the numerical value obtained by dividing count of mass of each element by total count of signals to normalize.

During DC glow discharge experiment (D-Pd system, 3Torr, 60min), a remarkable increase in counts for ^{56}Fe was observed. Fig.4 shows the normalized intensities of ^{56}Fe for a sample analyzed by TOF-SIMS before absorption and after glow discharge experiment. Such a remarkable increase was detected only when the data were collected after 30 seconds of sputter cleaning by Ga^+ ion. Ohmori *et al.*[4] also observed Fe production by means of electrolysis with an Au electrode.

After the DC glow-like discharge (D-Pd system), a change in isotopic distribution of Mg, although at one area out of three detecting areas of a sample, was observed on the surface exposed to the discharge, which is shown in Fig. 5. Mg isotopes with isotopic distribution similar to natural one were observed on the so-called blank samples and on the samples analyzed before experiment. Moreover, the peak in the gamma ray spectrum, corresponding to 228keV, has been observed using this Pd sample before the TOF-SIMS analysis was performed. Mizuno and coworkers [5, 6] have demonstrated the production of elements, during electrolysis, in a mass number range of 1-208 with an isotopic distribution quite different from the natural one. The emission of 228keV gamma ray related with a change of the isotopic distribution of Mg on the Pd sample (228keV sample) suggests that nuclear reactions might

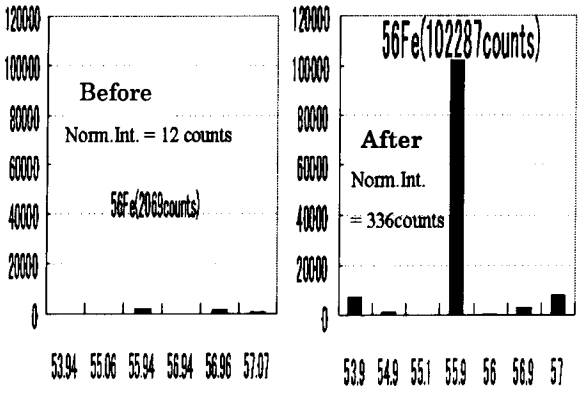

Fig.4: Comparison of ^{56}Fe before (left) and after (right) the experiment.

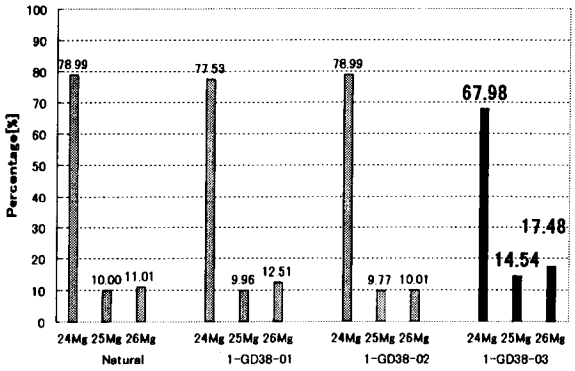

Fig.5: Isotopic distribution of the Mg compared with natural abundance. (1-GD38 is sample name. 1-GD 38-01, 02 and 03 indicate arbitrary three points.)

have occurred. However, since such a change was observed only for this sample, further examinations are needed.

The DC glow discharge experiments were performed for the H-Pd system. By analyzing the obtained data, it was found that Ba was detected as new element. For the background sample, no signals corresponding to this element were detected. This result makes us confirm that Ba emerges on the Pd sample only via the glow discharge process. In addition, slight increases of Fe and Cu were observed. Savvatimova *et al.*[7] have reported the production of different elements with atomic mass numbers smaller and larger than Pd isotopes during glow discharge using deuterium or hydrogen gas. Ba was detected clearly on both the uppermost and the sputtering areas of the sample after the glow discharge experiment. Comparison of Ba before with that after the experiment is shown in Fig. 6. In Fig.6, the number in the vertical axis shows the normalized intensity, the numbers 1-4 in the horizontal axis shows the detection points in a Pd sample before the experiment, the numbers 5-7 and 8-10 show the detection points on the sample after DC glow discharge for the uppermost area and the sputtering area, respectively. All Ba isotopes were detected on the sample for H-Pd system and the isotopic distribution of Ba is almost the same as natural isotopic distribution.

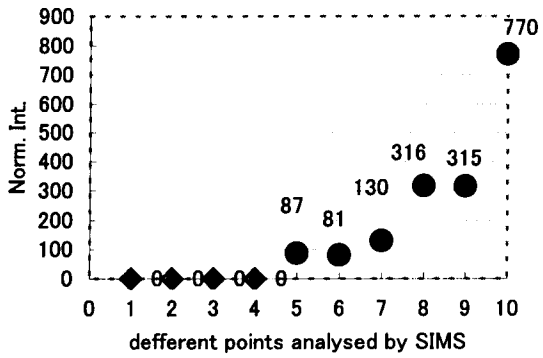

Fig6: Comparison of Ba intensity before experiment and that after the experiment. Details of detection point of horizontal axis.

1-4: Before the experiment
5-10: After the experiment
1-2: No sputter
3-4: 10s sputter
5-7: No sputter
8-10: 10s sputter

SUMMARY

Gamma rays with different energy were detected during DC glow-like discharge in deuterium atmosphere. The absence of gamma emissions during experiment using hydrogen gas suggests that deuterium might play an important role during experiment. The 228keV sample showed that an isotopic distribution of Mg was sometimes different compared with natural isotopic distribution.

The detection of the Ba on/in the Pd cathode after the glow discharge could imply that some nuclear reaction of protons and Pd atoms has taken place. We observed significant increases in the counts of ^{56}Fe that reinforced the possibility of nuclear origin for the production. However these elements are also impurities possibly coming from environment since they are common elements in the natural environment.

References

1 H. Yamada et al., Fusion Technol. **39** 253 (2001).
2. A.Arapi et al., Jpn. J. Appl. Phys, **41**, L1181 (2002)
3. A. B. Karabut: Proc 8th Int. Conf. Cold Fusion p. 329 (2000)
4. T. Ohmori et al., Fusion Technol. **31**, 210 (1997)
5. T. Mizuno et al., Proc 6th Int. Conf. Cold Fusion p665 (1996)
6. T. Mizuno: Nuclear Transmutation: The reality of Cold Fusion, pp. 128-133 (1998)
7. I.B. Savvatimova et al., Fusion Technol. **26**, 389 (1994)

ANOTHER EXPLANATION OF PIPE RUPTURE INCIDENT AT HAMAOKA NUCLEAR POWER STATION UNIT-1 FROM VIEW POINT OF COLD FUSION

Hiroshi YAMAMOTO
Free Journalist
17-5 Fujimi-dai Iwata, Shizuoka- Pref. Zip 438-0088, Japan
Tel: 81-538-32-4584, e-mail: hughy@aqua.ocn.ne.jp

Abstract: An extraordinary powerful explosion took place at the Hamaoka nuclear power station unit-1 of Chubu Electric Power Company in Nov. 2001, resulting in a pipe rapture of the steam condensation line of the residual heat removal system. The cause of the incident is said to be hydrogen explosion, namely, combustion of stoichiometric mixture of hydrogen and oxygen accumulated in the residual heat removal (RHR) system. Intensive research works have been carried out to reconstruct this strange combustion phenomenon but it seems the reports failed to explain this anomalous combustion. Randell Mills developed "BlackLight Process" starting in 1986 that can explain excess heat in the absence of nuclear products in the research of cold fusion. It was reported [1] that there exist several anomalous combustion phenomena which can not be explained by current theories but can be explained by the BlackLight Process. The Black Light Process was applied to this incident and it was shown that the BlackLight Process can explain the pipe rapture incident at Hamaoka Nuclear Power Station more clearly.
Key words: hydrogen explosion, high concentration of hydrogen and oxygen, Hydrino

1. INTRODUCTION

An extraordinary powerful explosion took place at the Hamaoka nuclear power station unit-1 of Chubu Electric Power Company in Nov. 2001, resulting in a pipe rapture of the steam condensation line of the residual heat removal (RHR) system. Intensive research works have been carried out to reconstruct this strange combustion phenomenon and the final report was published. The cause of the incident is said to be hydrogen explosion, namely, combustion of stoichiometric mixture of hydrogen and oxygen accumulated in the RHR system. A close examination of this report revealed that there were a couple of wrong assumption in the calculation of gas generation process during steam condensation and another explanation is needed.

2. PIPE RAPTURE MECHANISM

According to the report prepared by Nuclear and Industrial Safety Agency (NISA), Ministry of Economy, Trade and Industry (METI), JAPAN, the mechanism of pipe rapture can be illustrated as is shown in Fig.1 and can be summarized as follows [2].

(1) The main steam contains hydrogen and oxygen generated by radiolysis of reactor water. The RHR steam condensation line at Hamaoka-1 features a very long and upward pipe with the dead-end section. In such a piping layout, a temperature gradient is produced throughout the piping system. Therefore, the steam condensation by heat release from the pipe allows non-condensable gas to gradually accumulate at the upward dead-end pipe section and the separation takes place between high-temperature steam region and low-temperature non-condensable gas region. The results from the experiments and the analyses showed that non-condensable gas had accumulated in the upward dead-end pipe section (about 7-m length from the holdup water surface in the pipe).

(2) The hydrogen combustion might have been caused by the pressure transient induced by the inflow of high-temperature steam to non-condensable gas region, due to the opening of the valve for the periodical inspection. It is possible that the noble metals attached to the inner surface of pipe acted as a catalyst.

(3) The ignition of non-condensable gas was followed by its combustion that propagated toward downstream and shifted from normal combustion to detonation. Pressure in the pipe increased rapidly in the meantime, causing the rupture of the elbow containing the holdup water.

3. ACCUMULATED GAS CONTENTS

Chubu Electric Company has been operating 4 nuclear power plants at Hamaoka. The unit-1 (in which the incident took place) and unit-2 are boiled water reactor and have a very similar operating history including injection of hydrogen and noble metal catalysts into cooling water to prevent stress corrosion cracking of internal parts made of steel alloy. After the incident, non-condensable gasses of the unit-2 that were accumulated at the upward dead end of the pipe

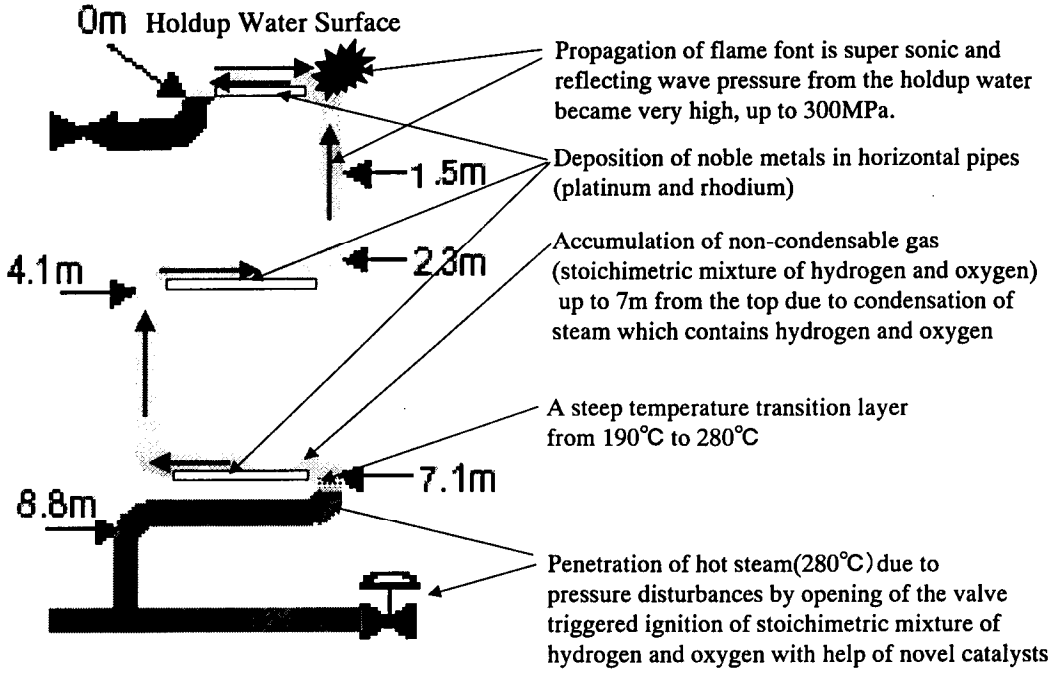

Fig. 1 Mechanism of hydrogen explosion according to Chubu Electric Company

	A: Residual gases from previous cycle *Initial condition*	B: Calculated gas generation by Chubu	C: Calculated gas contents in pipe by Chubu		D: Measured Gases	E: Calculated gas generation based on A&D
Gases	mol	mol	mol	%	%	mol
Hydrogen	0	**63.7**	63.7	**41.9**	**45.1**	**62.29**
Oxygen	11.9	**31.9**	43.8	**28.8**	**22.5**	**19.15**
Nitrogen	44.7		44.7	**29.4**	**32.4**	
Sum	56.6	95.6			100	81.44

Table 1 Gas contents in the pipe

were taken and its contents were measured. Also, the company carried out the calculation of non-condensable gas generation by computer simulation program and confirmed the validity of the simulation program using a test rig similar to the existing pipe. But it should be noted that amount of gasses thus calculated depends on the initial assumption how much the concentration of hydrogen and oxygen are in the steam. The table 1 shows mol and percentage of hydrogen and oxygen that were calculated and also measured on the unit-2.

Column A is the carried over gasses in mol from the previous cycle
Column B is the gasses in mol calculated by computer simulation program
Column C is the combination of A & B which the company thought were present in the pipe.
Column D is the measured gas concentration in percentage.
Column E is the gas quantity required to have Column D, starting from the initial condition of Column A.

4. QUESTIONS ON THE CLAIMS BY CHUBU ELECTRIC COMPANY

Chubu Electric Company claims that its calculation results of hydrogen and oxygen in % in C are generally in agreement with measured one (D). But if we compare the hydrogen contents of 41.8% in C with 45.1% of the measured one in D, the difference is minus 3.2%. On the other hand, if we compare the oxygen contents of 28.8% in C with 22.5% of the measured one in D, the difference is plus 6.3% and its direction of the differences is opposite to the case of hydrogen. The quantity of hydrogen and oxygen in C calculated by Chubu is decided by the initial assumption how much hydrogen and oxygen are contained in the hot steam. Chubu assumed that the concentration of hydrogen and oxygen in the steam were 2ppm and 16ppm respectively which gives rise to the gas generation ratio of hydrogen 2 and oxygen 1, but as was shown in the above examination, this assumption seems wrong. Rather simple calculation gives hydrogen and oxygen in mol which are necessary to have the measured gases in D when started from A, as shown in E. When we compare column B with E, we can notice that hydrogen is in good agreement but oxygen is not. In other words, generation of oxygen must be much smaller than 31.9 mol in B. This suggests that Chubu assumed too much concentration of oxygen in the steam and also ignored the re-combination of hydrogen and oxygen with the help of noble metals on the pipe wall. The total gas generation in E is 81.44 mol and this is 15% less than the calculated one in B. The operating hours of Unit-1 after the previous periodical inspection to the accident is almost 2.5 times longer than that of Unit-2, it can be assumed that more re-combination of hydrogen and oxygen took place in Unit-1. This suggests that non-condensable gas in the unit-1 didn't reach 7m from the top dead end section. All these examinations put the pipe rapture mechanism by Chubu in a serious doubt and necessitate developing a new mechanism for the pipe rapture incident.

5. HYDRINO HYPOTHESIS

There are several scientists who claim that an electron with lower energy states than the ground electronic state is possible in the hydrogen atom. Randlle Mills, one of these scientists, demonstrated that hydrogen atoms can achieve lower states than ground state by a resonant collision with a near by atom or combination of atoms having the capability to absorb the energy to effect the transition, namely, an integer multiple of the potential energy of the electron at ground state of the atomic hydrogen, $m \times 27.2eV$ (m=integer) [3]. He succeeded in generating energy somewhat between chemical and nuclear reaction using several elements such as potassium and helium as catalysts to make this transition happen. He named this shrunken hydrogen atom "Hydrino" and claims that this Hydrino can be a catalyst to shrink other Hydrinos to further lower states.

6. A CATALYTIC ROLE OF OXYGEN IN ANOMALOUS HEAT GENERATION

The author postulated that atomic oxygen can be a good catalyst for "hydrinos" generation because ionization energy of hydrogen and oxygen is very close as is shown below.

Hydrogen =13.598 eV, Oxygen =13.618 eV

It can be expected that the following reactions can take place in the environment in which atomic hydrogen and oxygen can co-exist.

$O + O + H \rightarrow H[n=1/2] + 2\,O^{+} + 2\,e^{-}$ ----(1)

$H + H + O \rightarrow H[n=1/2] + H^{+} + O^{+} + 2e^{-}$ -----(2)

$H + H + H \rightarrow H[n=1/2] + 2\,H^{+} + 2\,e^{-}$ ----(3)

$D + D + D \rightarrow D[n=1/2] + 2\,D^{+} + 2\,e^{-}$ ----(4)

$D + D + O \rightarrow D[n=1/2] + D^{+} + O^{+} + 2\,e^{-}$ ---(5)

$D + O + O \rightarrow D[n=1/2] + 2\,O^{+} + 2\,e^{-}$ ----(6)

H[n=1/2], D[n=1/2] designates a hydrogen and a deuterium whose electron orbit is shrunken to 1/2 the radius of a normal one and these will be shrunken further as reactions continue. Ions and electrons thus generated will re-combine, resulting in the formation

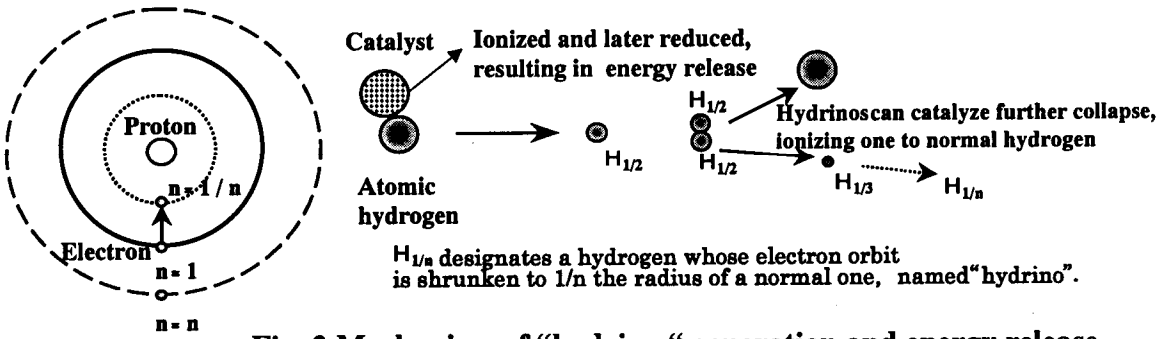

Fig. 2 Mechanism of "hydrino " generation and energy release

of oxygen as is shown in the following equation.

$2O^{+} + 2e^{-} \rightarrow 2O$ -----(7)

Then, the net reaction is :

$H \rightarrow H[n=1/2] + 40.8eV$ -----(8)

40.8eV is the energy difference of the electron at the ground state n=1 and n=1/2 state.

H[n=1/2] can be catalyst for further step as is shown in Fig 2.

It had been shown that this postulation can be applied to the explanation of several anomalous combustion phenomena that cannot be explained by current theories, such as stoichiometric mixture of hydrogen and oxygen, known as Brown's gas and air-less combustion of emulsified fuels and others[1].

It had also been shown that this postulation can be applied to the explanation of anomalous heat generation of proton conductive ceramics and nuclear transmutation induced by calcium oxide [4].

Recently, it was shown that molecule oxygen can be also a good catalyst for Hydrino generation because molecular oxygen will be undergone the following reaction[5].

$O2 + 54.4eV \rightarrow O^{2+} + O + 2e^{-}$ -----(9)

Then, the following reaction is possible.

$H + O2 \rightarrow H[n=1/2] + O^{2+} + O + 2e^{-}$ ---(10)

7. PROPOSED MECHANISM OF ANOMALOUS EXPLOSION AT THE HAMAOKA NUCLEAR POWER STATION

The steam condensation by heat release from the pipe resulted in accumulation of hydrogen and oxygen at the upward dead-end pipe section. At the surface of noble metals such as platinum and rhodium that are deposited on the horizontal part of the pipe, molecular hydrogen and oxygen will be divided into atoms. This enhances the re-combination of hydrogen and oxygen, in other words, catalytic combustion but due to the small amount of noble metals, there existed plenty hydrogen and oxygen in the upper part of the pipe. In this circumstance, there are a lot of chances for atomic hydrogen to collide with molecular oxygen and with 2 atomic oxygen simultaneously. These reactions can generate somewhat between chemical and nuclear reaction, in other words far more energy than normal combustion of hydrogen. Judging from the latest report made by the NASA funded project [6], it can be conceivable that the explosion could be strong enough to break the pipe spontaneously, because the density of hydrogen in the RHR system is over 4 order higher than that of the NASA funded project.

8. HYDROGEN EXPLOSION AT SRI IN 1992

The pipe rapture incident at Hamaoka reminds us of a very powerful explosion during a cold fusion experiment at Stanford Research Institute in 1992. At that time, there were no knowledge about the above mentioned combustion mechanism, so it is only natural to conclude the incident was just a hydrogen explosion, as long as there are no nuclear ash. But, after knowing it, it is strongly recommended to revisit this incident from a new stand point of view described in this paper.

SUMMARY

1 The Chubu's report on the incident is based on a wish-full assumption such as high concentration of hydrogen and oxygen in steam, no consideration of re-combination of hydrogen and oxygen in the RHR system, and can hardly explain the mechanism of the anomalous explosion of the pipe rapture.

2 High concentration of hydrogen and oxygen on platinum and rhodium at the top corner of the pipe was optimum condition to have Randdle Mills' BlackLight process and judging from the past successful application of this process to other anomalous combustion phenomena, it can be expected that his process can be applicable to the this incident.

3 Re-visiting the incident of explosion at SRI in 1992 from this new view point is strongly recommended.

REFERENCE

(1) Yamamoto, H., Explanation of Anomalous Combustion of Brown's Gas using Dr. Mills' Hydrino Theory , SAE1999-01-3325, 1999

(2) Nuclear and Industrial Safety Agency (NISA), Ministry of Economy, Trade and Industry (METI), JAPAN, Investigation Report on Pipe Rupture Incident at Hamaoka Nuclear Power Station Unit-1, July 2002

(3) Mills, R. The Grand Unified Theory of Classical Quantum Mechanics, Blacklight Power Inc.,1999

(4) Yamamoto, H, A Catalytic Role of Atomic Oxygen on Anomalous Heat Generation Induced in Proton Conductive Ceramics under Hydrogen Atmosphere, JCF2 Abstract NO.25, 2000

(5) Mills, R, et.al., Novel Catalytic Reaction of Hydrogen as a Potential New Energy Source, U.S. Environmental Protection Agency Sustainable Technologies Division Seminar Series, Oct. 24, 2002, Cincinnati, Ohio

(6) Marchese, A, et.al., The Blacklight Rocket Engine, a Phase I Study Funded By The NASA Institute For Advanced Concepts Phase I Final Presentation, October 25, 2002

Analysis on neutron induced fission of ^{235}U by SCS model

Masayuki Ohta and Akito Takahashi

Department of Nuclear Engineering, Osaka University
Yamadaoka 2-1, Suita, Osaka, 565-0871, JAPAN

ABSTRACT

We have calculated the nuclear transmutation of W, Au and Pd by the multi-photon induced fission (MPIF) and the selective channel scission (SCS) models. To check the estimation of fission product (FP) yields calculated by SCS model, the change of FP yields from n+^{235}U reaction for incident neutron energies was analyzed by SCS model.

FP yields for thermal and 1 MeV neutron-induced fissions of ^{235}U were analyzed by considering proper channel-dependent fission barriers including the tunnel fission effect. FP yield for thermal neutron showed a good agreement not only in mass-distribution but also in two-dimensional plot of atomic number and mass and FP yields. And FP yield for 14 MeV neutron-induced fission of ^{235}U were analyzed approximately. The incident neutron energy dependence of FP yields for ^{235}U was understood consistently. We obtained a good consistency between the SCS model and the multimodal random-neck rupture model.

Keywords: selective channel scission, fission, nuclear transmutation, channel-dependent fission barrier

1. INTRODUCTION

We have analyzed the nuclear transmutation of W, Au and Pd by the multi-photon induced fission (MPIF) and the selective channel scission (SCS) models.[1] In the process of this analysis, the evaluation of calculation method in SCS model, in particular, of the effective scission distance, is needed. We have analyzed a famous neutron-induced fission of ^{235}U to evaluate and to improve SCS model.[2]

For the fission of U, several models for fission analysis have been proposed.[3–5] Recently, the five-dimensional analysis of nuclear fission modes and fragment mass asymmetries was carried out.[6] And the multimodal random neck-rupture model[7,8] is well known as one that supposes a few shapes of nuclei at scission and paths of deformation (modes) and treats the scission of neck by a Gaussian distribution. This model can explain fission properties well phenomenologically, but is not able to predict the fission products (FPs) for arbitrary nuclides. Therefore, this model is ineffective for W, Au and Pd fission analysis.

We have proposed SCS model and have analyzed the FP yield from ^{235}U fission induced by thermal neutron.[1,2] SCS model treats the fission by the concept of channel dependent fission barriers for all scission channels. The reason why the mass-distribution of FP yield from thermal neutron fission of ^{235}U has two humps could be understood by SCS model.[2]

But the valley part of FP yields of ^{235}U has not corresponded to the experimental data in detail for the change of incident neutron energies. The calculation method of SCS model is improved to analyze this change of valley part of FP yields by one parameter fitting that concerns the effective scission distance.

2. MODEL

SCS model is based on the liquid drop model that is suitable and has been used by many authors to treat the mechanism of fission. The fission process by the SCS model, that is shown in Fig.1 (a), is characterized by the energy change ΔE of nuclear liquid drop in the elliptic deformation of the nuclei[9] and the bare Coulomb potential energy after scission V_c.

$$\Delta E = \epsilon^2 \left(6.88 \mathrm{A}^{2/3} - 0.1398 \frac{\mathrm{Z}^2}{\mathrm{A}^{1/3}} \right), \quad (1)$$

$$V_c = 1.44 \, \mathrm{Z}_1 \mathrm{Z}_2 / r, \quad (2)$$

in MeV and fm,

where the distance between fission product 1 (FP1) and fission product 2 (FP2) is defined by $r = |r_1 - r_2|$. The elliptic coefficient is $\epsilon = (R_1 + R_2 + r - 2R_0)/(2R_0)$, where R_0, R_1 and R_2 are the radii of the nuclei before scission, and those of FP1 and FP2, respectively: $R_0 = r_0 \mathrm{A}^{1/3}$, $R_1 = r_0 \mathrm{A}_1^{1/3}$, $R_2 = r_0 \mathrm{A}_2^{1/3}$ and $r_0 = 1.2$ fm. And Z_1 and Z_2 are atomic numbers (numbers of electric charge) of FP1 and FP2, respectively.

The channel dependent fission barrier E_f is estimated by these potentials and the $Q-$value of the channel, and is defined as

$$E_f = E_c' - Q, \quad (3)$$

where the effective Coulomb potential $E_c^{'}$ = 1.44 Z_1Z_2/R_{eff} in MeV and fm.

It may be more appropriate that R_{eff} is expressed by the next relation.

$$R_{eff} = \eta_1(Z_1, A_1)R_1 + \eta_2(Z_2, A_2)R_2, \quad (4)$$

where $R_1 = r_0 A_1^{1/3}$, $R_2 = r_0 A_2^{1/3}$ and $r_0 = 1.2$ fm.

But we use the next relation for one-parameter analysis.

$$R_{eff} = \eta(R_1 + R_2). \quad (5)$$

The tunnel fission probability $P_i(E_x)$ of i-th channel for the excitation energy E_x is estimated using the Wentzel-Kramers-Brillouin (WKB) method as follows:

$$P_i(E_x) \approx \exp[-0.436\sqrt{\mu}\int_a^b (V(r) - E_x)^{1/2} dr], \quad \text{in MeV and fm,} \quad (6)$$

where μ is the reduced mass: $\mu = A_1A_2/(A_1+A_2)$.

This equation is transformed to the next relation approximately.

$$P_i(E_x) \approx \exp[-0.218\ |a-b|\ \sqrt{\mu\ \Delta V}], \quad \text{in MeV and fm,} \quad (7)$$

where $\Delta V = E_f - E_x$ $(E_x \leq E_f)$.

The yields of FPs are calculated by summing up the tunnel fission probabilities all over fission channels. And the prompt neutron emission from fission fragments that have a characteristic saw tooth shape is considered for the analysis of n+ ^{235}U reaction. Figure 1 (b) shows the prompt neutron emission from the thermal neutron fission of ^{235}U.[10]

The detailed information of the channel dependent fission potential is needed to obtain FP yields for an arbitrary incident neutron energy. The channel dependent fission potentials are difficult to calculate theoretically. The E_f value is able to be adjusted by only one adjustable parameter of the η, by fixing the tunneling distance $|a-b|$ at a certain value, 2.5 fm for this calculation to keep consistency with the previous analysis.[2] FP yields can be calculated using one parameter η for a fission channel to fit with the experimental results[11] of the FP yields for both of thermal and 1 MeV neutron-induced fissions. Therefore, this E_f is only a virtual parameter for this calculation. Hereafter, we use representations of E_f^*, η^* and R_{eff}^* to distinguish the values including tunnel effect from ones not including the effect.

3. ANALYSIS

The plot of η^* used in this analysis has two humps as shown in Fig. 2 (a). The E_f^* for ^{236}U is obtained by the plot of η^*, as shown in Fig. 2 (b).

The FP yield from thermal neutron-induced fission of ^{235}U is shown in Fig. 2 (c). E_x is 6.5 MeV, that is the excitation energy of ^{235}U by thermal neutron absorption. Figure 2 (d) shows FP yield from 1 MeV neutron fission of ^{235}U. E_x is 7.5 MeV. The experimental data for comparison to the analytical results is JENDL-3.2.[11]

And Fig. 2 (d) shows the E_f^* for ^{235}U by using the same plot of η^*. We show FP yield for 14 MeV neutron-induced fission of ^{235}U in Fig. 2 (f) for reference. 14 MeV neutron-induced fission depends on mainly "the chance" fission of ^{235}U* excited by inelastic scattering. E_x is assumed at 10 MeV for this calculation, and the used data of η^* is same for analysis of thermal and 1 MeV fissions in this calculation. But η^* should be calculated for each elements essentially.

In this analysis, the definition of the parameter is different from the one in previous analysis because of one parameter fitting. Figures 2 (g) and (h) show channel-dependent fission barrier E_f and η calculated by previous method.

Figure 3 shows the consistence of SCS analysis for Z-A distribution of FP yield from thermal neutron-induced fission of ^{235}U.

4. DISCUSSION AND CONCLUSION

Thermal and 1 MeV neutron-induced fissions of ^{235}U were analyzed by setting proper effective fission barriers E_f^* containing tunnel effect. Mass-distributions of FP yields for thermal and 1 MeV neutron-induced fissions of ^{235}U were calculated with very good agreements with the experimental data as shown in Figs. 2 (c) and (d), respectively. In particular, Z-A distribution of FP yield from thermal neutron induced fission of ^{235}U is shown in Fig. 3. The present method is suitable for the case that the difference of excitation energies is small. For reference, the mass-distributions of FP yields for 14 MeV neutron-induced fission of ^{235}U were also calculated as shown in Fig. 2 (f).

These analysis are analyzed by setting the proper data set of η^* that characterizes the information of channel-dependent fission potentials. It is difficult to calculate the precise values of channel dependent fission barriers E_f theoretically. To fit the distributions of FP yields with experimental data[11] for each incident neutron energies, the plot of η^* and the plot of E_f^* are obtained for ^{236}U. This E_f^* is not the true channel dependent fission barrier E_f having physical meaning because of including the tunnel effect. Therefore E_f should be converted from E_f^* by excluding the tunnel effect. But we cannot develop the method of reevaluation for E_f by now. Of course, the channel-dependent fission potentials are needed to calculate theoretically for a precise treatment of the tunnel fission effect.

For comparion, we calculate the η and E_f values by the previous method.[2] Figures 2 (g) and (h) show the plot of η and the plot of the E_f value calculated for ^{236}U, respectively. These data have physical meanings but cannot reproduce the incident neutron energy dependence of FP yields. The dispersion of E_f value may be large. The dispersion depends on the restriction of the one-parameter approximation in the equation of R_{eff}, but not on the method estimating E_f value itself. And R^*_{eff} depends on only mass number of the fission fragments approximately for this calculation. The calculation should be carried out by R^*_{eff} containing the effect of atomic number Z in each scission channel.

Three modes of the standard 1 (S1), the standard 2 (S2) and the superlong (SL) are proposed in the multimodal random neck-rupture model[7,8] for the neutron-induced fission of ^{235}U. In SCS analysis, two and three regions exist in the plot of η^* and η as shown in Figs. 2 (a) and (g), respectively. In Fig. 2 (a), the region I corresponds to the SL mode and the region II corresponds to the S1 and S2 modes. In Fig. 2 (g), the region I corresponds to the SL mode, the region II correspond to the S1 and S2 modes and the region III corresponds to the parts of lower FP yields in A<80 and A>160 The SCS analysis is an effective method as shown these correspondences.

These SCS analytical methods considering fission modes will be applied to the experimental data of the nuclear transmutations of W, Au and Pd. However, fission modes of W, Au and Pd are unknown. At present, η is used at a constant value for SCS analysis of W, Au and Pd.

Au is a single isotope in nature. The η is taken as 1.5148. The excited energy E_x is supposed as 15 MeV. Fig.4 (a) is the Z-distribution of FP yield from Au photo-fission calculated by MPIF/SCS model. W has five isotopes in nature, that are ^{180}W (0.120 %), ^{182}W (26.498 %), ^{183}W (14.314 %), ^{184}W (30.642 %) and ^{186}W (28.426 %). The η was taken as 1.55. The excited energy E_x was supposed as 15 MeV. Fig.4 (b) is the Z-distribution of FP yield from natural W photo-fission calculated with weights for natural abundance. Pd has six isotopes in nature, that are ^{102}Pd (1.02 %), ^{104}Pd (11.14 %), ^{105}Pd (22.33 %), ^{106}Pd (27.33 %), ^{108}Pd (26.46 %) and ^{110}Pd (11.72 %). The η was taken as 2.8. The excited energy E_x was supposed as 18 MeV. Figs.4 (c) and (d) are the Mass and Z-distributions of FP yields, respectively, from natural Pd photo-fission.

SCS analysis considering fission modes for these elements is a subject for future study.

REFERENCES

[1] A. Takahashi et al., *Jpn. J. Appl. Phys.*, **40** (2001) 7031; Also see *Proc. ICCF8*, (2000) 397.

[2] M. Ohta et al., *Jpn. J. Appl. Phys.*, **40** (2001) 7047.

[3] N. Bohr and J.A. Wheeler: *Phys. Rev.*, **56** (1939) 426.

[4] L. Meitner and O.R. Frisch: *Nature*, **143** (1939) 239.

[5] D.G. Madland and J.R. Nix: *Nucl. Sci. Eng.*, **81** (1982) 213.

[6] P. Moller et al.: *Nature*, **409** (2001) 785.

[7] U. Brosa et al.: *Phys. Rep.*, **197** (1990) 167.

[8] U. Brosa et al.: *Phys. Rev.*, **C59** (1999) 767.

[9] K. Yagi: *Genshikaku Butsurigaku (Nuclear Physics)* (Asakura, Tokyo, 1989) p. 280 [in Japanese].

[10] *The New Encyclopaedia Britannica* (Encyclopaedia Britannica, Chicago, 1980) 15th ed., Vol. 13, p. 301.

[11] T. Nakagawa et al.: Japanese Evaluated Nuclear Data Library Version-3 Revision-2: JENDL-3.2, *J. Nucl. Sci. and Technol.*, **32(12)** (1995) 1259.

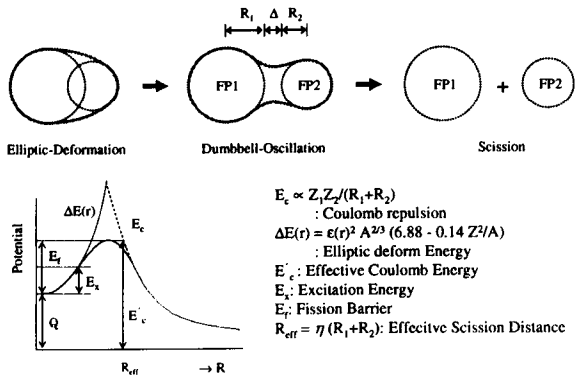

(a) Fission process.

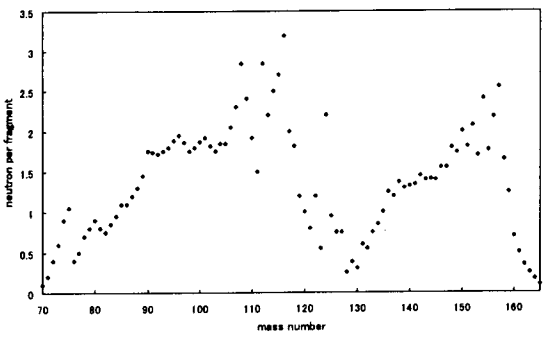

(b) Prompt neutron emission from thermal neutron fission of ^{235}U.

Figure 1: Fission process and prompt neutron emission.

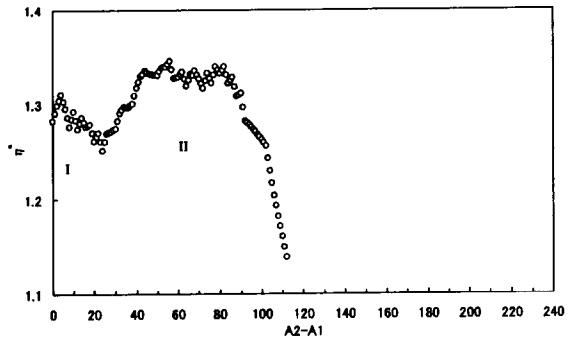

(a) The plot of η^*.

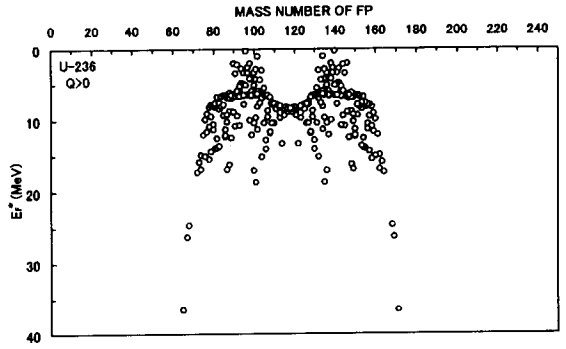

(b) E_f^* for ^{236}U.

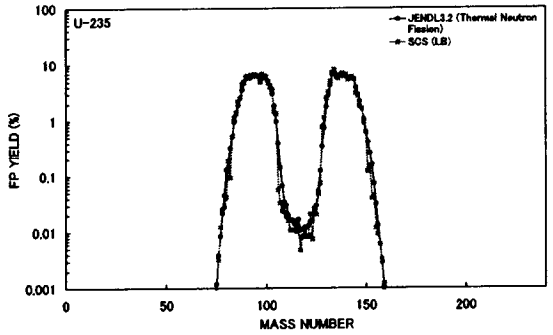

(c) FP yield for thermal.

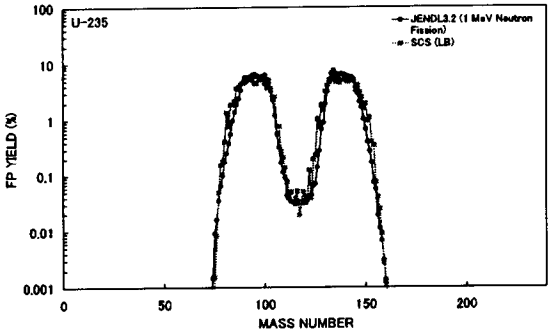

(d) FP yield for 1 MeV.

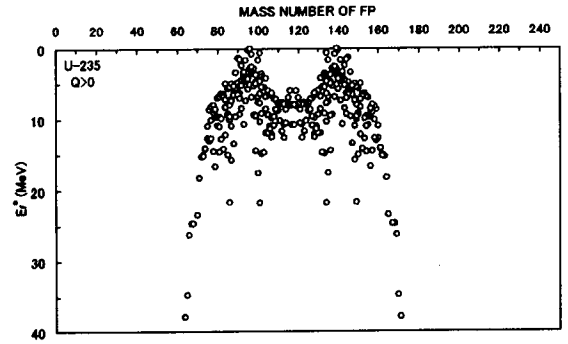

(e) E_f^* for ^{235}U.

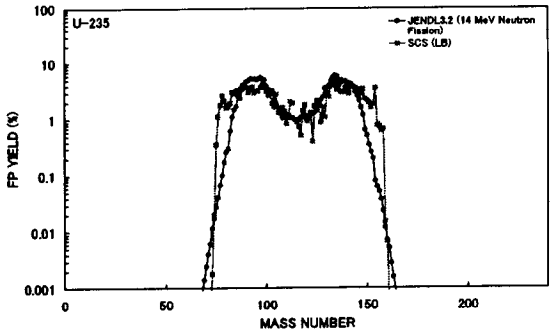

(f) FP yield for 14 MeV.

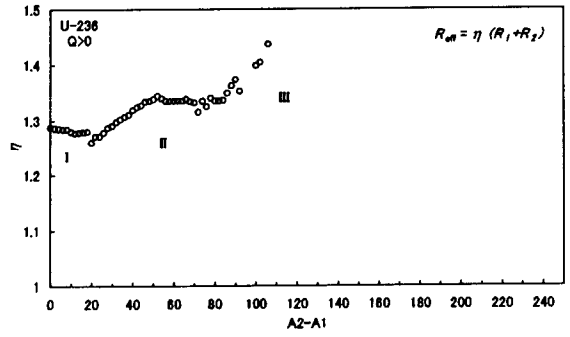

(g) The plot of η.

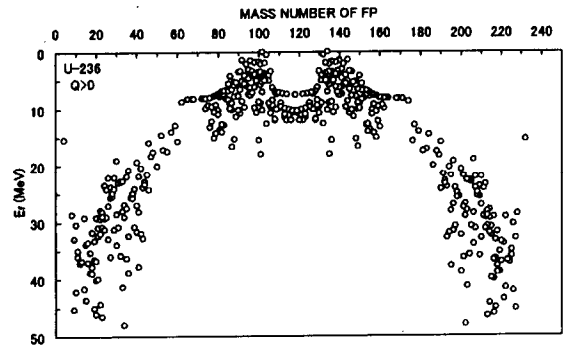

(h) E_f for ^{236}U.

Figure 2: SCS analysis of the neutron-induced fission of ^{235}U.

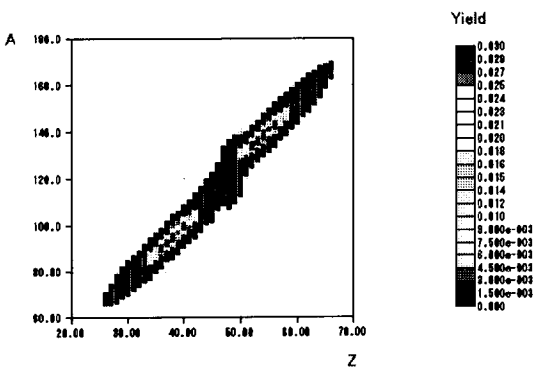

(a) Experimental data (JENDL-3.2).[11]

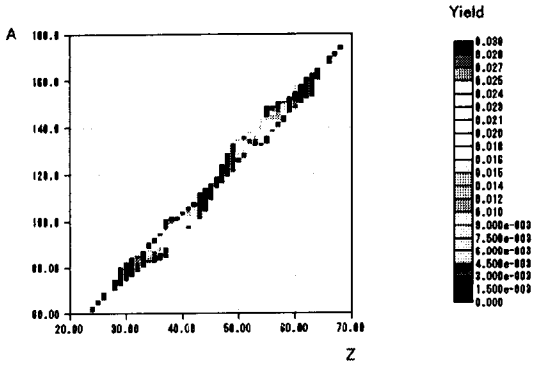

(b) Results by SCS model.

Figure 3: Fission product yields of thermal neutron induced fission of ^{235}U.

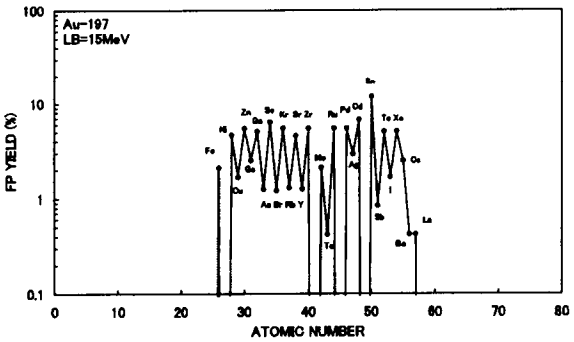

(a) Z-distribution of FP yield for Au.

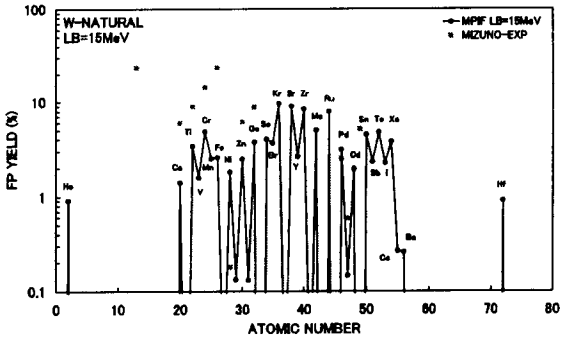

(b) Z-distribution of FP yields for W, compared with experimental data repored by Mizuno et al.

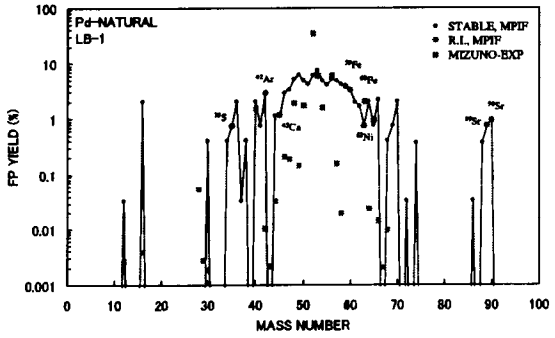

(c) Mass-distribution of FP yields for Pd, compared with experimental data repored by Mizuno et al.

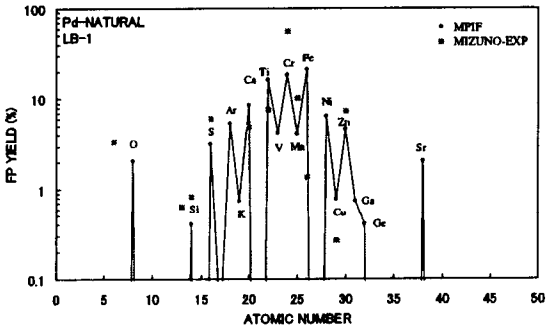

(d) Z-distribution of FP yields for Pd, compared with experimental data repored by Mizuno et al.

Figure 4: MPIF/SCS analysis of Au, W and Pd photo-fission.

POSSIBLE NUCLEAR TRANSMUTATION OF NITROGEN IN ATMOSPHERE OF EARTH

Mikio FUKUHARA, Toshiba Tungaloy: a80010@tungaloy.co.jp

Abstract: An attempt to give a possible answer to a question why nitrogen exists so abundantly in Earth 's atmosphere and how it was formed in Archean era (3.8 to 2.5 billion years ago) is presented. It is ascribed to endothermic nuclear transmutation of carbon and oxygen nuclei confined in carbonate $MgCO_3$ lattice of the mantle with an enhanced rate by attraction effect of catalysis of neutral pions produced by electron emission and nutrinos from sun: $^{12}C + {}^{16}O - 2\pi^0 \rightarrow 2\,{}^{14}N$. The cross section

and the reaction rate are determined: $\sigma = \frac{10^6}{E}\exp\left(\frac{-0.470}{\sqrt{E}}\right)$, $R = 9.254 \times 10^{-6}$ f/s/cc.

Keywords: nuclear transmutation of nitrogen, atmosphere of Earth, carbonate in mantle, neutral pion- catalysis

1. INTRODUCTION

When we examine the composition of the atmosphere of solar planets and their sixty-one satellites, we note that the nitrogen concentration is rather low (~ 6%) on the average with exception of the Earth, Titan and Triton.[1] Earth has extremely high concentration of nitrogen of 78%, in Titan and Triton the concentration would be smaller than 2×10^{-6} % and 5×10^{-6} % of the Earth's one, respectively.[2] Since rocky planets having inner orbitals had formed by accretion of solid planetesimals in the same region of the developing solar system at almost the same time,[3] we cannot imagine that abundance of nitrogen is derived from the planetesimals with abundance of nitrogen as the secondary atmosphere, after primary, captured atmosphere was released.[4] A significant question for the origin of abundance of nitrogen has not been entirely resolved, and has been overlooked without the consensus..

When we investigate carefully the variation of various atmospheric gases on the Earth's history, based on an assumption calculated by many research groups,[5)-9)] we find that the decrease in carbon dioxide composition is accompanied by a gradual accumulation of nitrogen into the atmosphere in Archean era (3.8 to 2.5 billion years ago), before the generation of atmospheric oxygen derived from photosynthetic activity by organic matters from around 2 billion years ago. [10] The disappearance means formation of rocks and mantles containing carbon dioxide due to weathering of igneous rocks. The main parts of carbonaceous rocks are distributed on and near the Earth's surface. Thus, consumption of the carbon dioxide, *i.e.*, formation of carbonates, seems to correlate with formation of nitrogen. Therefore we note a possibility of nuclear transmutation between carbon and oxygen atoms in carbonate crystals to form nitrogen.

In a previous paper, [11] the reason why the Earth's atmosphere has such a high concentration of nitrogen was ascribed to a possible endothermic nuclear transmutation of carbon and oxygen nucleus pairs confined along three $[1\sqrt{3}0]$ directions in a (111) plane of rhombohedral $MgCO_3$ crystals existing in the mantle crust. The nuclear reaction is:

$$^{12}C + {}^{16}O - 2\pi^0 = 2\,{}^{14}N, \qquad (1)$$

based on neutral pion catalyzed fusion, [12]

$$^2D + ^2D + 2\pi^0 = ^4He. \quad (2)$$

Kenny [13] has pointed out that the nucleus is charged by electron capture into neutral pion and then decays to produce heat energy. His electropionic mechanism rests on mass alone and sacrifices both baryon conservation and quark consistent pictures of elementary particles. In case of deuteron with lower mass, we have reported the following formula, [14]

$$e^- + ^2D \rightarrow \pi^o + \nu + \gamma, \quad (3)$$

where ν and γ are neutrino and photon, respectively.

Although main carbonate of mantle is dolomite $CaMgC_2O_6$, we select conveniently magnesite $MgCO_3$ instead of dolomite due to lack of crystal lattice data of dolomite under high pressure over 50 GPa. The excited electron e^* was generated by rapid fracture or sliding of carbonate crystals due to volcanic earthquake, and plenty of neutrinos ν were derived from universe, mainly sun. The neutral pion is provided by emission of two excited electrons derived from the carbonate lattice, [15]

$$e \rightarrow e^*, \gamma. \quad (4)$$

$$\gamma + \gamma = \pi^o \quad (5)$$

Here we consider the nuclear reaction of Eq.(1), using low-energy nuclear interaction based on the electropionic attraction. From Eqs.(5) – (8). we got the following formula

$$^{12}C + ^{16}O + 2e^* + 2\nu \rightarrow 2\,^{14}N + ^4He, \quad (6)$$

with help of the electropionic attraction due to the excited electron capture and neutral pion catalysis. We assumed that the formation of nitrogen and helium had continued for 1.3 billion years in Archean era, until the active volcanism or storm of neutrinos ceases. As far as we know, no previous paper has treated this subject, and the formation rate have not been made clear yet. The possibility needs to be confirmed.

2. REACTION RATE FOR ACTIVATED STATE PRODUCT

Since transmutation of nitrogen is attained by instantly occurring spontaneous fission of activated state product $^{12}C^{16}O$ produced by fusion of carbon and oxygen nuclei, we then consider a reaction rate for the product as the transmutation rate.

In the Born-Oppenheimer approximation, the reaction rate R for the C - O reaction is proportional to the probability $|\Psi(0)|^2$, where Ψ is the wave function of the interacting C - O pair at the origin in the center of mass coordinate system, [16]

$$R = D|\Psi(0)|^2, \quad (7)$$

where D is the nuclear reaction constant (dimensions of cm^3/sec). At very low energies the cross section σ [17] for the reaction can be written as

$$\sigma = \frac{D}{V} C_0^2, \quad (8)$$

where V is the relative velocity of the incident particle and C_0^2 is the s -wave Coulomb penetration factor. When the finite size of the interaction volume is neglected, the Coulomb factor at low energies is

$$C_0^2 \approx 2\pi\eta_0 \exp(-2\pi\eta_0) \quad (9)$$

$$\eta_0 = \frac{e^2}{hV}, \quad (10)$$

where η_0 is the Sommerfeld parameter. Fom Eqs.(8), (9) an (10), we obtain the familiar Gamow formula. [18]

$$\sigma = \frac{S}{E} 2\pi\eta_0 \exp(-2\pi\eta_0) = \frac{S}{E} \exp\left(-\frac{\beta}{\sqrt{E}}\right) \quad (11)$$

$$E = \frac{E_{m_2}}{E_{m_1}+E_{m_2}} \qquad (12)$$

where S is astrophysical S factor and β is the Coulomb barrier tunneling constant, E is a reduced energy of masses, m_1 and m_2 of an incident particle and a target nucleus, respectively. Next we introduce the neutral pions. Pions are responsible for all low-energy nuclear interactions and must be involved in the nuclear interaction.[19] If the neutral pion is provided by emission of two excited electrons, the velocity v of the neutral pion can be assumed as $v = 3\times10^5$ m/s.[12] When two neutral pions collides with carbon and oxygen nuclei, we find that

$$2 \times \tfrac{1}{2} m_{\pi^0} v^2 = \tfrac{1}{2} M' V^2 \qquad (13)$$

$$M' = 14\, m_p + 14\, m_n + 50\, m_{\pi^\pm} + 50\, m_{\pi^0} \qquad (14)$$

where m_p, m_n and $m_{\pi^\pm}$ are masses of proton, neutron and charged pion of the activated state product M', respectively, and V is velocity of M', provided that a mass deviation energy is negligible. In eq.(13), six protons and six neutrons in the carbon ^{12}C nucleus are mediated by eighteen charged pions and eighteen neutral pions, while eight protons and eight neutrons in oxygen ^{16}O nucleus are combined by the attractive mediation of thirty-two charged and thirty-two neutral pions. Thus, we obtain

$$V_{M'} = 2.477 \times 10^4 \text{ m/s.} \qquad (15)$$

To obtain the Coulomb factor C_O^2 in Eq.(8), we must calculate η_O. Using Eq.(15), we get

$$\eta_O = \frac{e^2}{hV_{M'}} = 88.37 \qquad (16)$$

Then we consider the screening effect for the Coulomb repulsion to enhance the fusion probability for carbon-oxygen pairs. As is assumed for compacted matter under high pressure, the total number of oscillating electrons in collective resonance for magnesium is ~ 12. Since the screening by many electrons can be apparently treated as one electron with the total mass of all electrons involved, the effective change of carbon and oxygen is reduced to $e/12$ by the electron charge screening effect. This means

$$\eta = \frac{1}{12}\eta_O \qquad (17)$$

From Eq. (17) we get

$$C_O^2 = 4.627\times10^{-19} \qquad (18)$$

Last we consider D in Eq. (7). Here it should be noted that Jackson [17] has reported that the negative meson should be able to act as a catalyst a very large number of times during it's lifetime and the reaction rate in the mesonic molecule will be of the order of 10^6 times that of the observed rate. For this reason, the meason is quite effective in lowering the Coulomb barrier between two nuclei by virtue of its very small orbit around one of them, as if the mesonic atom acts as a neutron in its penetration up to another nucleus. Hence, by analogy we infer that the rate for C - O reaction can be treated as $D = 2 \times 10^{-8}\cdot cm^3/s$, by catalytic help of neutral pions. Thus we get

$$\sigma = 3.7361 \times 10^{-33} cm^2 = 3.736 \times 10^{-9} \text{ barn} \qquad (19)$$

When we consider a pion exchange force between nucleons, we assume that the S factor is enhanced as a function of the force.[20] We apply the effect by the charged pions to that by the neutral pion. Because the addition of two neutral pions increases the S factor ($=10^6$ keV·barn) by four orders of magnitude over conventional two charged pions, using "multibody fusion resonance" model by model by Takahashi *et al.*[20] Thus Eq.(10) gives

$$E = \frac{10^6}{10^{-9}} \times 4.6271 \times 10^{-19}$$

$= 0.1239$ eV. (20)

This value is plausible one as nuclear fusion with C - O system. Substituting $\sigma = 3.736 \times 10^{-9}$ barn, $S = 10^6$ keV·barn and $E = 12.39 \times 10^{-5}$ keV into Eq.(10) gives Coulomb barrier tunneling constant

$\beta = 0.470$ eV. (21)

Thus we have

$$\sigma = \frac{10^6}{E} \exp\left(\frac{-0.470}{\sqrt{E}}\right). \quad (22)$$

The nuclear reaction rate is given by

$$R = N_{C\text{-}O}\ N_{coh}\ V\sigma, \quad (23)$$

where $N_{C\text{-}O}$ is the atomic density of carbon and oxygen, N_{coh} is a multipliciy factor according to lattice-site conditions. If $N_{C\text{-}O} = 10^{22}$ pair/cm^3, $N_{coh} = 10^{21}$, we get

$R = 9.254 \times 10^{-6}$ f/s/cc (24)

3. CONCLUSION

In a previous paper,[11] the formation of nitrogen existing in the present Earth was interpreted to be the results of endothermic nuclear transmutation due to two body confinement of carbon and oxygen nucleus pairs along three $[1\sqrt{3}0]$ directions in a (111) plane of rhombohedral $MgCO_3$ crystals of upper mantle,

$$^{12}C + {}^{16}O - 2\pi^0 = 2\ {}^{14}N, \quad (1)$$

In this study, we calculated endothermic transmutation rate catalized by neutral pions, provided that the activated state product $^{12}C^{16}O$ immediately undergo fission to two ^{14}N nitrogen atoms, accompanied by liberation of four neutral pions. The cross section and rate for the nuclear reaction are given by

$$\sigma = \frac{10^6}{E} \exp\left(\frac{-0.470}{\sqrt{E}}\right). \quad (22)$$

$R = 9.254 \times 10^{-6}$ f/s/cc (24)

The value of $\sigma = 3.736 \times 10^{-9}$ barn deduced in the present study makes the neutral pion catalyzed fusion plausible.

References:

1) Y.Koide,D.Hirata,H.Yamashita and T.Sato, Database of Planetary Science, Res.Rep.Kanagawa Prefect. Mus.Nat. Hist.,Kanagawa, 1987, 13-29 pp.

2) J.Mitton, The Penguin Dictionary of Astronomy, Penguin Book, London, 1991, Table 6, p.349.

3) J.F.Luhmann,J.B.Pollack and L.Colin, The Pioneer mission to Venus, Sci. Am., April, (1994) 68-75.

4) A.Benlow and A.J.Meadows, The formation of the atmospheres of the terrestrial planets by impact, Astrophys.Space Sci., 46 (1977) 293-300.

5) T.Owen, R.D.Cess and V.Ramanathan, Enhanced CO_2 greenhouse to compensate for reduced solar luminosity on early Earth, Nature, 277, (1979) 640-642.

6) H.Ohmoto, When did the atmosphere enhance oxygen?, Kagaku,14 (1994) 360- 370.

7) J.F.Kasting, Theoretical constraints on oxygen and carbon dioxide concentrations in the Precambrian atmosphere, Precamb.Res.,34, 1987, 205- 229.

8) S.J.Mojzsis,G.Arrhenius,K.D.McKeegan,T.M.Harrison, A.P.Nutman and C.R.L.Friend, Evidence for life on earth before 3,800 million years ago, Nature, 384, (1996) 55-59.

9) M.I.Budyko,A.B.Ronov and A.L.Yanshin, History of the Earth's Atmosphere, Springer-verlag, New York, 1985, p.2, 16, 128.

10) L.Van Valen, The history and stability of atmospheric oxygen, Science, 171 (1971) 439 - 443.

11) M.Fukuhara, Possible Origin of Nitrogen in Earth's Atmosphere, submitting to Earth and Planetary Science Letters.

12) M.Fukuhara, Neutral Pion-Catalysed Fusion in Palladium Lattice, Fus.Sci. and Tech., **43**(2002), 128-133.

13) J.Kenny, Electropionics and Fusion, Fus.Tech., **19**

(1991) 547-551.
14) M.Fukuhara,Possible Dynamic Interaction of Deuterons Between Tetrahedral and Octahedral Interstices of Palladium Lattice at Cryogenic Temperatures,Fus.Tech.,**34**(1998)151-155.
15) R.P.Feymann,The Theory of Fundamental Processes, Benjamin/Cummings Publishing Company, 1961, p.37.
16) C.Van Siclen and S.E.Jones, Piezonuclear Fusion in Isotopic Hydrogen Molecules, J.Phys.,G.12 (1986) 213-221.
17) J.D.Jackson, Catalysis of Nuclear Reactions Between Hydrogen Isotopes by μ^- Mesons, Phys.Rev.,**106** (1957) 330- 339.
18) W.P.Allis, Nuclear Fusion, D.Van Nerstrand Company, Princeton (1960) p.1.
19) D.F.MEASDAY and G.A.MILLER,"Hopes and Realities for the Proton-Pion Reactions," Ann.Rev.Nucl. Part.Phys.,**29**, 121 (1979).
20) N.akahashi,T.Iida,T.Takeuchi and A.Mega, Excess Heat and Nuclear Products by D_2O/Pd Electrolysis and Multi body Fusion, Int. J. Appl. Electromag. Mat.,**3**, (1992) 221-230.
21) A.Takahashi,T.Iida and H.Miyamaru, Multi body Fusion Model to Explain Experimental Results, Fus.Tech.,**27**, (1995) 71-85.

Neutron Drops and Production of the Larger Mass-Number Nuclides in CFP

Hideo KOZIMA[1)]
Physics Department, Portland State University
Portland, OR 97207-0751
1) On leave from Cold Fusion Research Laboratory, Yatsu 597-16, Shizuoka, Shizuoka 421-1202, Japan. E-mail: cf-lab.kozima@nifty.ne.jp

Key words; nuclear excited level, neutron-proton interaction, neutron energy band

Abstract

Formation of the neutron valence bands (NVB) below zero in transition-metal hydrides is verified by quantum mechanical calculation of interaction between lattice nuclei and occluded protons or deuterons. The local coherence of neutron Bloch waves in the NVB results in formation of high-density neutron liquid (NL) and neutron drops (ND) in boundary regions. The NL and ND interact with lattice nuclei, protons (or deuterons) and minor nuclei in boundary regions to produce cold fusion phenomenon (CFP) in which large change of nucleon and proton numbers of nuclei occur with dissipating channels of liberated energy rather than gamma emission

1. Introduction

The nuclear structure of isolated nuclei $^{A}_{Z}X$ has been thoroughly investigated in about sixty years since the discovery of the atomic nucleus in 1911 in order to achieve fundamental understanding in the energy region up to several hundred MeV[1,2)]. The global features of the exited levels of nucleons and their energy distribution seem to be fairly well described by the Fermi gas mode, while the results have had been mainly confined to light nuclei and a quantitative analysis is plagued with difficulties in the description of the reaction mechanism.[1)] This is true even now especially for excited levels with energies very close to the zero level; which corresponds to the neutron level with a binding energy of zero in the nucleus $^{A}_{Z}X$, or to the state where a neutron and the separated nucleus $^{A-1}_{Z}X$ remain still. (We use this energy standard in this paper unless otherwise stated.)

Therefore, it is interesting to investigate some phenomena that are directly related with the excited levels of nucleons at around zero energy in medium and heavy nuclei.

In this paper, these features of excited states of nuclei in solids are semi-quantitatively investigated on the knowledge of nuclear structures established in nuclear physics and apply them to cold fusion phenomenon (CFP). We use the Fermi gas model for nucleons in a nucleus throughout this work.

2. Excited States of Neutrons and its Density of States in Medium and Heavy Nuclei

It is a common knowledge in nuclear physics that average properties of the excitation spectrum are given by the Fermi gas model as a result of dominance of the particle degrees of freedom over the number of collective modes.[1)]

In the Fermi gas model, nucleons in a lattice nucleus at a_i is treated as independent particles and their quantum states $\psi_{\{n\}}(x, a_i)$ are specified by quantum numbers $\{n\} \equiv (n, l, m, s)$;

$$\psi_{\{n\}}(x, a_i) = \psi_{\{nlms\}}(x - a_i, \sigma). \quad (1)$$

The wave function of a neutron in a nucleus $^{A}_{Z}X$, however, extends far away from the nucleus when the energy E of the state is less than but close to zero and then the wave function outsides the nucleus is approximated by

$$\psi_{\{nlms\}}(x - a_i, \sigma) = c_i e^{-\eta|r-a_i|} Y_{l,m}(\theta_i, \phi_i) \chi_s(\sigma), \quad (2)$$

where $\eta \equiv \eta(|E|)$ is a damping factor of the radial wave function depending on the energy assumed for simplicity to be independent of quantum numbers, and (θ_i, ϕ_i) are angles measured from the lattice point a_i. In the following treatment, we use the wave function (1) until we need the wave function (2).

The result of the calculation of the total level density for the Fermi gas in a nucleus $^{A}_{Z}X$ is given as:[1)]

$$\rho(N,Z,\varepsilon) = (6^{1/4} g_0/12(g_0\varepsilon)^{5/4}) \exp((4\pi^2/6) g_0 \varepsilon)^{1/2} \quad (N \quad Z) \quad (3)$$

where ε is the excitation energy measured from the ground state level and g_0 is the one-particle level density at the Fermi energy g_F, representing the sum of the proton and neutron level densities

$$g_0 \equiv g(\varepsilon_F) = (3/2)(A/\varepsilon_F), \quad (4)$$

for a case $Z = N = A/2$. These levels seem very sharp and have fairly long lifetime, which we take as an infinite in the following treatment.

The energy range, where the above formula is applicable, is determined by a relation

$$\varepsilon_F/A \ll E \ll \varepsilon_F A^{1/3}, \quad (5)$$

where ε_F 37 MeV for heavy nuclei.[1] This relation gives an energy range 0.4 – 170 MeV of applicability of the relation (3) for nuclei with mass numbers A 100.

High density of nuclear levels at high excitation energies, amounts of the order 10^6 times higher than that corresponding to single-particle motion, has been revealed by densely spaced, sharp resonances in the slow neutron capture reactions and results in formation of the compound nucleus in a nucleus with A 100.[1,3] The figure 10^6 will be increased further by several orders when the energy of the slow neutron capture reactions goes down to 1 eV. In the following discussion, we will take this factor as 10^9 at its maximum suggested by experimental data for Ag in the range of 2 to 8 MeV[3] considering later application to Pd isotopes in the energy range up to 10 MeV.

3. Effective Potential for the Super-nuclear Interaction between Neutrons in Adjacent Lattice Nuclei of Metal Hydrides and Deuterides

In the transition-metal hydrides MeH_x, on the other hand, the crystal structure is dependent on the concentration x of hydrogen isotopes which can be introduced into the crystal lattice of the metal Me continuously until a definite limit and kept stably there (occluded).[4,5] We confine our investigation to crystals of stoichiometric compounds PdH for our object in the following treatment. In this compound, hydrogen atoms occluded in the crystal are ionized and occupy octahedral interstices having six Pd atoms each as nearest neighbors on the crystallographic axes half way of the lattice constant a. The lattice constant a of the compound PdH_x depends on the composition and that of PdH is a little larger than that of Pd crystal 3.89 Å. In the following treatment, however, we ignore the dependence of a on the composition x and use the value for Pd crystal as for the compound PdH.

Dynamical behavior of the proton occluded in transition-metal hydrides is described as a harmonic oscillator in its ground and lower excited states. The wave function, $\phi_p(R-b_j, \sigma)$, of a proton in a state specified by quantum numbers $p \equiv (n_p, l, m, s_p)$ at an interstice b_j can have finite probability density at nearby lattice point at a_i, a nearest neighbor of b_j, especially when the proton is in its excited states. If we ignore mutual interaction of Z protons on different interstices, the total proton wave function may be expressed as a product of wave functions on the interstices (neglecting anti-symmetrization),

$$\Phi_{\{p\alpha\}}(X_1, X_2, \ldots, Xz,) = \Pi_j \phi\{p_j\}(R_j - b_j, \sigma_j), \quad (6)$$

where $\{p_\alpha\} \equiv \{p_1, p_2, \ldots, p_z\}$.

The overlapping of the proton wave function $\phi\{p_j\}(R_j - b_j)$ on the interstice b_j with a nucleon (neutron) wave function $\psi\{n\}(r - a_i)$, Eq. (1), of an adjacent lattice nucleus at a_i results in the proton-neutron interaction through the nuclear force. The nuclear interaction is expressed by a potential whose form is taken, for example, as the square-well type;

$$V_s(r-R) = -V^{(s)}_0, \quad (|r-R| < b) \quad (7)$$
$$= 0, \quad (|r-R| > b)$$

where $V^{(s)}_0$ 3.5 MeV and b 2.2×10^{-13} cm.[6] The choice of this potential out of several possible types does not make a large difference to the result for low energy phenomena we are considering in this paper.

This interaction pulls two neutron states in different lattice nuclei into coupling as shown below that we will call the "super-nuclear interaction." In the following investigation, we concentrate on excited neutrons in lattice nuclei than protons, which needs more energy to be raised to the excited levels with the same energy than neutrons due to the fact $Z \ll N$. (In Pd, $Z = 46$ and $N = 56 - 64$.)

Let us consider a neutron in an excited state $\{n\}$ of one of lattice nuclei. The regularity of the crystal lattice determines the coefficients of the linear combination as required by the Bloch's theorem.[7] Then in a periodic potential of lattice nuclei, a neutron in an excited state $\{n\}$ of a lattice nucleus at a_i should be expressed by a Bloch function (omitting the spin part)

$$\psi_k(r) = \Sigma_i e^{i(ka_i)} \psi_{\{n\}}(r - a_i). \quad (8)$$

Therefore, the total wave function of the system composed of a neutron Bloch wave $\psi_k(r)$ and z occluded protons in the state $\{p_\alpha\} = \{p_1, p_2, \ldots, p_z,\}$ at interstices is expressed as (omitting spin parts)

$$\Psi_{k,\{p\}}(r; R_1, R_2, \ldots, R_z)$$
$$= \psi_k(r)\ \Phi_{\{p\alpha\}}(X_1, X_2, \ldots, Xz,). \quad (9)$$

The total energy $E_{k,\{p\alpha\}}$ of this system in the second-order perturbation approximation is expressed as follows taking the square well potential for the nuclear interaction:

$$E_{k,\{p\alpha\}} = E_{\{n,p\alpha\}} + \Sigma_{k',i,i',j} \exp(-i(ka_i - k'a_{i'}))v_{np}(ii'j), \quad (10)$$

$$v_{np}(ii'j) = \Sigma_{p'}(\langle np;ij|V|n'p';ij\rangle\langle n'p';i'j|V|np;i'j\rangle)/(E_{\{n',p'\}} - E_{\{n,p\}}),$$
$$= \Sigma_{\{p'\}\neq\{p\}} P \int dE\, \rho \times (\langle np;ij|V|n'p';ij\rangle\langle n'p';i'j|V|np;i'j\rangle)/(E + \varepsilon_{p'p}), \quad (11)$$

$$E_{\{n,p\alpha\}} = E_{\{n\}}^{(p)} + \Sigma_j \varepsilon_{pj}, V(r) = V_s(r), \quad (12)$$

$$\langle np;ij|V|n'p';ij\rangle = \iint dr dR_j\, \psi^*_{\{n\}}(r - a_i)\, \phi^*\{p\}(R_j - b_j)$$

$\times V_s(r-R)\ \psi_{\{n'\}}(r-a_i)\,\phi_p(R_j-b_j)$, (13)

where summations over i and i' in (10) are only over the nearest neighbor lattice points a_i and $a_{i'}$ of an interstice b_j, $\rho_n(E)$ is a density of states for neutron quantum states, $\varepsilon_{p'p} \equiv \varepsilon_{p'} - \varepsilon_p$, and $E \equiv E_{\{n'\}} - E_{\{n\}}$. Further, the summation over $\{p'\}$ reduces to a factor, $(n_p+1)(n_p+2)$, the degeneracy of the energy ε_{np}. $E_{\{n\}}^{(p)}$ is an energy of a neutron in an excited state $\psi_{\{n'\}}(r-a_i)$ in a lattice nucleus at a_i when occluded protons are in states $\{p_\alpha\}$, and ε_{pj} in (12) is an energy of a proton in a state $\phi_{pj}(R_j-b_j)$ at an interstice b_j. We ignore, however, p-dependence of $E_{\{n\}}^{(p)}$ hereafter in this work.

For the neutron wave function (1) in the Fermi gas model, we can describe wave functions $\psi_{\{n'\}}(r-a_i)$ by those determined in the nuclear harmonic oscillator potential in a nucleus to calculate matrix elements (13) in the above equation (11):

$$\psi_{nlms}(r,\theta,\phi,\sigma) = R_{nl}(r)Y_l^m(\theta,\phi)\chi_s(\sigma), \quad (|m| \leq l) \qquad (14)$$

$$E_{nlms} = (n+3/2)(h/2\pi)\omega_n + \Delta\varepsilon_{lms} \qquad (15)$$

where $\Delta\varepsilon_{lms}$ expresses the l s and other coupling energies taken symbolically into consideration to distinguish energies of the states with the same n and different l, m, and s, ω_n is the circular frequency of the harmonic oscillator and $Y_l^m(\theta,\phi)$ are the spherical harmonics.

In nuclei of palladium isotopes, we can use an excited neutron state $2f_{7/2}$ as shown by shell model calculation with a Woods-Saxon potential[1] for the order of magnitude estimation of (14):

$$\psi_{2f\,7/2,s}(r,\theta,\phi,\sigma) = R_{53}(z)Y_3^m(\theta,\phi)\chi_s(\sigma), (|m|\leqq 3) \qquad (16)$$

$$R_{53}(z) = C_n(32/210)^{1/2}z^{3/2}(1-(2/9)z)e^{-z/2}, \qquad (17)$$

$C_n = 2(8\alpha_n^3/\pi)^{1/4}$, $z = 2\alpha_n r^2$, $\alpha_n = \pi m_n\omega_n/h$, where m_n is the mass of the neutron and $\omega_n = 41/A^{1/3}$ MeV.[8]

For the interstitial proton wave functions $\phi_p(R_j-b_j)$ in PdH, on the other hand, we can use a wave function $\phi_{1d}(R,\Theta,\Phi)$ in a lattice harmonic oscillator potential centered at an interstice determined by diffusion data;[9]

$$\phi_p(R_j) = \phi_{nplms}(R,\Theta,\Phi,\sigma_p) = \xi_{npl}(R)Y_{lm}(\Theta,\Phi)\chi_s(\sigma_p), \quad (|m|\leqq l) \qquad (18)$$

$$\varepsilon_{nplm} = 2\pi(n_p+3/2)h\omega_p, \qquad (19)$$

$$\phi_{1d}(R,\Theta,\Phi) = \xi_{1d}(Z)Y_{20}(\Theta,\Phi), (n=2) \qquad (20)$$

$$\xi_{1d}(Z) = C_p(4/15)^{1/2}Z\exp(-Z/2), \qquad (21)$$

$C_p = 2(8\alpha_p^3/\pi)^{1/4}$, $Z = 2\alpha_p R^2$, $\alpha_p = \{m_p\pi\omega_p/h\}$, $\omega_p = (K/m_p)^{1/2}$,

or by Hermite polynomials $H_n(\xi)$;[10]

$$\phi_p(R_j-b_j,\sigma_p) = u_{nx}(x)\,u_{ny}(y)\,u_{nz}(z)\ \chi_s(\sigma_p), \qquad (22)$$

$$u_{nx}(x) = N_nH_n(\alpha x)\exp(-(1/2)\alpha^2x^2), \qquad (23)$$

$\alpha^4 = 4\pi^2m_pK/h^2$, $N_n = (\alpha/\pi^{1/2}2^n n!))^{1/2}$.

where $R = (R,\Theta,\Phi)$, n_p is an integer, $l \leqq n_p$ and $|m| \leqq l$, ε_{nlm} is the proton energy of the state $\phi_{nlm}(R)$, $\omega_p = (K/m_p)^{1/2}$, m_p is the mass of the proton, K is the force constant, and $n_i (i = x, y, z)$ are integers.

The proton wave functions thus determined include already effects of screening by itinerant electrons and electrons bound in atoms, and also the effect of Coulomb repulsion by lattice nuclei.

The analysis based on the diffusion data[9] showed that appropriate wave functions for a proton in the NbH is that with n = 2 in the above equation and the corresponding force constant K is given as

$$K_H = 1.44 \times 10^{19}\ \text{eV/m}^2 \quad \text{(NbH)} \qquad (24)$$

We use this value for PdH to make an order of magnitude estimation in this paper.

A concrete expression of the matrix element (14) for PdH is expressed as follows using wave functions (15), (19), and others:

$$\langle 2f_{\{7/2\}}1d;ij|V|2p_{\{3/2\}}2s;ij\rangle = -\iint dr dR_j R_{53}(z_i)Y_{3,0}(\theta_i,\phi_i)\chi_{1d}(Z_j)Y_{2,0}(\Theta_j,\Phi_j) \times V_s(r-R_j)R_{51}(z_i)Y_{1,0}(\theta_i,\phi_i)\chi_{2s}(Z_j)\ Y_{0,0}(\Theta_j,\Phi_j), \qquad (25)$$

$z_i = 2\alpha_n|r-a_i|^2$, $Z_j = 2\alpha_p|R_j-b_j|^2$,

where a_i is a nearest neighbor lattice site of an interstice b_j, $K = K_H$ in α_p in Eq.(22), and (θ_i,ϕ_i) and (Θ_j,Φ_j) are angles measured from origins at a_i and b_j, respectively.

To estimate an order of magnitude of the effective potential $v_{np}(ii'j)$ (11), we utilize the property of the densely spaced excited states explained before and ignore selection rules associated with single configurations. Furthermore, we put the numerator of (11) as a constant and take it as the value of the matrix element (25) for PdH.

Then, the order of magnitude of the effective potential $v_{np}(ii'j)$ given in Eq.(11) is estimated as follows: the proton wave function $\phi_p(R)$ is slowly varying in the range of the nuclear force, and the nuclear wave function $\psi_n(r)$ is approximated by a delta-function. Then, an order of magnitude of the matrix elements $\langle np;ij|V|n'p';ij\rangle$ is given as

$$|\langle np;ij|V|n'p';ij\rangle| \int \psi_n(r)^*\ \psi_n(r)dr\langle V\rangle\phi_p(R)^*\phi_p(R)\Omega \qquad (26)$$

$$1\times\{4/3\}\pi r_0^3\times|u_2(x_N)|^2|u_0(0)|^2|u_0(0)|^2 = 3.2\times10^{-14}\ \text{eV}, \qquad (27)$$

where Ω is the volume of the Pd nucleus, $\langle V\rangle = |V_0^{(s)}| = 3.5$ MeV (Eq.(7)), $\phi_p(R)$ is taken as $u_2(x)u_0(y)u_0(z)$ and $x_N = 1.95$ Å is the position of the lattice nucleus measured from the interstice.

Putting this value (30) into Eq.(11), we can estimate the effective potential $v_{np}(ii'j)$ as a function of the principal value of the integration appeared in that equation, assuming the insensitiveness of the matrix elements to the energy:

$v_{np}(ii'j) \quad 1\times10^{-27}\ \text{eV}^2I$,

$I \equiv P \int (\rho_n(E)/E)dE.$ (28)

We can estimate the approximate value of the integral I, taking following values $\rho_n(E)$ 10^9 keV^{-1}, $\delta\varepsilon$ 10^{-9} keV, and $\Delta\varepsilon$ 1 keV on the assumption that single particle energy level difference is 1 keV and the level density increases to 10^9 times larger than that of single particle motion:

I $(\rho_n(\varepsilon)/\delta\varepsilon)\,\Delta\varepsilon = 10^{15}$ eV^{-1}.

v_{np}(ii'j) 1×10^{-12} (eV). (29)

4. Tight-Binding Neutron Bands in Metal Hydrides and Deuterides

The effective super-nuclear interaction energy obtained above is used to calculate band structure of neutron energy in transition-metal hydrides that is originated in the excited states of neutrons in lattice nuclei and mediated by occluded hydrogen isotopes.

To show briefly crystal-structure dependence of the bandwidth, we will make a simplification of the super-nuclear interaction (11) between adjacent nuclei at a_i and $a_{i'}$ assuming that it depends only on the magnitude of the vector $a_l \equiv a_i - a_{i'}$.

Then, we can rewrite the total energy (10) and have energy spectrum of the neutron Bloch waves in the face centered cubic (fcc) lattice (a is the side of the lattice cube);[7]

$$E = E_{\{n,p\alpha\}} - \alpha - 2\times4\gamma(\cos(1/4)k_ya\cos(1/4)k_za + \cos(1/4)k_za\cos(1/4)k_xa + \cos(1/4)k_xa\cos(1/4)k_ya) - 2\gamma(\cos k_xa + \cos k_ya + \cos k_za) \quad \text{(fcc)} \quad (30)$$

$$E_{\{n,p\alpha\}} = E_{\{n\}} + \Sigma_j \varepsilon_{pj},$$

$$-\alpha = v_{np}(0), \quad -\gamma = v_{np}(ii'j), \quad (31)$$

The factor 2 in the third term on the right comes from the fact that nearest neighbor lattice nuclei are mediated by two protons at different interstices while next nearest ones are by only one. A characteristic of this energy band formation is the contributions from nearest neighbors ((0, $\pm$a/2, $\pm$a/2) etc.) and also from next nearest neighbors (($\pm$a,0,0) etc.) to the k-dependent terms.

The neutron energy bands originating in the excited states of lattice nuclei are located below zero energy in contrast to those originating in free neutron states above zero worked out in a previous paper.[11] The former could be called *neutron valence band* and the latter *neutron conduction band* to distinguish them in the following discussion of the nuclear reactions in solids.

Using the value of v_{np}(ii'j) given in (29), we obtain a semi-quantitative estimation of the valence band width Δ from Eq.(30):

$\Delta = 24\, v_{np}$(ii'j) 10^{-8} (meV) (PdH). (32)

Thus, it is concluded that the matrix elements (25) should be 10^5 times larger than the values estimated in (27) to substantially keep the neutron bands below zero which was determined to form in solids with a width Δ 25 meV that is not destroyed by the thermal motion of ions at room temperature. This is realized only when the neutron wave function (1) extends out as the wave function (2) from a lattice nucleus to regions where a wave function of the occluded proton (23) has a larger value by a factor 10^5 than that at the lattice nuclei. The main term of the proton wave function relevant to this behavior is the exponential factor $\exp\{-\alpha^2x^2/2\}$ in (23) and it gives this value at x_0 = 1.43 Å from an interstice (or 0.52 Å from a lattice point). If this behavior is coupled with an extension of the neutron wave function (2), then the neutron-proton interaction can contribute to formation of a neutron valence band with a width of Δ 25 meV.

From a point of view of the isolated nucleus treated in conventional nuclear physics, this is an unconceivable situation. While, the extension of a neutron wave function (2) far away to 0.52 Å = 5.2$\times$ 10^{-9} cm over the nuclear extent range of $r_0 = 10^{-13}$ cm, i.e. 10^4 times longer than r_0, is not absurd in the situation we are considering here.

As was shown by numerical calculation in a previous paper,[11] the energy of thermal neutrons interacting with lattice nuclei by attractive nuclear force is pulled down below zero; the states of propagating waves then become quasi-localized states around lattice nuclei with a damping factor depending on the strength of the attractive interaction. The same situation is also realized from opposite direction as a limit of highest bound states as shown in Eq.(2). We consider here an s-type wave function for the state, for simplicity:

$$\psi_\eta(r - a_i) = c_i \exp(-i\eta|r - a_i|). \quad (33)$$

To extend the neutron wave function to the range of $\lambda = 5.2\times10^{-9}$ cm referred above, the decay constant of the state $\eta(|E|) = 1/\lambda$ should be 1.9×10^8 cm^{-1} and this corresponds to an energy E:

$|E| = (h^2/8\pi^2m_n)\,\eta(|E|)^2 = 7.4$ (eV) (34)

below zero, where $m_n = 1.67\times10^{-24}$ g is the neutron mass. In other words, the excited states of isolated lattice nuclei with energies of from zero to 7 eV can participate to the *neutron valence band*, or the neutron bands below zero, in transition-metal hydrides considered above.

If the state has less energy, i.e. far from zero, and the extension of the state is less than 5.2×10^{-9} cm, the band state fails to be substantially formed even in PdH and neutrons are essentially in single particle states in isolated lattice nuclei.

5. Discussion

When there are many neutrons in a neutron band,

there appear interesting features of neutron's behavior at boundaries that reflect neutrons back into the crystal; "local coherence" of neutron Bloch waves, and therefore, high densities of neutrons (neutron liquid) appear there.[12] High-density neutrons in the boundary region[13] or in neutron star matters [14,15] induce formation of "neutron drops" (or clusters of many neutrons and a few protons and corresponding electrons) in a thin neutron background. These neutron liquid (NL) and neutron drops (ND) in a thin neutron background interact with nuclei to produce new nuclear effects in the boundary region.

Scenario of the CFP will be written down as follows. The background thermal neutrons in ambience trapped in a sample of the transition-metal hydrides or deuterides are in a neutron conduction band. Their density at boundary region becomes high due to the local coherence but may be not so large and not enough to form neutron drops. The neutrons in the band, however, can reacts with nuclei in the boundary region and the reactions are the trigger reactions.[16,17] The nuclear products of the trigger reactions induce breeding reactions resulting in multiplication of the number of neutrons in the conduction band and also excitation of neutrons in lattice nuclei.

The latter effect makes possible formation of neutron valence bands (NVB) in the CF matter we are now considering. The density of neutrons in the NVB will be very large enough to form neutron liquid (NL) and neutron drops (ND) in the boundary region. The ND thus formed may be in a lattice (a Coulomb lattice) with smaller lattice constants coexisting with original crystal lattice of the transition metal with larger (10^2 times) lattice constants. This is a new state of solids not noticed and not observed until CFP was detected.

The NL and/or ND thus formed can give or exchange nucleons with lattice nuclei and/or with nuclei of minor elements in the boundary layer. Nuclear reactions investigated in nuclear physics in 20th century were mainly those occur in free space except rare cases of n-p cluster formations in the neutron star matter.[14,15] The nuclear reactions in surface layers where are lattice nuclei, occluded hydrogen isotopes, and high density neutrons (NL and ND) should be distinguished from those occurring in free space and treated with similar cautions to the n-p cluster formation in the neutron star matter.[15]

The fundamental differences related with nuclear transmutations observed in CFP are possibilities of 1) nucleon exchange between NL (and/or ND) and lattice nuclei (and/or minor nuclei) and 2) energy exchange between NL (and/or ND) and nuclides in excited states in the CF matter. The former gives a possibility to generate new nuclides with largely different mass and proton numbers from lattice or minor nuclei in the CF matter and the latter gives a possibility to stabilize excited states of nuclides without emission of γ-rays.

In our treatment of experimental data sets in CFP,[11,12,16–18] we have applied the TNCF model to various events only using reactions where occurs absorption of a neutron by a nucleus followed by β- or α- decay or by fission to explain various products with successful results. The nuclear transmutations, however, have shown large changes of mass numbers up to several tens in the experiments showing NT_F[19–23] and recent experiment of NT_A[23–27] which needs possibility to absorb large number of neutrons or sometimes the n-p clusters simultaneously. The formation of NL and/or the neutron drops (ND) gives natural explanation of these absorptions.

As we have seen in this paper, CFP is a wide spread phenomenon including excess heat generation, three types of NT, production of light elements, ^{3}H and ^{4}He, emissions of neutrons, gammas and X-rays with various energies up to about 10 MeV, and decay-time shortenings[16,28-30] occurring in complex systems composed of transition-metal hydrides and deuterides and others at about room temperature in ambient radiation.

The events with large variety from nuclear transmutations to emissions of light particles and γ-rays are evidences of nuclear reactions occurring in surface layers of CF materials, especially transition-metal hydrides and deuterides, intermittently and sporadically. Investigating this phenomenon, we could figure out physics of CFP as neutron physics in crystals occluding hydrogen isotopes; formation of two types of neutron bands, neutron liquid and neutron drops in surface layers where appears the local coherence of neutron Bloch waves.

Knowing physics of CFP, we can explore various applications of this phenomenon ranging from production of new nuclides, remediation of hazardous radioactivity, and production of thermal energy although limited by our poor imagination at present. Really, world of application of this phenomenon will be wider exceeding our present imagination.

Acknowledgment

The author would like to express his thanks to John Dash, Makoto Takeo and Jon Warner for valuable discussions during this work. This work is supported by a grant from the New York Community Trust and Professional Development Fund for Part-time Faculty of Portland State University.

References

[1] A. Bohr and B.R. Mottelson, *Nuclear Structure* I, Benjamin, New York, 1969.

[2] A. Bohr and B.R. Mottelson, *Nuclear Structure* II, Benjamin, New York, 1975.
[3] K. Tsukada, S. Tanaka, M. Maruyama and Y. Tomita, "Energy Dependence of the Nuclear Level Density below the Neutron Binding Energy" *Nuclear Physics*, **78**, 369 (1966).
[4] R. Bau ed., *Transition Metal Hydrides*, American Chemical Society, Washington, D.C., 1978.
[5] G. Alefeld and J. Voelkl ed. *Hydrogen in Metals* I, Springer-Verlag, Berlin, 1978.
[6] J.M. Blatt and V.F. Weisskopf, *Theoretical Nuclear Physics*, Chapter II, John-Wiley & Sons, New York, 1952.
[7] For instance, N.F. Mott and H. Jones, *The Theory of the Properties of Metals and Alloys*, Dover, New York, 1958.
[8] W.F. Hornyak, *Nuclear Structure*, Chapter IV, Academic Press, New York, 1975.
[9] J.A. Sussmann and Y. Weissman, "Application of the Quantum Theory of Diffusion to H and D in Niobium" *Phys. Stat. Sol.* **B53**, 419 (1972).
[10] For instance, L. Pauling and E.B. Wilson, *Introduction to Quantum Mechanics*, McGraw-Hill Book Co., New York, 1935.
[11] H. Kozima, "Neutron Band in Solids", *J. Phys. Soc. Japan* **67**, 3310 (1998).
[12] H. Kozima, K. Arai, M. Fujii, H. Kudoh, K. Yoshimoto and K. Kaki, "Nuclear Reactions in Surface Layers of Deuterium-Loaded Solids" *Fusion Technol.* **36**, 337 (1999).
[13] H. Kozima, "Neutron Drop: Condensation of Neutrons in Metal Hydrides and Deuterides", *Fusion Technol.* **37**, 253 (2000).
[14] G. Baym, H.A. Bethe and C.J. Pethick, "Neutron Star Matter," *Nuclear Physics* **A175**, 225 (1971).
[15] J.W. Negele and D. Vautherin, "Neutron Star Matter at Sub-nuclear Densities" *Nuclear Physics* **A207**, 298 (1973)
[16] H. Kozima, *Discovery of the Cold Fusion Phenomenon - Evolution of the, Solid State-Nuclear Physics and the Energy Crisis in 21st Century*, Ohtake Shuppan KK., Tokyo, Japan, 1998.
[17] H. Kozima, K. Kaki and M. Ohta, "Anomalous Phenomenon in Solids Described by the TNCF Model", *Fusion Technol.* **33**, 52 (1998).
[18] H. Kozima, M. Ohta, M. Fujii, K. Arai and H. Kudoh, "Possible Explanation of ^{4}He Production in a Pd/D_2 System by the TNCF Model" *Fusion Science and Technology* **40**, 86 (2001).
[19] J.O'M. Bockris and Z. Minevski, "Two Zones of "Impurities" Observed after Prolonged Electrolysis of Deuterium on Palladium", *Infinite Energy* Nos. 5 & 6, 67 (1995-96). (NT_F)
[20] T. Mizuno, T. Akimoto, T. Ohmori and M. Enyo, "Confirmation of the Changes of Isotopic Distribution for the Elements on Palladium Cathode after Strong Electrolysis in D_2O Solution", *Int. J. Soc. of Materials Engin. for Resources* **6-1**, 45 (1998). (NT_F)
[21] T. Ohmori, M. Enyo, T. Mizuno, Y. Nodasaka and H. Minagawa, "Transmutation in the Electrolysis of Light Water - Excess Energy and Iron Production in a Gold Electrode", *Fusion Technol.* **31**, 210 (1997). (NT_F)
[22] G.H. Miley, G. Narne, M.J. Williams, J.A. Patterson, J. Nix, D. Cravens and H. Hora, "Quantitative Observation of Transmutation Products Occurring in Thin-Film Coated Microspheres during Electrolysis", Proc. ICCF6, p.629. (NT_F)
[23] H. Yamada, S. Narita, Y. Fujii, T. Sato, S. Sasaki and T. Omori, "Production of Ba and Several Anomalous Elements in Pd under Light Water Electrolysis" *Proc. ICCF9* (to be published); Abstracts of ICCF9, p.123 (2002). (NT_F and NT_A; Pd → Ba, Pb)
[24] S. Miguet and J. Dash, "Microanalysis of Palladium after Electrolysis in Heavy Water", *Proceedings of 1st Low Energy Nuclear Reactions Conference*, College Station, Texas, p. 23 (1995) (NT_A; Pd → Cd).
[25) R. Kopecek and J. Dash, "Excess Heat and Unexpected Elements from Electrolysis of Heavy Water with Titanium Cathodes", *Proceedings of 2nd Low Energy Nuclear Reactions Conference*, College Station, Texas, p. 46 (1996) (NT_A; Ti → Cr).
[26] J. Warner and J. Dash, "Heat Production during the Electrolysis of D_2O with Titanium Cathodes", *Conference Proceedings* **70** (*Proceedings of 8th International Conference on Cold Fusion*, Lerici, Italy), p.161 (2000) (NT_A; Ti → Cr).
[27] Y. Iwamura, M. Sakano and T. Itoh, "Elemental analysis of Pd Complexes: Effects of D_2 Gas Permeation" *Jpn. J. Appl. Phys.* **41**, 4642 (2002) (NT_A; Cs → Pr, Sr → Mo)
[28] J. Dash, I. Savvatimova, S. Frantz, E. Weis and H. Kozima, "Effects of Glow Discharge with Hydrogen Isotope Plasmas on Radioactivity of Uranium", *Proc. ICCF9* (2002) (to be published). (Decay-time shortening of $^{238}_{92}$U)
[29] I.V. Goryachev, "Abnormal Results of Experimenting with Excited Substances and Interpretation of the Discovered Effects within the Frames of the Model of Collective Interactions", *Proc. ICCF9* (2002) (to be published). (Decay-time shortening of radioactive nuclides)
[30] J. Dash, I. Savvatimova, G. Goddard, S. Frantz, E. Weis and H. Kozima, "Effects of Hydrogen Isotope on Radioactivity of Uranium" *Proc. ICENES2002* (to be published). (Decay-time shortening of $^{238}_{92}$U)

DRASTIC ENHANCEMENT OF DEUTERON-CLUSTER FUSION BY TRANSIENT ELECTRONIC QUASI-PARTICLE SCREENING

Akito TAKAHASHI, Osaka University: akito@nucl.eng.osaka-u.ac.jp

Abstract: Superconductivity trend of metal-deuteride like PdDx suggests the generation of transient electronic quasi-particles e* like Cooper pair with short life in dynamic lattice plasma oscillation of deuterons with electrons squeezing to focal points. Under the transient generation of e*, drastic screening effect on d-d Coulomb repulsive potential was estimated to induce observable level D+D fusion rates and further more deep potential hole attracting D-cluster of 4-8 deuterons with electrons which could realize very enhanced 4D and 8D cluster fusion rates. Elemental analyses for screening effect by e* is described.

Keywords: PdDx, electronic quasi-particle, drastic screening, deuteron cluster-fusion

1. INTRODUCTION

We have studied the transient deuteron-cluster formation in full or over-loaded metal deuteride (MDx) systems like PdDx (x>1) and elaborated the theoretical model of tetrahedral (TRF) and octahedral resonance fusion (ORF) by assuming the transient "bosonization" of electrons, namely the generation of electronic quasi-particles like Cooper pair and quadru-coupling[1,2]. We concluded that the reversion of fusion-rate-levels between D+D (2D) fusion and multibody (3D, 4D and 8D) fusions could take place in the competing process of 2D through 8D fusion in TRF and ORF deuteron-clusters (D-cluster), which nuclear products agreed quite well with claimed ^{4}He generation with excess heat and mass-8-and-charge-4 increased transmutation[2]. This paper makes further detail study on screening effect by electronic quasi-particle generation.

2. GENERATION OF ELECTRONIC QUASI-PARTCLES

Some of metal-deuterides have been studied for high temperature superconductivity trend, as typical significant effect was reported by Celani et al.[3] for full and over-loaded PdDx (x = or > 1). The physics of low-temperature superconductivity is believed to be established by the BCS theory[4] and the physics of high-Tc (critical temperature) superconductivity has been studied, albeit not established yet, by extension of the BCS theory and Bogoliubov theory for electronic quasi-particle generation.

Deuteron at O-site (or T-site) in PdDx lattice behaves as an harmonic oscillator with phonon frequency ω_q. And motion of electrons is treated with plasma oscillation with frequency ω of the lattice system with many electrons, deuterons and metal-atoms (e.g., Pd). By electron-phonon scattering, momentum $\mathbf{q} = \mathbf{k} - \mathbf{k}'$ is carried by phonon and two electrons having opposite momentum and spin may be born to generate a Cooper pair $(\mathbf{k}\downarrow, -\mathbf{k}\uparrow)$ as an electronic quasi-particle, due to attractive force to compensate repulsive force of Coulomb interaction, in the phonon-electron coupled motion. Shielded Coulomb interaction potential is given[4] as:

$$V(q,\omega) = 4\pi e^2/(q^2 + k_s^2) + (4\pi e^2/(q^2 + k_s^2))(\omega_q^2/(\omega^2 - \omega_q^2)) \quad (1)$$

$$= (4\pi e^2/(q^2 + k_s^2))(\omega^2/(\omega^2 - \omega_q^2)) \quad (2)$$

where $1/k_s$ is the screening distance for Fermi gas. The 1st term of Eq.(1) shows normal Coulomb repulsive potential between electrons, and the 2nd term shows phonon-mediated interaction. As clearly seen by Eq(2), the potential becomes negative (attractive) if $\omega < \omega_q$. This is a driving force to produce Cooper pairs. When two deuterons with electrons are squeezing from opposite directions to T-site (or O-site) under the TRF (or ORF) transient condensation[2], the condition of opposite momentum and spin for two electrons can be naturally fulfilled. However, directions of deuterons in TRF and ORF condensation are not ideally 180 degree opposite, so that momentum transfer by phonon-electron coupling makes conditioning for transient Cooper pairs.

Effective mass m* and effective charge e* of Cooper pair can be approximately given[4] as $m^* = 2m_e$ and $e^* = 2e$. Microscopic Cooper pair with short life around lattice focal point can be regarded as single particle with mass $2m_e$ and charge 2e. Hence we label Cooper pair as $e^*(m^*/m_e, e^*/e) = e^*(2,2)$. Cooper pair is the s-wave pairing of two electrons with opposite momentum and spin. To explain high-Tc superconductivity, generation of unconventional

pairing (e.g., d-wave pairing) and very heavy fermions (several hundred times mass of electron) have been proposed (see Chapter 9 of Ref-4), albeit reaching no consensus yet. By considering higher order pairing (s-wave) of binary e*(2,2) quasi-particles to generate a quadru-coupling e*(4,4) and moreover e*(8,8) by binary e*(4,4) quasi-particles, we may treat the state of high-Tc superconductivity, instead of assuming heavy fermions (electrons), as we see later.

"Bosonized" electron wave function Ψ_N for N-electrons system in MDx lattice will be approximated by a linear combination of normal electron wave function $\Psi_{(1,1)G}$ and quasi-particle wave functions $\Psi_{(2,2)G}$, $\Psi_{(4,4)G}$ and $\Psi_{(8,8)G}$ as;

$$|\Psi_N\rangle = a_1|\Psi_{(1,1)G}\rangle + a_2|\Psi_{(2,2)G}\rangle + a_4|\Psi_{(4,4)G}\rangle + a_8|\Psi_{(8,8)G}\rangle \quad (3)$$

This may be called quasi-particle expansion of total electronic wave function. Here suffix G denotes ground state. For MDx system, the normal electron wave function $|\Psi_{(1,1)G}\rangle$ coupled with phonon may be given by a Bloch function with lattice period xl, combined with harmonic oscillator motion for D, in one-dimensional case; Using Hermite polynomial H_n,

$$|\Psi_{(1,1)G}\rangle = \sum C\exp(il(x\text{-}xl)) \sum \exp(-\alpha_n(x\text{-}xl)^2) H_n^2(\alpha_n^{1/2}(x\text{-}xl)) \quad (4)$$

The ground state BCS wave function is defined as,

$$a_1|\Psi_{(1,1)G}\rangle + a_2|\Psi_{(2,2)G}\rangle = \Pi(u_k + \nu_k C^*_{k\uparrow} C_{-k\downarrow})|\Psi_0\rangle \quad (5)$$

where $|\Psi_0\rangle$ denotes vacuum, u_k is the un-occupied wave function of Cooper pair and ν_k is the occupied wave function of Cooper pair; hence $u_k^2 + \nu_k^2 = 1$ is the normalization condition. $C^*_{k\uparrow}$ and $C_{-k\downarrow}$ are generation and destruction operators, respectively.

We may define production operator C^*_{2k} and destruction operator C_{2k} for bosonized (spin zero) e*(2,2) to generate quadru-coupling e*(4,4) as,

$$a_1|\Psi_{(1,1)G}\rangle + a_2|\Psi_{(2,2)G}\rangle + a_4|\Psi_{(4,4)G}\rangle = \Pi(u_{2k} + \nu_{2k} C^*_{2k} C_{2k})|\Psi_0\rangle \quad (6)$$

with $u_{2k}^2 + \nu_{2k}^2 = 1$ for normalization. Wave function for e*(8,8) is similarly defined.

To evaluate coefficients a_1, a_2, a_4 and a_8, we may apply the variational method with evaluating the BCS Hamiltonian (see Chapter 3 of Ref-4);

$$H = \sum\sum \varepsilon_{kn} k_\sigma + \sum\sum V_{kl} C^*_{k\uparrow} C^*_{-k\downarrow} C_{-l\downarrow} C_{l\uparrow} \quad (7)$$

And

$$\delta\langle\Psi_N^*|H|\Psi_N\rangle = 0 \quad (8)$$

The above equations are just for formality, and we need further extension to substantiate the problem. However, essential components of the problem can be analyzed as shown in the next section.

3. SCREENING EFFECT AND FUSION RATES

For the time-window of potential deep hole[1,2], effective (time-averaged) screening potential, for a d-d pair in a transient D-cluster of 4-8 deuterons for TRF and ORF condition[2], can be defined by a screened potential of quasi-particle complex;

$$V_s(R) = b_1 V_{s(1,1)}(R) + b_2 V_{s(2,2)}(R) + b_4 V_{s(4,4)}(R) + b_8 V_{s(8,8)}(R) \quad (9)$$

Where R is the inter-nuclear distance of a d-d pair and $V_s(m^*/m_e, e^*/e)(R)$ is the screened potential for a dde*$(m^*/m_e, e^*/e)$ molecule, for $(m^*/m_e, e^*/e)$ = (1,1), (2,2), (4,4) and (8,8). Time-averaging treatment for transient D-cluster condensation with electrons including transient quasi-particles is transferred here to coefficients b_1 through b_8. By definition, we need to satisfy the following normalization condition.

$$b_1^2 + b_2^2 + b_4^2 + b_8^2 = 1 \quad (10)$$

For a dde* molecule (one quasi-particle approximation) within the short time-interval of D-clustering, wave function of a d-d pair (2D) is given by the solution of the following Schroedinger equation:

$$(-h^2/(8\pi\mu))\nabla^2 X(R) + (V_n(R) + V_s(R))X(R) = EX(R) \quad (11)$$

with nuclear potential $V_n(R)$ for strong interaction and reduced deuteron mass μ.
By Born-Oppenheimer approximation, we assume as,

$$X(R) = X_n(R) X_s(R) \quad (12)$$

Overlapping rate of $X(R)$ at $R = r0$ gives estimation of d-d fusion rate λ_{2d} as:

$$\lambda_{2d} = G|X(R)|^2_{R=0} = G|X_n(R)|^2_{R=0}|X_s(R)|^2_{R=0} \quad (13)$$

where G is the scaling constant and r0 is given to be 5 fm considering deuteron radius plus charged-pion exchange range (about 2 fm) at contact surface

configuration of the moment of d-d fusion reaction.
Using WKB approximation for the barrier ($V_s(R)$) penetration probability,

$$| X_s(R) |^2_{R=r0} = \exp(-2\Gamma_n(E_d)) \quad (14)$$
;Barrier Factor (BF)

where E_d is the relative deuteron energy and Γ_n is Gamow integral for a d-d pair in D-cluster (n-deuterons with electrons) that is defined as:

$$\Gamma_n(E_d) = (2\mu)^{1/2}/(h/\pi) \int_{r0}^{b}(V_s(R)-E_d)^{1/2}dR \quad (15)$$

Using astrophysical S-factor for strong interaction,

$$G | X_n(R) |^2_{R=r0} = vS_{2d}(E_d)/E_d \quad (16)$$

Consequently we can approximately define fusion rate as:

$$\lambda_{2d} = (vS_{2d}(E_d)/E_d) \exp(-2\Gamma_n(E_d)) \quad (17)$$

In the previous paper[1], we have estimated Gamow integral for dde* molecule, by solving Schroedinger equation to obtain screened potential $V_s(m^*/me, e^*/e)$ and evaluate the corresponding Gamow integral $\Gamma_n(m^*/m_e, e^*/e)$ by,

$$\Gamma_{n(m^*/me,e^*/e)}(E_d) = (2\mu)^{1/2}/(h/\pi) \int_{r0}^{b}(V_{s(m^*/me,e^*/e)}(R)-E_d)^{1/2}dR \quad (18)$$

Using Eq.(15) and Eq.(9) with condition of $V_s(R) \gg E_d$; $R < b$, and considering that b-parameter becomes independent own value for each quasi-particle, we can approximately obtain:

$$\Gamma_n(E_d) = b_1\Gamma_{n(1,1)}(E_d) + b_2\Gamma_{n(2,2)}(E_d) + b_4\Gamma_{n(4,4)}(E_d) + b_8\Gamma_{n(8,8)}(E_d) \quad (19)$$

To estimate coefficients b_1 through b_8, we have to solve coupled channel Schroedinger equations of normal electrons, Cooper pairs, quadru-couplings, e*(8,8) to evaluate first relative state densities of a_1 through a_8. This is a hard task to do in future.

Screened potentials $V_s(m^*/m_e,e^*/e)(R)$ were previously calculated for dde* molecular state[1] using solutions by the variational method[5], as:

$$V_{s(m^*/me,e^*/e)}(R) = V_h + e^2/R + (J + K)/(1 + \Delta) \quad (20)$$

Where the Coulomb integral J, the exchange integral K and the non-orthogonal integral Δ are given as[1]:

$$J = Z(e^2/a)[-1/y + (1 + 1/y)\exp(-2y)] \quad (21)$$

$$K = -Z(e^2/a)(1 + y)\exp(-y) \quad (22)$$

$$\Delta = (1 + y + y^2/3)\exp(-y) \quad (23)$$

With

$$y = R/a \quad (24)$$

$$a = a_0/Z/(m^*/m_e) \quad (25)$$

with $a_0 = 0.053$ nm (Bohr radius) and $Z = e^*/e$.
We also solved atomic de* system to obtain ground state energy V_h as:

$$V_h = -13.6Z^2/(m_e/m^*) \quad (26)$$

For dde*e* molecule, we have obtained screened potential function $V_{se^*e^*}$ as:

$$V_{se^*e^*}(R) = 2V_h + e^2/R + (2J + J' + 2\Delta K + K')/(1 + \Delta^2) \quad (27)$$

Where the cross-Coulomb integral J' and cross exchange integral K' are given as:

$$J' = (Z^2e^2/a)(1/y - \exp(-2y))(1/y + 11/8 + 3y/4 + y^2/6) \quad (28)$$

$$K' = (Z^2e^2/5/a)[-\exp(-2y)(-25/8 + 23y/4 + 3y^2 + y^3/3) + (y/6)((0.5772 + \log y)\Delta^2 + (\Delta')^2 Ei(-4y) - 2\Delta\Delta' Ei(-2y))] \quad (29)$$

with

$$\Delta' = \exp(-y)(1 - y + y^2/3) \quad (30)$$

$$Ei(y) = -\int_0^{\exp(-y)}(1/\log(x))dx \quad (31)$$

In these equations corrections were made for mistakes in text book[5].

For fusion rates of multi-body (nD) reactions in a D-cluster was defined[1,2] as:

$$\lambda_{nd} = [vS_{nd}(E_d)/E_d] \exp(-n\Gamma_n(E_d)) \quad (32)$$

by assuming the very fast sequential process of cascade two-body reactions for intermediate states[2]. And we have made estimate for $S_{nd}(0)$ values by using empirical scaling of known S(0)-values of H+D, D+D and D+T fusion reactions extrapolating up to unknown multibody $S_{nd}(0)$ values as a function of PEF (pion exchange force) numbers for equilaterally symmetric configuration of strong interaction (π^+ and π^- exchange) in TRF and ORF condensation[1,2]. The

second term of Eq.(32) gives mulit-body barrier factor.

4. NUMERICAL RESULTS AND DISCUSSIONS

We have done calculations of screening potentials of dde* molecules with heavy electrons (fermions) for $m^* = 1m_e$ to $208m_e$(muon), to make comparison with screening effect by quasi-particles of e*(2,2), e*(4,4) and e*(8,8).

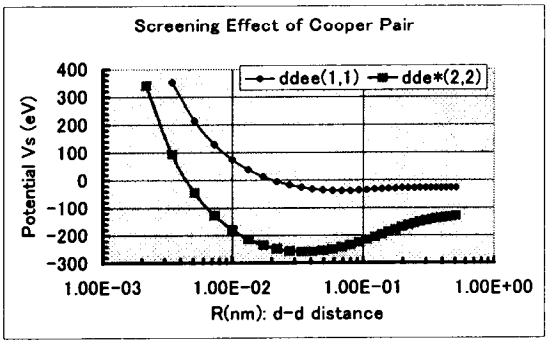

Fig.1: Screening effect of Cooper pair for dde* molecule, compared with D_2 molecule

Figure 1 shows the effect of first-step bosonization, namely generation of Cooper pair, compared with screened potential of D_2 molecule (ddee system) which has minimum potential hole (-10.6 eV) at Re = 0.07 nm. Value of b-parameter for Gamow integral is approximately given by the zero-potential crossing distance; actually we use crossing point for E_d = 2.5 eV[1], which is essential to barrier penetration calculation. Value of b-parameter moves from 20 pm for D_2 molecule to 4 pm for dde*(2,2) Cooper pair. This is drastic effect: As given in Table-1, barrier factor increases from 1E-50 with λ_{2d} = 1E-63 , for D_2, to 1E-7 with λ_{2d} = 1E-20, for Cooper pair dde*. Assuming macroscopic production density of 1E+20 (1% of D-density in PdDx, x>1) Cooper-pairs/cc, we obtain D+D (2D) fusion yield of 1 f/s/cc, that is so called Jones level[6] and lowest countable level by usual neutron detectors. We can say that Cooper pair can make great effect to drastically enhance d-d fusion rate in MDx systems. This may be the first clear theoretical evidence that "cold fusion" exists. Cooper pair generates deep hole (-256 eV) to attract deuterons and initiate D-cluster condensation[1,2].

In Fig.2, dde* potentials are compared between Cooper pair e*(2,2) and a heavy fermion e*(10,1). Screening effects are comparable.

In Fig.3, comparison is also made for quasi-particle of quadru-coupling e*(4,4) and very heavy fermion e*(100,1), to show comparable effects between the two.

Table-1: Barrier-Factors (BF) and Fusion-Rates (FR in f/s/cl), by transient quasi-particle screening

(m*/me, e*/e)	2D BF (FR)	3D BF (FR)	4D BF (FR)	8D BF (FR)
(1,1)	1E-125 (1E-137)	1E-187 (1E-193)	1E-250 (1E-252)	1E-500 (1E-499)
(2,1)	1E-53 (1E-65)	1E-80 (1E-86)	1E-106 (1E-108)	1E-212 (1E-211)
(2,2)	1E-7 (1E-20)	1E-11 (1E-17)	1E-15 (1E-17)	1E-30 (1E-29)
(4,4)	3E-4 (3E-16)	1E-5 (1E-11)	1E-7 (1E-9)	1E-14 (1E-13)
(4,4)b	4E-1 (4E-13)	2E-1 (2E-7)	1E-1 (1E-3)	2E-2 (2E-1)

Where E_d=0.22eV is assumed, which is the n=3 phonon excited state of D in PdDx lattice with $h\omega_0$ = 64 meV and $E_d = (n+1/2)h\omega_0$. And

(0,0) : Bare dd reaction

(1,1) : dde- molecule

(2,1) : dde* with heavy electron

(2,2): dde* with Cooper pairing

(4,4): dde* with quadru-coupled electrons

(4,4)b: dde* with binary quadru-coupled electrons, namely (8,8)

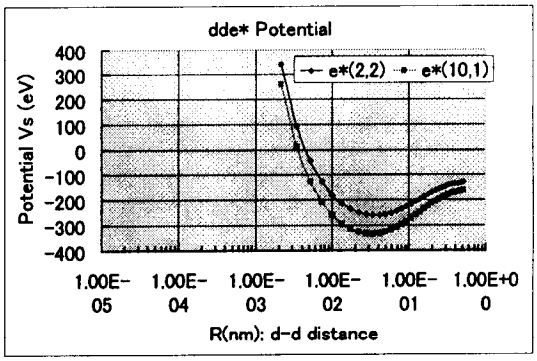

Fig.2: Comparison of screened potentials between Cooper pair and mass 10 heavy fermion

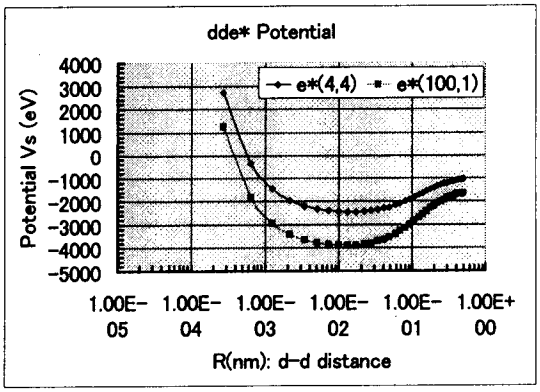

Fig.3: Comparison of screened potentials between e*(4,4) quasi-particle and mass 100 heavy fermion

Muon has $m^* = 208m_e$, so that binary Cooper coupling, namely quadru-coupling e*(4,4) works as strongly as muon for D+D fusion induction. We can say that the very heavy fermion model for high-Tc superconductivity can be replaced with the binary bosonization of two Cooper pairs to make e*(4,4) quadru-coupling. Depth of the transient deep hole[1] by e*(4,4) generation is so large as –2,460 eV, that can strongly attract surrounding deuterons with electrons to make TRF and ORF condensations at focal points. Value of b-parameter for dde*(4,4) is about 0.5 pm (500 fm), to enhance D+D barrier factor to 3E-4, and 1E-5 for 3D and 1E-7 for 4D multi-body fusion, of which fusion rate (microscopic) are 1E-16, 1E-11 and 1E-9, respectively for 2D, 3D and 4D fusion. If we assume D-cluster density of 1E20 cl/cc, we obtain fusion yield (f/s/cc) of 1E4, 1E9 and 1E11, respectively for 2D, 3D and 4D fusion, which are already "miracle" values to meet with major claims of "cold fusion" experiments. 8D fusion yield becomes significant level as 1E7 f/s/cc.

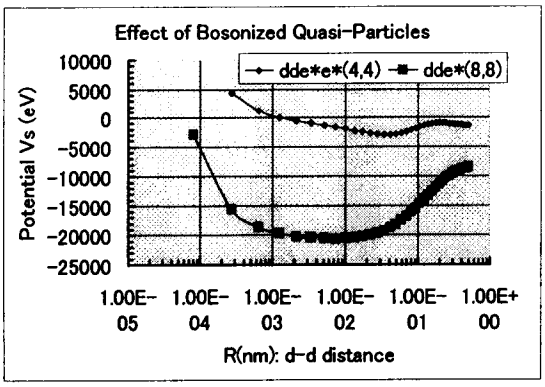

Fig.4: Bosonization effect of e*(4,4) binary quasi-particles, on screened potential

Figure 4 shows the bosonization effect of binary e*(4,4) quasi-particles. When this extreme condition is realized, we have b-parameter of 70 fm within which domain deuterons can approach as classical particles to make very condensed D-cluster for very enhanced strong interaction between 3, 4 and 8 resonant deuterons[1,2] simultaneously (within Heisenberg uncertainty) as previously discussed[1]. This screening effect of binary e*(4,4)b, namely e*(8,8) is comparable to that of heavy fermion e*(300,1). Depth of transient deep hole by e*(8,8) is very large as –20.6 keV. When we recall that the first-step goal of DT plasma temperature in TOKAMAK device is around 10 keV, e*(8,8) can provide comparable "acceleration condition", however microscopically "coherent" way. Thus 8D fusion can be winner of D-cluster fusion as discussed previously[2]. 8D fusion emits two high energy (47.6 MeV) ^{8}Be-particles, which can induce secondary capture reactions to make transmutation with mass-8-and-charge-4 increment, as recently claimed by MHI experimnet[7].

5.CONCLUSIONS

Transient deuteron clustering at focal points in metal-deuteride system may generate transient electronic quasi-particles as microscopic Cooper pairs and quadru-coupling, at room temperature. At these moments, we can expect very strong screening effect for d-d Coulomb repulsive force and drastically enhance D+D fusion rate to be in countable level, and moreover the condensed D-cluster induce 3D, 4D and 8D resonance fusion with miracle-high level of 1E11 or more f/s/cc. Generation of electronic quasi-particles (equivalently small localized bosonization, and not necessarily macroscopic superconductivity) is of key background for D-cluster fusion in condensed matter.

Major claims of "cold fusion" experiments, e.g., ^{4}He production and corresponding excess heat without intense neutrons and tritium generation, mass-8-and-charge-4 increased transmutation, anomalous 3D fusion rate enhancement, and so on, can be explained by models based on the present electronic quasi-particle screening theory.

However, since the model was based on assuming the generation of transient e*(2,2) as sub-angstrom single particle, we need further study of such extreme bosonization under time-dependent many body problem of metal-deuteride lattice (See JCF4-22).

Acknowledgment: The author acknowledges discussions and suggestions by Drs. Y. Iwamura, S. Kuribayashi and T. Itoh, Mitsubishi Heavy Industry.

References:

1) A. Takahashi: Deuteron cluster fusion in solid, submittal to Journal (private com.), July 2002
2) A. Takahashi: Tetrahedral and octahedral resonance fusion under transient condensation of deuterons at lattice focal points, Proc. ICCF9, Beijing, May 2002
3) F. Celani, et al: Proc. ICCF6, Toya Japan, pp.228-233 (1996)
4) M. Tinkham: Introduction to superconductivity, McGraw Hill (1996)
5) J. Pauling and A. Wilson: Introduction to quantum mechanics with application to chemistry, McGraw-Hill (1935)
6) S. Jones, et al: Nature, 338 (1989)737-740
7) Y. Iwamura, et al: Jpn. J. Appl. Phys. 41 (2002) 4642-4650

Mass-8-and-Charge-4 Increased Transmutation by Octahedral Resonance Fusion Model

A. Takahashi (Osaka University)*
Y. Iwamura, S. Kuribayashi (Mitsubishi H. I.)
* akito@nucl.eng.osaka-u.ac.jp

Abstract: Based on the quasi-particle expansion theory for transient deuteron clustering in PdDx lattice dynamics, possibility of selected 4D and 8D multibody fusion reactions was discussed, and transmutation with mass-8 and atomic-number 4 increase by high energy Be-8 particles by 8D fusion was suggested.

Keywords: transient quasi-particle screening, octahedral deuteron condensation, 8D fusion, Be-8, transmutation

1. Introduction

Mitsubishi H. I. Group has reported[1] extraordinary transmutation results, namely production of mass-8-and-charge(atomic number)-4 increased elements (Mo-96 and Pr-141) from Sr-88 and Cs-133 thin zone on Pd/CaO/Pd multi-layered film under deuterium permeation. By applying Takahashi's theoretical model[2,3] (EQPET: Electronic Quasi-Particle Expansion Theory) of tetrahedral (TRF) and octahedral resonance fusion (ORF) with transient quasi-particle e*(Cooper pair and quadru-coupling) generation in PdDx lattice dynamics, we attempt to explain the underlying physics of the observation.

Schematic view of octahedral condensation of deuterons in PdDx lattice dynamics is shown in Fig.1.

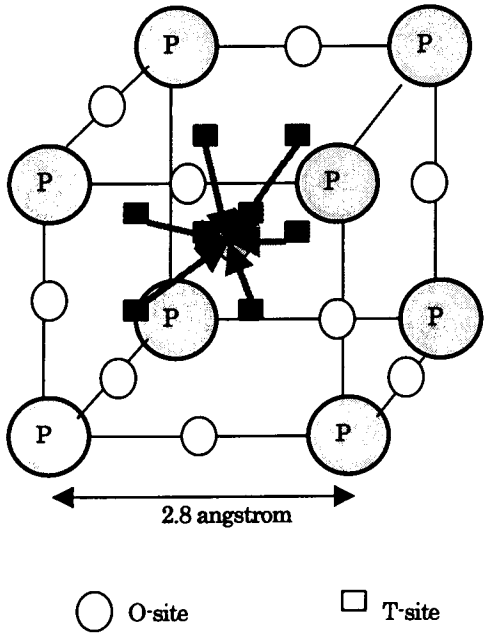

Fig.1: Octahedral condensation of deuterons from T-sites to an O-site.

In the TRF or ORF condensation, we consider the squeezing of deuterons with 4d-shell electrons of Pd, as drawn in 2-dimensional map of Fig.2.

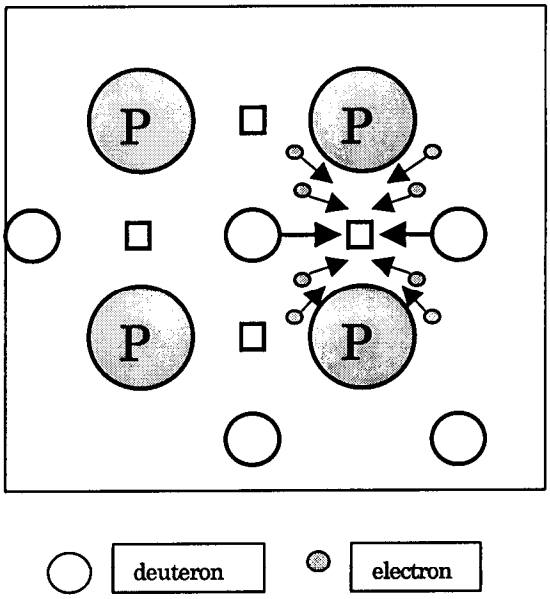

Fig.2: Transient squeezing of deuterons and electrons from O-site to T-site for TRF condensation, 2-dimensional map. P denotes palladium.

Counter approach of two deuterons, in Fig.2, attracts electrons due to attractive coulomb force between deuteron and electron. Two electrons from counter orbits of Pd 4d-shell (there are 10 4d-shell electrons per Pd atom, which attribute to conduction band) may approach closely less than 1 angstrom, since repulsive force between electrons is screened by deuteron-electron attractive force, and may have opposite momenta and spins, which may make a transient electronic quasi-particle (TEQP) like a Cooper pair, for short time interval. PdDx lattice phonon vibration and D-e plasma oscillation mediate and assist the generation of TEQP as discussed in our

JCF4-21 paper[3]. When more than two electrons per deuteron are squeezing in the system, we may consider the generation of "further bosonized" quasi-particles as e*(4,4) and e*(8,8) as we used in Ref.3. We have treated TEQP as single particle with sub-angstrom size. This assumption may be supported by the interesting simulation by Kirkinskii and Novikov in Russia[5].

2. EODD Model and EQPET

Kirkinskii and Novikov proposed the EODD (Electron Orbital Deformation Dynamics) model to treat the lattice dynamics in similar system as shown in Fig.2. The EODD method is a kind of Monte-Carlo Molecular Dynamics calculation taking into account deformation of 5s + 4d shell electron-orbits by approach of two counter deuterons. They estimated the probability distribution of minimal pairing distances R_{dd} of deuterons, which showed a broadly peaked distribution in 0.5 to 2 angstrom region, probably reflecting minimum potential positions 1.1 and 0.7 angstrom respectively for dde and ddee (D_2) molecular states, and very interestingly steeply increasing component in lower R_{dd} region less than 0.2 angstrom, as shown in Fig.3.

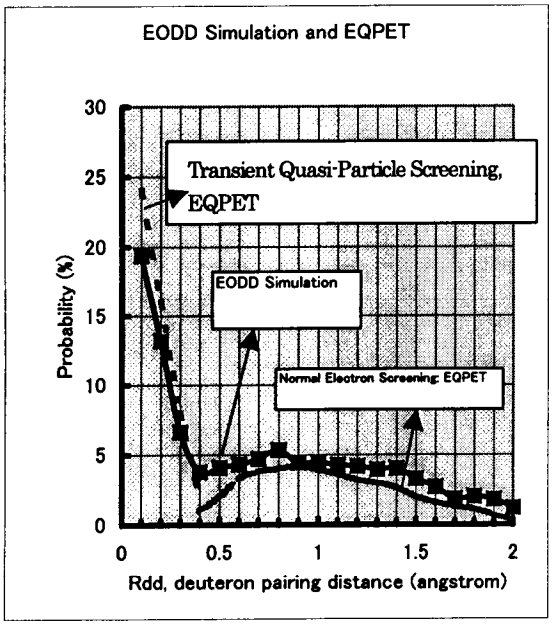

Fig.3: EODD simulation and EQPET, the lower R_{dd} component is described by transient quasi-particle expansion

EODD simulation has given about 19 % probability to have closely-packed transient d-d pairs with less than 0.1 angstrom (even in 0.01 angstrom region) inter-nuclear distance which gives very enhanced fusion rate as 1E-10 f/s/pair level[5]. It is regarded that this component realizes visible "cold fusion events". From our EQPET calculation, this component can be described as linear combination of TEQP components, namely dde*(2,2), dde*(2,2)e*(2,2), dde*(4,4) and dde*(8,8), etc., transient molecular states of EQPET theory[3]. This means that ,when we will get 3-dimensional EODD simulations for TRF and ORF systems , we will be able to fit the result with the combination of normal electron (dde + ddee) and transient quasi-particle screening (dde* + dde*e*) components (wave functions X for d-d Schroedinger equation)[3]. This should give the basis of EQPET.

3. Octahedral Resonance Fusion

As we have seen that transient dde* states give very deep potential holes [3] (-0.25 keV by dde*(2,2) to –22 keV by dde*(8,8)), there happens enhanced possibility to attract 4-8 deuterons with electrons at focal points (T-site for TRF, and O-site for ORF). We may expect 4D and 8D fusion as resonant multi-body fusion[2,3]. This model may explain the MHI experiment[1].

The schematic view of the MHI experiment's condition is shown in Fig.4.

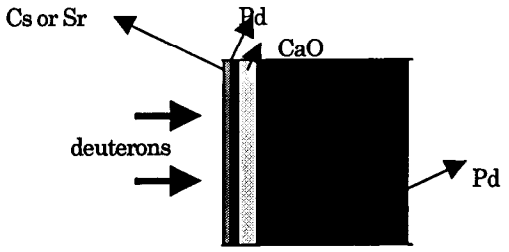

Fig.4: Schematic view of the MHI experimental condition[1]

The CaO layer (100 nm thick) is considered to make significant gap of Fermi levels in the interface region between CaO and thin (40 nm) Pd layer on which about 2 nm thin test sample (Sr or Cs) zone was made. Constant D-flow from sample zone to backing thick (0.1 mm) Pd zone would continue to satisfy overloading (PdDx, x>1) and site-to-site diffusion condition in the thin surface zone of Pd, where local superconductivity-like condition around focal points generating transient electronic quasi-particles e*s can be expected due to strong phonon-electron (Pd 4d shell) coupling by D-plasma oscillation (about 10^{14} s^{-1} frequency) and squeezing of deuterons with electrons as simulated by EODD, in transient dynamics of D-cluster condensation at T- or O-sites[2]. Celani reported[4] anomalous reduction of resistance of

Pd-wire under over-loading PdDx condition, and we conceive that was the occurrence of superconductivity.

Very deep (-260 eV by e*(2,2) transient Cooper pair and –2460 eV by e*(4,4) transient quadru-coupling) transient potential holes, born by the generation of e*, strongly attract electrons and D-clusters (4D for TRF and 8D for ORF) . At the case of more than two e*s generation per 8D-cluster, 8D-cluster can condense within 80 fm domain[3] where quantum mechanical tunneling interaction of simultaneous multi-body fusion[2] may be drastically enhanced in competition of the following reactions;

0) 2D → n + ^{3}He + 3.25MeV, p+T +4.02 MeV
1) 3D → Li-6* → t + He-3 +9.5 MeV
2) 4D → Be-8* → 2xHe-4 +47.6 MeV
3) 5D → B-10* (53.7 MeV)
4) 6D → C-12* (75.73 MeV)
5) 7D → N-14* (89.08 MeV)
6) 8D →O-16* (109.84 MeV) →2xBe-8 +95.2 MeV

The EODD simulation by Kirkinskii and Novikov has shown that about 19 % of d-d pairing with less than 0.1 angstrom inter-nuclear distance could be born as shown in Fig.3. This component can be regarded as components of dde*(4,4) and dde*(8,8). And very high density of about 1E+22 dde* pairs per cubic centimeters can be expected, to further initiate 4D and 8D fusion reactions, selectively. The additional reason of selectivity of 4D and 8D fusion is as follows: Because of resonant strong interaction by 3-dimensionally symmetric pion exchange[2] for TRF and ORF process, 2D, 3D, 4D and 8D fusion reactions are selectively enhanced. Especially with the existence of plural quadru-coupling e*(4,4) quasi-particles, 8D fusion process can be winner (1E-1 f/s/cluster at best)[3] of the competition and generate very high energy Be-8 particles (47.6MeV).

4. Transmutation Reactions

Be-8 particles with 47.6 MeV high kinetic energy can make easy secondary capture (fusion) reactions with existing heavy nuclei as Sr-88 or Cs-133, due to large contact surface of Be-8 deformed nucleus and Sr or Cs nucleus for high energy fusion process, as

7) Sr-88 + Be-8 (47.6MeV)→ Mo-96*(Ex) + KE
8) Cs-133 + Be-8(47.6MeV) → Pr-141*(Ex) + KE

Considering a liquid drop like character of above collision processes, the very high kinetic energy of Be-8 may be transferred to kinetic energy (KE) of Mo-96 or Pr-141, which may be deposited to lattice phonon energy by heavy particle slowing down process, without hard X- or gamma-ray radiation.

The process is illustrated in Fig.5;

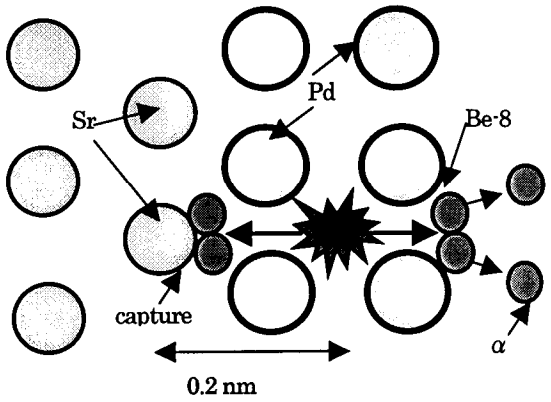

Fig.5: What happens near interface

5. Conclusions

The transient bosonization effect of electrons in the dynamic squeezing of deuterons and electrons at lattice-focal points for TRF and ORF systems can generate transient d-d pairs with close d-d inter-nuclear distance less than 0.1 angstrom which may enhance d-d fusion rates over visible level (more than1E-20 f/s/pair). Moreover, deep transient potential holes by TEQP generation can induce resonant multi-body fusion of 4D and 8D fusion. High energy Be-8 particles by 8D fusion can make secondary reactions to produce transmuted elements with mass 8 and charge 4 increase.

We need however analysis by 3-dimensional EODD simulation to understand more about the process.

References:

1)Y. Iwamura, et al: observation of low energy nuclear reactions by D_2 gas permeation through Pd complexes, Proc. ICCF9, May 19-23, 2002, Beijing, China; also see Jpn. J. Appl. Phys., Vol.41(2002) pp.4462-4650

2)A. Takahashi: tetrahedral and octahedral resonance fusion under transient condensation of deuterons at lattice focal points, Proc. ICCF9, May 19-23, 2002, Beijing China

3)A. Takahashi: drastic enhancement of D-cluster fusion by electronic quasi-particle screening, JCF4-21 (this meeting), Oct. 17-18, 2002,Iwate-U, Morioka, Japan

4)F. Celani, et al: observation of strong resistivity reduction in a palladium thin long wire using ultra-high frequency pulsed electrolysis at D/Pd>1, Proc. ICCF6, pp.228-233 (1996)

5) V. Kirkinskii and Y. Novikov: Theoretical Modeling of Cold Fusion, Nobosivirsk State University, 2002

External and internal causes of nuclear reaction within solids

Norio YABUUCHI
High Scientific Research Laboratory
204 Maruzen Building
Tsu City, Mie 514-0033, JAPAN
E-mail yabu333@lilac.ocn.ne.jp

Key words: quantum-confinement effect, super-heavy hydrogen isotope element, Platonic regular polyhedral structure, halo nucleus, bubble effect

Abstract

Nuclear fusion is believed to have internal and external causes. The author believes that an internal cause is found in the structure of the atomic nuclei as Platonic regular polyhedra, and an external cause is to be found in the quantum-confinement effect.
Firstly, the internal cause, Platonic regular polyhedral structure, is discussed. Because a Platonic regular polyhedron may be both inscribed and circumscribed on spherical surfaces, the shell structure is formed by overlapping concentric spheres, in the it is believed that protons and neutrons exist at the apices of the regular polyhedron inscribed on a concentric sphere. Accordingly, for elements with larger atomic numbers, other protons and neutrons are thought to exist at the apices of regular polyhedra inscribed on other concentric spheres.
Secondly, the quantum-confinement effect is believed to be an external cause. When a crack in a hydrogen-absorbing metal contains a large number of deuterons at one time, density becomes extremely high, the range of existence for each deuteron contracts, and due to Heisenberg's uncertainty principle, $\Delta x \Delta p \leqq \Delta h$, $\Delta x \rightarrow 0 \therefore \Delta p \rightarrow \infty$, and because of Yabuuchi's formula, $\int mvdv = 1/2mv^2 + C$, $1/2mv^2 \rightarrow \infty$. Thus the interior of the crack becomes hot, movement between atomic nuclei is excited, and collision occurs, resulting in thermonuclear fusion.

1. Structure of the atomic nucleus

The Platonic structure of the atomic nucleus as intuitively understood by the author is as follows. A tetrahedron, indicated by T, has four apices, and a neutron (n) or proton (p) exists at each apex. Similarly, a cube (C) has eight apices, an octahedron (O) has six, an icosahedron (I) has 12, and a dodecahedron (D) has 20, with an n or p at each.
Because a Platonic regular polyhedron may be both inscribed and circumscribed on spherical surfaces, spheres having the same center and different radii form shells, with regular polyhedra both inscribed and circumscribed on each, thereby forming superimposed layers.
A $^4He_2$ nucleus has a T structure, and at

its four apices there are two p and two n. Accordingly,

$^{4}He_{2}[T] = (2n + 2p)$ (1-1)

Next,

$^{16}O_{8}[T,I] = (2n + 2p, 6n + 6p) = (8n + 8p)$ (1-2)

Here, the I is circumscribed on the sphere on which the T is inscribed, with two n and two p in the inner shell and six n and six p on the outer shell, for a total of eight n and eight p.

Next,

$^{40}Ca_{20}[C,I,D] = (4n + 4p, 6n + 6p, 10n + 10p) = (20n + 20p)$

Also,

$^{60}Ni_{28}[C,D][T][C,D] = (4n + 4p, 10n + 10p)\ (4n)\ (4n + 4p, 10n + 10p)$

$= (14n + 14p)\ (4n)\ (14n + 14p)$

$= (28n + 28p + 4n)$ (1-3)

This has a [T] sphere interposed between and interlinked with two [C,D] spheres.

Next,

$^{118}S_{50}[T,C,O,I,D][T,C,O][T,C,O,I,D]$

$= (25n + 25p)\ (18n)\ (25n + 25p) = (50n + 50p + 18n)$ (1-4)

Next,

$^{208}Pb_{82}[T,C,O,I,D][C][I,D][C,D][I,D][C][T,C,O,I,D]$

$= (25n + 25p)\ (8n)\ (16p + 16n)\ (28n)\ (16p + 16n)\ (8n)\ (25n + 25p)$

$= (126n + 82p)$ (1-5)

Here, the magic numbers 2, 8, 20, 28, 50, 82, and 126 are obtained by fulfilling the structure of regular polyhedra. They yield a nuclear structure that is stable. The correctness of the Yabuuchi model of the atomic nucleus according to the structure of Platonic regular polyhedra is verified by the following explanation of the nuclear-fission ratio of uranium (see Figure 1).

$^{238}U_{92}[C,O,I,D][T][C,O,I,D][C,O,I,D][C,O,I,D][T][C,O,I,D]$

$= (23n + 23p)\ (4n)\ (23n + 23p)\ (46n)$

$96 \quad \uparrow \quad 140 + 2$

$(23n + 23p)\ (4n)\ (23n + 23p)$ (1-6)

Fission of uranium238 atom at an atomic weight of 96:140 is shown by the arrow in equation (1-6). It is believed that two nucleons are split by collision with an incident neutron. This explains why fission of uranium occurs at an atomic-weight ratio of 96 to 140.

One more point may be noted with respect to nuclear fission. When $^{56}Fe_{26}$ is included as an impurity in a palladium solid, it has the Platonic structure shown in Figure 2. According to the theory of Victor Weisskopf, large absorption of neutron resonance takes place at atomic weights near 11, 55, and 155; because the atomic weight of $^{56}Fe_{26}$ is close to 55, a similar phenomenon is likely to occur. Accordingly,

$^{56}Fe_{26}[C,O,I][T][C,O,I]$

$= (4n + 4p, 3n + 3p, 6n + 6p)\ (4n)\ (4n + 4p, 3n + 3p, 6n + 6p)$

$= (13n + 13p)\ (4n)\ (13n + 13p)$ (1-7)

When the (4n) absorbs a large number of neutrons, the T configuration is disrupted, and so the two lateral (13n + 13p) experience nuclear fission. Beta decay then produces either

$^{56}Fe_{26} + n \rightarrow {}^{26}Al_{13} + {}^{26}A_{13} + {}^{4}He_{2} + n + \Delta E$ (1-8)

or

$^{56}Fe_{26} + n \rightarrow {}^{26}Al_{13} + {}^{26}A_{13} + 2n + T + \Delta E$ (1-9)

2. Quantum-confinement effect

An unlimited large number of deuterium D, which are Bose particles, collect in a crack in a palladium solid irrespective of Pauli's exclusion principle, and so contraction occurs.

Instruction is believed that when cosmic-ray neutrons strike this, the D nuclei capture the neutrons and produce large amounts of super-heavy hydrogen isotope elements, such as ^{3}H, ^{4}H, ^{5}H, ^{6}H, ^{7}H, and so on. When contraction occurs, the existence range Δx of each nucleus becomes $\Delta x \rightarrow 0$, an $\Delta p \rightarrow \infty$ due to the Heisenberg uncertainty principle, and fusion takes place due to the external cause.

The reason for this is that because Yabuuchi's formula holds that $\int mvdv = 1/2mv^2 + C$, and so when Δm for D, H, and the like becomes larger, $1/2mv^2 \rightarrow \infty$, thereby increasing, and the required energy for fusion occurs.

For example,

$^{3}H_1 + {}^{6}H_1 \rightarrow {}^{4}He_2 + 4n + n + \Delta E$ (2-1)

The $^{3}H_1$ atom is a tetrahedron with one missing proton, and because the number of protons is one less than the magic number 2, the nucleus, strongly seeking stability, overcomes the Coulomb barrier and actively accepts a p.

The $^{6}H_1$ nucleus is a tetrahedron with two extra neutrons (2n), forming a halo nucleus; its configuration resembles that of a $^{4}H_1$ nucleus with two more n at a considerable distance from the nucleus. Accordingly, because the two extra neutrons 2n in the $^{6}H_1$ nucleus forcefully overcome the Coulomb barrier and so fusion with $^{3}H_1$ can be accomplished easily.

In this case, the crack in which the deuterium exists in a contracted state is like a "sea" of deuterium, and in the super-heavy hydrogen isotope elements, $^{n}H_1$ nuclei stabilize, as bubbles in seawater are more stable than bubbles in the air, and seek nuclear fusion. This could be termed the bubble effect.

References

1. Y. Iwamura, "Detection of anomalous elements, X-ray, and excess heat in D_2-Pd system and its interpretation by the electron-induced nuclear reaction model." *Fusion Technology*, vol. 33, No. 4, pp 387-500 (July 1998).
2. Victor F. Weisskopf and E.P. Rosenbaum, "A Model of the Nucleus," *Scientific American*, December 1955, vol. 193, No. 6, pp 84-91.
3. M. Brack, "Metal Clusters and Magic Numbers." *Scientific American* (December 1997).
4. W. Green, *Cold Fusion*, issue 12, pp 28, 29, and 31 (1995).
5. C. Illert, *Cold Fusion*, issue 13, pp 28-29 (1995).
6. N. Yabuuchi, "Low-Speed Nuclear Fusion." *Cold Fusion, issue* 17, pp 16, 17, 18, 19, and 11 (1996)
7. T. Mizuno, T. Omori, and M. Enyo, *Journal of New Energy*, vol. 1, No. 3, pp 13-45, Fig. 5 (1996).
8. Sam M. Austin and George F. Bertsch, "Halo Nuclei." *Scientific American* (June 1995).
9. N. Yabuuchi, *Proceedings: Fourth International Conference on Cold Fusion, vol. 4; Theory and Special Topics Papers*. TR-104188-V4

Structural diagram of $^{238}U_{92}$ atomic nucleus based on Platonic philosophy

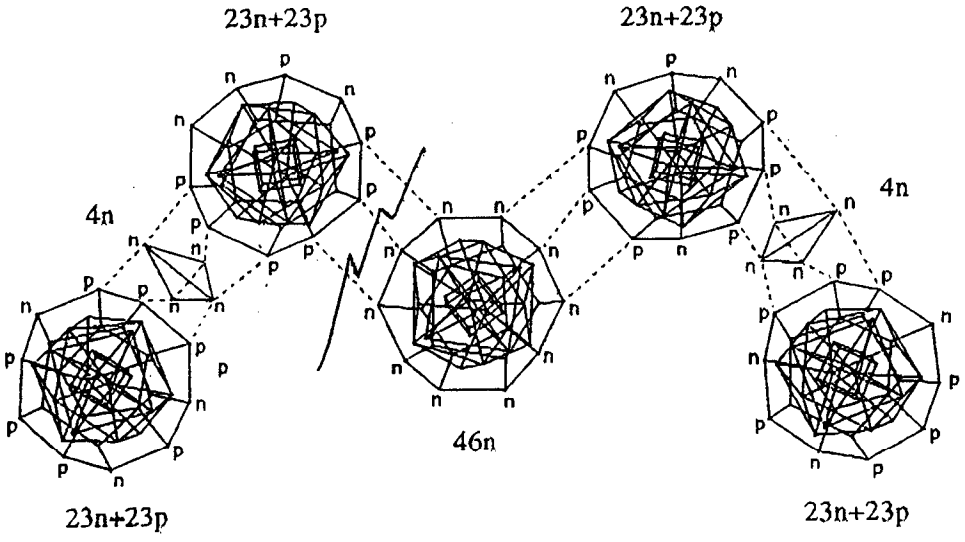

Easily destroyed because mutual attraction between neutrons is weak

Fig. 1

Structural diagram of $^{56}Fe_{26}$ atomic nucleus based on Platonic philosophy

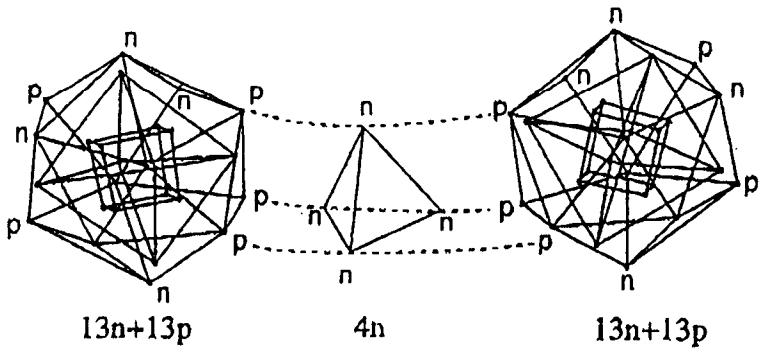

Fig. 2

A POSSIBLE MODEL FOR THE NUCLEAR REACTIONS IN METAL VACANCY INDUCED BY BOSE-EINSTEIN CONDENSATION

Ken-ichi TSUCHIYA

Department of Chemical Science and Engineering, Tokyo National College of Technology,
1220-2 Kunugida, Hachioji, Tokyo 193-0997, e-mail: tsuchiya@tokyo-ct.ac.jp

ABSTRACT: Bose-Einstein condensation (BEC) is one of the candidates to induce the nuclear reaction in solids, because deuterons in solids are regarded as Bose particles. In this work, the d-d fusion rate in Pd induced by BEC is estimated. The equivalent linear two-body method, which is based on the approximate reduction of many-body problems by variational principle, is used for the calculation.
Keywords: Bose-Einstein condensation, cold fusion

1. INTRODUCTION

When charged bosons are confined in ion trap[1], the Hamiltonian for the system is given by the summation of three terms. They are total kinetic energy, isotropic harmonic potential due to ion trap and repulsive Coulomb interaction between charged bosons. By applying equivalent linear two-body (ELTB) method to these many-body problems, Y.E.Kim et al. [2] derived the ground-state wave function and the nucleus-nucleus fusion rate.

In this work, Kim's theory is modified in the following two points. Firstly, vacancies in solid are regarded as harmonic ion traps and the frequency of this potential is estimated by using spherical approximation. The ELTB ground state wave function can be calculated numerically and also the rate of nuclear fusion in some kinds of lattice defects including N charged bosons can be obtained. Secondly, the dependence of this phenomenon on the temperature is introduced by using the well-known formula for the critical temperature of BEC, which depends on the number density of the particle.

2. APPLICATION OF KIM'S METHOD TO THE PHENOMENON IN SOLIDS

Firstly, we show the outline of Kim's method. They regarded the potential of the ion trap as the isotropic harmonic potential. Therefore the Hamiltonian of the system including N charged particle is then

$$\mathcal{H} = -\frac{\hbar^2}{2m}\sum_{i=1}^{N}\nabla_i^2 + \frac{m\omega^2}{2}\sum_{i=1}^{N}\mathbf{r}_i^2 + \sum_{i<j}\frac{e^2}{|\mathbf{r}_i-\mathbf{r}_j|}, \quad (1)$$

where m is the rest mass of the nucleus and $\mathbf{r}_i$ is the position of the i-th nucleus. They used ELTB method, which is based on the variational principle. The ground state of this many-body problem is written as

$$\Psi(\mathbf{r}_1,\mathbf{r}_2,.....,\mathbf{r}_N) \approx \frac{\phi(\rho)}{\rho^{(3N-1)/2}}, \quad (2)$$

where new quantity ρ is defined as

$$\rho = \left(\sum_{i=1}^{N}\mathbf{r}_i^2\right)^{1/2}. \quad (3)$$

The wave function ϕ in eq.(2) satisfies

$$\left\{-\frac{\hbar^2}{2m}\frac{d^2}{d\rho^2} + \frac{m\omega^2\rho^2}{2} + \frac{\hbar^2}{2m}\frac{(3N-1)(3N-3)}{4\rho^2} + \frac{2N\Gamma\left(\frac{3N}{2}\right)}{3\sqrt{2\pi}\Gamma\left(\frac{3(N-1)}{2}\right)}\frac{e^2}{\rho}\right\}\phi(\rho) = E\phi(\rho). \quad (4)$$

Generally, these equations for harmonic oscillator are rewritten by using nondimensional quantities $x = \sqrt{\frac{m\omega}{\hbar}}\rho$ and $\varepsilon = 2E/\hbar\omega$. As a result, eq.(4) is rewritten as

$$\left(-\frac{d^2}{dx^2} + x^2 + \frac{p}{x^2} + \frac{q}{x}\right)\phi(x) = \varepsilon\phi(x), \quad (5)$$

where p and q are defined as

$$p = \frac{(3N-1)(3N-3)}{4} \quad (6)$$

and

$$q = \alpha\sqrt{\frac{mc^2}{\hbar\omega}}\frac{4N\Gamma\left(\frac{3N}{2}\right)}{3\sqrt{2\pi}\Gamma\left(\frac{3(N-1)}{2}\right)}, \quad (7)$$

where α is the fine structure constant. Kim et al.[2] discussed the possibility of cold fusion in ion trap[1] by using these equations.

Secondly, we show the application of Kim's method to the phenomenon in solid. In eqs.(4) and (5), harmonic term is the electro magnetically induced attractive potential in the ion trap device[1].

For the case of the problems in crystalline solids, this term corresponds to the repulsive interaction between host ions and impurity deuterons. Therefore the Hamiltonian of this system is written as

$$\mathcal{H} = -\frac{\hbar^2}{2m}\sum_{i=1}^{N}\nabla_i^2 + \sum_{ij}\frac{Ze^2\exp(-k|\mathbf{R}_j-\mathbf{r}_i|)}{|\mathbf{R}_j-\mathbf{r}_i|} + \sum_{i<j}\frac{e^2}{|\mathbf{r}_i-\mathbf{r}_j|}, \quad (8)$$

where $\mathbf{R}_j$ is the Bravais lattice vector of the host lattice and Z is the effective charge of a host ion. By intuitive estimation, the 2nd term in eq.(8) is approximately harmonic at the center of the vacancy in the crystalline solids. This can be explained as following. The i-th component of the 2nd term in eq.(8) can be expanded into spherical harmonics as

$$\sum_j \frac{Ze^2\exp(-k|\mathbf{R}_j-\mathbf{r}_i|)}{|\mathbf{R}_j-\mathbf{r}_i|} = \sum_{lm} A_{lm}(r_i)Y_{lm}(\theta,\phi). \quad (9)$$

If this is approximately spherical function, dominant term in the expansion is the $l=m=0$ component, which is written as

$$A_{00}(r_i)Y_{00}(\theta,\phi) = Ze^2\frac{\sinh kr_i}{kr_i}\sum_j\frac{\exp(-kR_j)}{R_j}. \quad (10)$$

In this equation, $\sinh kr/kr$ is expanded as

$$\frac{\sinh kr}{kr} = 1+\frac{(kr)^2}{6}+O\{(kr)^4\}. \quad (11)$$

This means that the second term of eq.(8) is approximately expressed by the summation of constant and harmonic terms for small kr. Therefore, if we define ω as

$$\frac{Ze^2k^2}{6}\sum_j\frac{\exp(-kR_j)}{R_j} \equiv \frac{1}{2}m\omega^2, \quad (12)$$

eq.(8) is completely same with eq.(1). Seeing eq.(12), it is clear that the value of ω is determined by the lattice summation. In this calculation, the origin of the Bravais lattice vector is selected as the center of the vacancy.

The ELTB solution gives the nuclear reaction rate as

$$R = -\frac{2}{\hbar}\frac{\sum_{i<j}<\Psi|ImV_{ij}^F|\Psi>}{<\Psi|\Psi>}, \quad (13)$$

where imaginary part of Fermi pseudopotential[2,3] is written as

$$ImV_{ij}^F = -\frac{A\hbar}{2}\delta(\mathbf{r}_i-\mathbf{r}_j). \quad (14)$$

The short-range interactions of nuclear forces between two Bose nuclei are introduced by using δ function[2,3]. This rate can be calculated by using numerical solution of eq.(5), because ϕ gives the ground-state wave function Ψ for N identical Bose nuclei in eq.(13). For the normalized ϕ, it is done by using

$$R = \frac{AN(N-1)\Gamma(\frac{3N}{2})\left(\frac{m\omega}{\hbar}\right)^{\frac{3}{2}}\int_0^\infty dx\phi^2(x)/x^3}{2\pi^{\frac{3}{2}}\Gamma(\frac{3(N-1)}{2})}, \quad (15)$$

where A is given by

$$A = \frac{2Sr_B}{\pi\hbar}. \quad (16)$$

The constant A is determined by $r_B=\hbar^2/me^2$ and the S factor of the nuclear reaction between two nuclei.

3. RESULTS AND DISCUSSIONS

3.1 Four deuterons trapped in a vacancy

In this work, ELTB solutions for the system including four deuterons trapped in a vacancy in fcc Pd lattice have been obtained numerically, and d-d nuclear reaction rate has been estimated. The calculations were performed within the following conditions.

(i) In eq.(12), only the nearest neighbor lattice points are counted into the summation.

(ii) The screening constant in eqs.(5) and (12) is 2/(the first nearest neighbor (NN) distance). This means that impurity ions at the center of the vacancy are nearly free from host ions.

(iii) The effective charge of a host Pd ion is one.

(iv) The value of the S factor is 110kevb. This is consistent with Kim[2].

Using above conditions and 1NN distance = $\frac{\sqrt{2}}{2}a = 2.75$Å, where a=3.89Å is the lattice constant of fcc Pd, we find ω from eq.(12) to be

$$\omega \approx 1.12\times10^{14}sec^{-1} \quad (17)$$

and obtain the ground-state solution from eq.(5) for the case of the system including four deuterons in a vacancy, which is plotted in Fig.1. Seeing this, a sharp peak exists at $x\approx24.5$. This value corresponds to $\rho\approx4.65$Å. If $|\mathbf{r}_i|=r$ for all i in eq.(3), we obtain $\rho=\sqrt{N}r$. In this case, we obtain $r=\rho/\sqrt{4}\approx2.33$Å, which is smaller than 1NN distance. This means that deuterons are trapped in a vacancy.

Using the value of ω and numerical solution ϕ, the nuclear reaction rate is obtained from eq.(15). As a result we find R to be

$$R = 1.8\times10^{7}\ sec^{-1}. \quad (18)$$

This is extremely high, however if we consider the probability of the ground-state occupation Ω, which depends on the critical temperature T_c of BEC, it is not always high rate, because $R\Omega$ may be small. The well known formula for T_c of BEC is written as

$$T_c = \frac{h^2}{2\pi m k_B}\left(\frac{n}{\zeta(\frac{3}{2})}\right)^{2/3}, \qquad (19)$$

where n is the number density of Bose particles. In this case, deuterons are trapped in sharp peak in Fig.1. In 3-dimensional space, this means that the deuterons are trapped in the space between two concentric sphere, whose radii are $r_1 \approx 2.24$Å$(x \approx 23)$ and $r_2 \approx 2.50$Å$(x \approx 26)$. By using these values, we obtain $T_c = 107K$ from eq.(19). This temperature gives probability of the ground-state occupation. It is written as

$$\Omega = 1 - \left(\frac{T}{T_c}\right)^{2/3} \quad for\ T < T_c\ . \qquad (20)$$

If the temperature T is slightly lower than T_c, Ω should be very small. If a nuclear fusion happens in a vacancy in spite of the case of such a small probability, temperature becomes higher than T_c immediately. Then Ω becomes zero. And the reaction will be stopped. This is another reason why $R \approx 1.8 \times 10^7\ sec^{-1}$ is not always high rate.

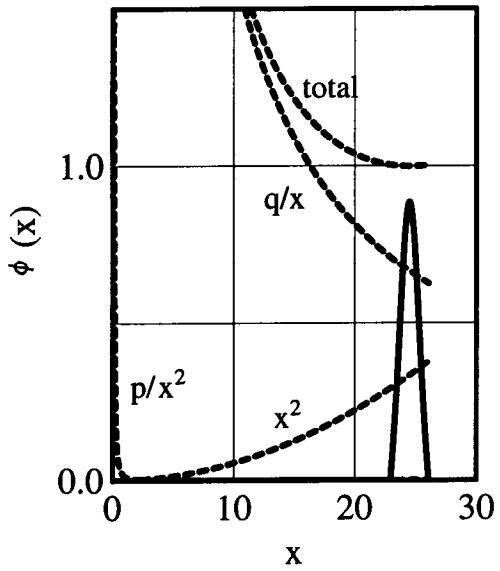

Fig.1
The ELTB solution for the system including four deuterons in fcc Pd vacancy.
The solid line means the ELTB solution. The dashed lines mean each potential in eq.(5) normalized by ε.

3.2 Other cases

We consider other cases for the trapped deuterons in some kinds of lattice defects. In this paper, they are called T, O, Vac, VacT and VacO. Table 1 summarizes the definition of them.

Table 1 Definition of traps

traps	meaning
T	T site
O	O site
Vac	single vacancy
VacT	tetrahedral void, which is constructed by 4 vacancies
VacO	octahedral void, which is constructed by 6 vacancies

For every site, calculated results of nuclear reaction rates are given in Table 2. In eq.(3), if all the particles exist at the same radial component r, ρ would become $\sqrt{N}r$. Therefore, if a position of a sharp peak in ELTB solution is smaller than $\sqrt{N}R_v$, where R_v is the radius of the defect, we can say that the condensed deuterons are trapped in the defect. This values are also given in Table 2. In this calculation, the convergences of the lattice summations are kept to be smaller than 1%. In order two clear this condition, more than 20th nearest neighbor (NN) lattice points should be needed.

Table 2 Nuclear Reaction Rate

traps	N	ρ_{max}	$\sqrt{N}R_v$	T_c	R
T	3	2.65	2.92	133	2.6
	5	4.36	3.77	160	5.2
	8	6.69	4.76	198	9.1
	10	8.15	5.33	221	12.5
O	3	2.69	3.37	129	2.5
	5	4.42	4.35	156	5.0
	8	6.79	5.50	193	8.7
	10	8.27	6.15	215	12.0
Vac	3	2.98	4.76	107	1.8
	5	4.90	6.15	129	3.7
	8	7.52	7.78	160	6.4
	10	9.16	8.70	178	8.2
VacT	3	3.31	5.59	88	1.3
	5	5.46	7.21	106	2.6
	8	8.38	9.12	131	4.6
	10	10.20	10.20	146	5.9
VacO	3	3.51	5.83	79	1.1
	5	5.58	7.53	96	2.2
	8	8.87	9.52	118	3.9
	10	10.80	10.70	132	5.0

N: the number of the trapped deuterons
ρ_{max}: position of a peak in ELTB solution [Å]
R_v: radius of the spherical defect [Å]
T_c: critical temperature of BEC [K]
R: nuclear reaction rate $[10^7 s^{-1}]$

Table 2 indicates following things.

(i) T and O can trap 2 or 3 deuterons.

(ii) Vac can trap 5 deuterons.

(iii) VacT and VacO can trap 7 or 8 deuterons.

(iv) The nuclear reaction rates are $10^7 sec^{-1}$

(v) T_c is lower than room temperature.

These results lead us to the conclusion that BEC of condensed deuterons trapped in the lattice defect can induce cold fusion.

ACNOWLEDGEMENTS

The author wishes to thank Professor Yamada (Iwate Univ.) for helpful discussions and encouragements.

REFERENCES

[1] Ghosh PK,"Ion Traps",
Oxford Clarendon Press, 1995

[2] Kim YE and Zubarev AL, "Nuclear Fusion for Bose Nuclei Confined in Ion Trap",
Fusion Technology,p151-156,**37**(2000)

[3] J.L.Bohn, B.D.Esry and C.H.Greene,
"Effective Potentials for Dilute Bose-Einsein Condensates",
Phys.Rev.A,p584-597,**58**(1998)

COMPOSITION OF 1/f AMPLITUDES ELECTRON WAVE AND A WORK OF ONE DIMENSION OF LATTICE

Masanobu BAN, Tokyo Metropolitan Industrial Technology Research Institute: banm0k@iri.metro.tokyo.jp

Abstract: Electron wave synthesizes the generation of heat that is an anomaly. Electron wave of cold cathode lay is resonant, and it synthesizes a lattice. A lattice of virtual image acts like it of crystal, and tunnel resonance phenomena is generated from the transportation of an electron. Resonance has the component that the amplitude is in inverse proportion to height of frequency. A characteristic looks just like rectangular wave of soliton. The standing wave which rose in resonance forms a lattice as teeth of a comb. Thus Shrödinger equation is remade by one dimension of new equation to solve resonance because Kirchhoff's law is one dimension of equation. Because virial theorem acts by a lattice of synthesis, one part of energy is saved in vibration of a lattice from propagation of phonon. A work of each stair in a lattice stores big energy. Cold fusion energy of large unit is produced by quantum nature of new equation.
Keywords: 1/f noise, soliton, transition probability, electron, tunnel effect, electron wave, electrons duality, cold fusion

1. INTRODUCTION

A phenomenon of abnormal heat can be generated by the direct current electric circuit that an electric discharge was generated in an electrode gap.

For example, in a phenomenon of electrostatic cooling, a change or a transportation of sudden thermal energy that does depend on non-convection, non-emission and non heat-conduction is observed in whichever of plus and minus by a condition of circumference.[1] When cold cathode lay was irradiated to the plate which was injected deuterium to aluminum or palladium, there can be an anomalous generation of heat phenomenon in a cold fusion.

In principle of causality about the consequence that produced the anomalous generation of heat, there is the inception common to two kinds of phenomenon to an electron-wave (de Broglie material wave) of direct current cold cathode lay. The kinds of one is an electrostatic cooling and the other one is a Cold fusion. Both of those have an electrode gap.

Energy of lattice vibration generated in a composition molecule of deuterium atoms as promotion factor of generation of heat works, and it becomes an opportunity, and the mass of deuterium may be converted into thermal energy.

Because there was the electrostatic-cooling phenomenon which became hot without a action of deuterium, basic cause of heat is electron-wave and tunnel resonance phenomena.

The Imagery of electron-wave group will make a lattice. Even if matter does not exist in it, the lattice is made a composition and it will become state of tunnel resonance.

The tunnel resonance phenomena of an electron-wave group is cause of generation of heat.

2. 1/f NOISE CURRENT OF CATHODE LAY

1/f noise current will occur in electric circuit made cold cathode lay by needle electrode pointed to anode plane. Wave has the amplitude of inverse proportion in each frequency, and a lot of wave is added, and special resonance is generated in a wave.

When electric field inclination is steep by needle cathode, cold cathode lay propagates toward anode. The transmission electron microscopes and the tunneling electron microscopes include this construction. Electrode gap of electrolysis or it of electroplating has this structure.

And in hologram equipment, electric field of biprism divided one electron into two electron-waves (plural material wave), and diffraction got up, and interference fringe of cold cathode lay was made with hologram equipment by the waves.[2]

A key of thinking is addition of electron-waves that is having an electric current. Electron-waves (plural material wave) depart from cathode and make propagation to anode at that time. While electron-wave propagates, mutual interference arises. Wave is added with wave during propagation.

And, the electric current is in proportion to electron-wave intensity. Alternating component of resonant circuitry current of cold cathode lay is expressed by proportion of an electron-wave group. Transition probability w_ψ (Fermi's Golden Rule) to change from energy level E_L in unit time is provided from perturbation theory depending about time.

When initial state n changes to final state l,
if $\langle \psi_l^{(0)} | H_l | \psi_n^{(0)} \rangle$ is a constant of real number, and $\rho\left(E_n^{(0)}\right)$ is a density of states, w_ψ is given as;

$$w_\psi = \frac{2\pi}{\hbar}\left(\langle \psi_l^{(0)} | H_l | \psi_n^{(0)} \rangle\right)^2 \rho\left(E_n^{(0)}\right) \qquad (1)$$

Now, angular speed of phasor ω is replaced $2\pi\nu$

$$2\pi = \int_{-\infty}^{\infty} \frac{\sin^2\left(\frac{1}{2}\omega\right)}{\left(\frac{1}{2}\omega\right)^2} d\omega \qquad (2)$$

$$2\pi = 2\pi \int_{-\infty}^{\infty} \frac{\sin^2 \pi\nu}{(\pi\nu)^2} d\nu. \quad (3)$$

Let w_ψ multiply by Planck's constant $\hbar$. If electron-wave make matter X, it has expected value W about energy $E = h\nu$. Expected value W of energy is given by energy (power) spectral density of unit time as;

$$W = h w_\psi \int_{-\infty}^{\infty} \frac{\sin^2 \pi\nu}{(\pi\nu)^2} d\nu. \quad (4)$$

Sampling function form "$/\nu$" in expression includes character of "$1/f$ noise electron momentum".

Then $\alpha = \frac{1}{2}$, $|\exp^{i\omega t}| = 1$. If $\exp^{2i\omega t}$is 1, and initial phase was tuned to $2n\pi$,

$$W = \hbar w_\psi \int_{-\infty}^{\infty} \frac{\sin^2 \alpha\omega}{(\alpha\omega)^2} \exp^{2i\omega t} d\omega. \quad (5)$$

Therefore $v = \sqrt{\frac{2}{m}E}$, Group velocity of real number v_g is given as;

$$v_g = 2\sqrt{\frac{\pi}{m}}h\left(\frac{1}{2\pi}\int_{-\infty}^{\infty} \sqrt{w_\psi(\omega)}\frac{\sin\alpha\omega}{\alpha\omega}\exp^{i\omega t} d\omega\right). \quad (6)$$

Within parenthesis of eq 6 is named y.

$$y(w_\psi, t) = \frac{1}{2\pi}\int_{-\infty}^{\infty} \sqrt{w_\psi(\omega)}\frac{\sin\alpha\omega}{\alpha\omega}\exp^{i\omega t} d\omega \quad (7)$$

By volume density ρ_{vol}, Cross-flow section S, and Elementary charge e, electric current j is given as;

$$j(t) = e\rho_{vol}Sv_g = 2e\rho_{vol}S\sqrt{\frac{\pi}{m}}hy(w_\psi, t). \quad (8)$$

2-a. PHASE COINCIDENCE OF $1/f$ RESONANCE

Transition theory includes case of degeneracy. Resonance continues by degeneracy. Dependence of all transition probability $w_\psi(\omega)$ is selected as one in a beginning of resonance. (We will prove properties of resonance in another chance.)

$$j(t) = e\rho_{vol}S\sqrt{\frac{h}{m\pi}}\int_{-\infty}^{\infty} \frac{\sin\alpha\omega}{\alpha\omega} e^{i\omega t} d\omega \quad (9)$$

Spectrum in resonance has had a sampling function. Because sampling function has ω in a denominator, there is character of $1/f$. However, all initial phase does not have to be in unison. We omit consideration of initial phase in order to simplify a calculation.

In statistics about magnitude of the signal which came in one period, one mean value exists from central limit theorem by all means. It is direct current.

Rayleigh distribution shows no order, and it becomes only white noise. Therefore 1/f noise does not coexist with Rayleigh distribution. Thus only-one-wave must be made by electron, if electric current has $1/f$ characteristic.

Because resonance is the main reason of anomalous heat, we will investigate a cause.

2-b. EFFECTIVE MASS AND FORCE

When electron beam was inclined by electric field of biprism, acceleration of force added to electron is in proportion to electric field and intensity of an electron material wave.

Factor of electric current is specific charge and electron density, mass of electron, and velocity of electron. The electric current is product of those elements.

When electric-current is in proportion to electron-wave, and mass of electron is in proportion to electron-wave, too. Then the force which let electron beam incline is to include a product arithmetic of electron-waves. Now new wave equation is made by the product.

In electron-wave number k, effective mass m of an electron propagating the inside of semi-conducting crystal is

$$\frac{1}{m} = \frac{1}{\hbar^2}\frac{d^2E(k)}{dk^2}. \quad (10)$$

However, crystallization of propagation medium is necessary for a constitution condition of this equation.

There is a potential barrier row in crystallization, and there is a work of infinite lattice of Toda in the row, and soliton propagates a row.

Because electron-wave and an electron with mass can propagate in an electrode gap, there will be something that is equal to crystal on the gap.

By the way, nature of a particle is lacking in a solution of the Maxwell equation about the electron of cold cathode lay. (We omit this proof and leave it to the next article.) Cathode ray cannot solve nature of a quantum from the Maxwell equation.

So another equation is necessary for propagation of an electron. Therefore we have to make a new wave-equation with particulate about propagation of cold cathode lay.

Tunneling rises at the time of half-transmitting-boundary condition with electron-wave in an electrode-gap, and standing-wave exists. If standing waves synthesize one-dimensional lattice, we think that even propagation in a vacuum without propagated-medium is tunnel-resonance-phenomena of a phonon-quantum, and the idea do not wake up contradiction.

Electron wave spreads through space of a domain of gap and cannot specify limited part place. However, wave strengthens it in wave packet, and a wave crest is created, and it goes straight on. The wave crest converges in a point with observation of a tunneling-electron-microscope or a transmission-electron-microscope. Therefore a wave crest of electron-wave is considered to be particulate of an electron. On the other hand, because energy E of Newton dynamics is product (product of power F and distance), energy becomes $dE = Fv_g dt$.

Because energy E is the function that differential calculus is possible by wave number, energy E of wave packet has distribution density about wave number.

$$dE(k) = (F \cdot v_g)dt. \quad (11)$$

From semiconductor-electrical-engineering, $dE(k)$ is given as;

$$dE(k) = \hbar v_g dk. \quad (12)$$

Accordingly, F in eq 11 is given as;

$$\hbar\frac{dk}{dt} = F. \tag{13}$$

The force is made of electron-wave. Electron wave produces progressive wave and standing wave in an electrode gap with tunneling.

Nature of a quantum is made by these electron-wave. And the following will become clear that even mass of a quantum is made by these electron-wave.

The probability-waves will synthesize undulations (Like teeth of a comb in Fig.1:) that stand in line with a simple condition from the higher harmonic group of standing-wave.[3)]

3. STANDING WAVE OF ONE ELECTRON

We are thinking about standing wave to make a lattice. Therefore the first stage, with a condition of one quantum in a well, Shrödinger equation is given as;

$$\left[-\frac{\hbar^2}{2m}\frac{d^2}{dx^2} + V(x)\right]\psi(x) = E\psi(x) \tag{14}$$

$$0 \le x \le d, \qquad V(x) = 0 \tag{15}$$

$$-\frac{\hbar^2}{2m}\frac{d^2\psi}{dx^2} = E\psi(x) \tag{16}$$

$$\psi(x) = A\sin(k_n x) + B\cos(k_n x) \tag{17}$$

With boundary condition of standing wave,

$$x = 0, \psi = 0, B = 0, \quad and \quad x = d, \psi = 0, \tag{18}$$

$$k_n = \frac{\pi}{d}n, \qquad n = 1,\ 2,\ 3,\ \cdots n_p \tag{19}$$

$$\psi(x) = A\sin\left(\frac{\pi}{d}nx\right). \tag{20}$$

3-a. SYNTHESIS STANDING WAVE

We are thinking that more than one standing wave exists between electrodes. The property of amplitude in inverse proportion to frequency of 1/f is added to those characteristics.

A wave equation is three dimensions of function for a cube, but we calculate only a single dimension. Because Kirchhoff's law is calculated with a single dimension, it is held good.

Higher harmonic is composed in relation to order from n to infinity as a large enough integer. A overall length of phase angle of fundamental (the first harmonic) standing wave is $k_n d = n\pi$-rad.

Fundamental wave of electron-wave is f_1. Order of harmonic is l. Wave number k_1 of fundamental wave is $k_1 d = n\pi$-rad. Amplitude of resonance is $A = 1/(lf_1)$. Equation 9 represents Ψ^2 in eq 22

$$\frac{\pi}{d}nx = \frac{\pi n x k_1}{\pi n} = k_1 x \tag{21}$$

$$\Psi^2 = \frac{1}{f_1^2}\left(\sum_{l=1}^{\infty}\left(\frac{1}{l}\sin(lk_1x)\right)\right)^2 = \frac{1}{f_1^2}y_{ham}. \tag{22}$$

Ψ^2 is divided by fixed number $1/f_1^2$, and a part surrounded by parenthesis named y_{ham}. Figure 1: is synthesized by harmonics. Because it is existence probability wave, figure 1: represents a row of existence positions. y_{ham} makes n_p mountains, and the mountain

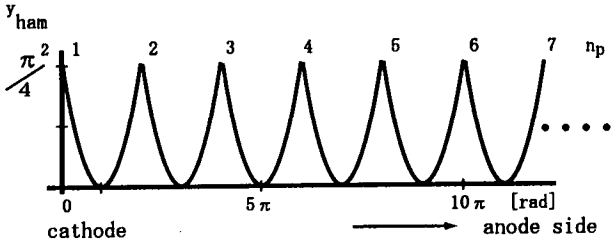

Fig. 1: Synthesis of harmonic y_{ham}

stands in line like teeth of a comb, and height is $\pi^2/4$. n_p is integral part of $n/2+1$. If there are a lot of particles, a particle stands in line every each top.

As a result, in an electrode gap, there is not substance, but a lattice of a synthesis image is made.

3-b. TUNNEL RESONANCE

As standing wave of synthesis is velocity zero, the electric current is 0-A, but the electric current can be in the electrode gap because there is soliton progressive wave in tunnel resonance of a lattice. The potential barrier stands in a row at a lattice. We can consider the row to be Kronig-Penny model.

When Katsuhiro Nakamura et al. calculated the transport of quantum by Kronig-Penny model, the energy spectrum density had being the square of momentum, that had $1/f$ characteristic, with any magnitude of circuit voltage.[4)] We can take it as a phenomenon of a lattice thereby.

If a quantum propagates a lattice, eq 22 is exempted from the eigenvalue, for the reason that limitation is not severe as for band theory.

4. NEW WAVE EQUATION

Electric energy is separated into phonon and photon in crystal of a semiconductor and propagates a lattice. A phonon quantum is a soliton propagating in a lattice. The signal of soliton includes the wave that the amplitude is in inverse proportion to frequency.

Photon can propagate an electrode gap by electric field of transverse wave and action of magnetic field, but propagation of phonon needs a medium of a lattice.

The medium that become form of the lattice which is necessary for propagation of soliton has been composed already by a virtual image of standing waves. When phonon propagates in an image of one-dimensional lattice between electrode-gaps, a new equation 36 is concluded with the following.

Partial derivative notation "$\partial/\partial x$" is expressed in "$,x$". And "$\partial^2/\partial x^2$" is expressed in "$,xx$". As amplitude $u = u(x,t)$ of soliton, a KdV equation becomes as follows.[5)]

$$u_{,t} - 6uu_{,x} + u_{,xxx} = 0 \tag{23}$$

This solution u becomes potential of Shrödinger wave equation. A relation is created by Shrödinger equation and KdV equation as;[6)]

$$-\frac{d^2\phi}{dx^2} + u(x,t)\phi = k^2\phi. \tag{24}$$

k^2 is a spectrum parameter. A soliton has mass m and kinetic energy. Wave height u is energy potential of electron swarm.

$$u(x) = \left(\frac{\hbar^2}{2m}\right)^{-1} V(x) \tag{25}$$

$$k^2 = \left(\frac{\hbar^2}{2m}\right)^{-1} E \tag{26}$$

Wave function of Shrödinger wave equation is $\phi(x, t : k)$. In wave function ϕ of Shrödinger wave equation,

$$\int_{-\infty}^{\infty} \phi^2 dx < \infty. \tag{27}$$

In this way there is the wave solution that the amplitude converges in zero in a distant place.[6] As it is converging wave, there is nature of a particle.

But the amplitude of standing wave does not converge. Soliton is caught by section if it continues being reflected. Then a reflection has standing wave and progressive wave. Because standing wave is constant wave, a calculation of Fourier transform is possible.

A product of waves by $u\phi$ making amplitude modulation is settled in the second term of eq 24; the leftside of equal sign.

When derivation L and derivation B are given as following;

$$L = -\left(\frac{\partial}{\partial x}\right)^2 + u \tag{28}$$

$$B = -4\left(\frac{\partial}{\partial x}\right)^3 + 6u\frac{\partial}{\partial x} + 3u_x \tag{29}$$

$$\begin{cases} L\phi = k^2\phi \\ \dfrac{\partial\phi}{\partial t} = B\phi \end{cases} \tag{30}$$

The upper section eq 30 is Shrödinger wave equation. The lower section is an equation about Soliton. The upper equation has N- soliton solution on u as follows. It is a solution of quantum unit nonlinearly.[7]

$$u(x, t) = 2\left(\frac{\partial}{\partial x}\right)^2 \log\tau(x, t) \tag{31}$$

$$\tau(x, t) = \exp(a_1 X(p_1, -p_1)) \cdots \cdot \exp(a_N X(p_N, -p_N)) \cdot 1 \tag{32}$$

$$X(p, -p) = \exp(\eta(t, p) - \eta(t, -p)) \times \exp(-\eta(\tilde{\partial}, p^{-1}) + \eta(\tilde{\partial}, (-p)^{-1})) \tag{33}$$

$$\eta(t, p) = \sum_{n=1}^{\infty} t_n p^n \tag{34}$$

$$\eta(\tilde{\partial}, p^{-1}) = \sum_{n=1}^{\infty} \frac{1}{n} p^{-1} \partial_n \tag{35}$$

Wave ϕ has a characteristic of $1/f$ by resonance from condition of standing wave. Both sides of the upper section eq 30 are differentiated with t by the requirements that wave ϕ was compatible in a simultaneous equation, and simultaneous equation eq 30 becomes the next equation.

$$\left(\frac{\partial L}{\partial t} - [B, L]\right)\phi = 0 \tag{36}$$

$$now, \qquad [B, L] = BL - LB. \tag{37}$$

We named eq 36 soliton Shrödinger wave equation from character of physical phenomenon. The eq 36 is made of application of literature.[6]

Having singular equation is a principle of physics that one equation is created with regard to energy. Therefore equation 36 is more superior in a point of simplification than simultaneous equations 30.

$[B, L]$ are calculation of Lee-bracket-product, and there is nature of folowing equation.

$$\frac{\partial L}{\partial t} - [B, L] = u_{,t} - 6uu_{,x} + u_{,xxx} = 0 \tag{38}$$

Relationship of right-hand member on the first line and the second is the KdV equation that displayed eq 23 with a method of Lax. The whole is the generalization that a KdV equation, Maxwell wave equation and Shrödinger wave equation have consisted simultaneously after all.

eq 24 is found with the separation of variables form which is unrelated to time of eq 36. Therefore we name eq 24 "soliton Shrödinger equation." Two factor of the $u\phi$ product term gains new another amplitude modulation wave.

Because outbreak is only once, solitary wave is not observed if there is not luck. However, if there has been amplitude modulation, fluctuation is observed any time.

Frequency and the amplitude are in proportion to reverse even if it measured with any kind of method for $1/f$ noise. Even if it was greatly different in length of the observation period, it is mysterious that it is in frequency component to be the same as one solitary wave. The question clears up by existence of amplitude modulation.

Both elements of $u\phi$ are electron-wave. And u of progressive wave of electron-wave has a dimension of energy, and ϕ has no dimension on existence probability. This problem is solved as follows.

Electron wave ϕ is converted into u of dimension of energy by relation of the following conservation law by volume integral of energy density $W_{\kappa j}$. Because a product of wave is the same as a principle of amplitude modulation, 3^{rd} (side band) wave occurs. As for the side wave, the carrier wave, the signal wave, each wave numbers is expressed with $k_0 = k_1 + k_2$. And ω $(= 2\pi f)$ is expressed with $\omega_0 = \omega_1 + \omega_2$.

By indication of a non-linear term ingredient (NL), electric susceptibility is $\chi^{(n)}$ with term of ordering n. It is $\chi^{(n)}$ with electric susceptibility about an ingredient of n index, and by indication of a non-linear term ingredient (NL), it is shown a conjugate of complex number $*$ with three-electron-wave ϕ_0, ϕ_1, ϕ_2. Energy conservation law becomes as follows.[8]

$$\frac{d}{dt}\sum_{j=0}^{2} W_{\kappa j} = i(\omega_0 - \omega_1 - \omega_2)\chi^{(NL)}\phi_0^*\phi_1\phi_2 = 0 \tag{39}$$

Momentum density of wave is P_{k_j}. Momentum conservation law is given as;

$$\frac{d}{dt}\sum_{j=0}^{2} P_{\kappa_j} = i(\mathbf{k}_0 - \mathbf{k}_1 - \mathbf{k}_2)\chi^{(NL)}\phi_0^*\phi_1\phi_2 = 0. \qquad (40)$$

There is meaning that group of electron-wave will be converted into potential, momentum, and mass from eq 39, and eq 40. Electric current and an electron have been made from only electron-wave.

For example, the potential becomes the same as potential of a fluid when electron groups flow and make direct current or electrostatic field. A signal of $1/f$ was output (3^{rd}) in an experiment that two lasers ($1^{st}, 2^{nd}$) different in a wavelength were input into crystal simultaneously.[9] Because crystal and two lasers each had a matter-wave, the experiment is an example of evidence.

5. INFILTRATED OF DEUTERIUM LAYER

There is only one electric current to flow through a closed circuit. Therefore all sections have electron-wave of the same frequency characteristics uniformly. An electric current of a circuit makes a lattice of electron-wave in infiltration section of deuterium. Figure 2: shows a schematic representation of Cold cathode-Lay.

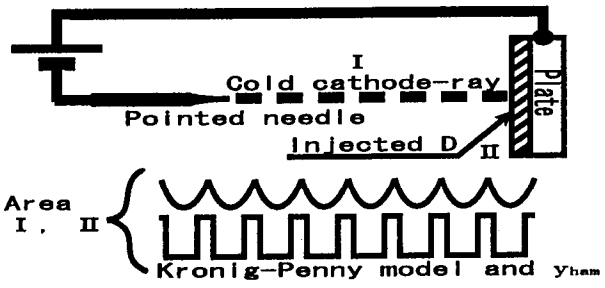

Fig. 2: Illustration

The deuterium which floated is drawn to lattice point by the gravitation eq 13 that electron-wave arises after the deuterium was injected between metal.

A work of the gravitation was taken to a photograph. A laser beam propagated to circular wave guide, and standing wave of electron-wave drew a particle to a section of flux.[10] It is the example that electron-wave made gravitation. Another example was shown in technique to carry one unit of atom with tunneling electron microscope.

Deuterium stands in line on teeth of a comb of one-dimensional lattice by the gravitation that electron-wave made, and a figure of lining up seems to be a pearl chain. When a phonon quantum propagates there, energy is accumulated according to virial theorem by each step of a lattice. An electron ranges in an electrode gap, and an electron stores energy of vibration like a lattice point.

When an electric current changes, an interval of teeth of a comb changes simultaneously then. A total of energy to store in each lattice is large, but the income and expenditure of energy is equal by a unit of a quantum in once of change. Cold fusion of big unit can be caused then by small fluctuation. The composition acts in a phenomenon then.

6. CONCLUSIONS

When cold cathode lay arises in an electrode gap of direct current electric circuit, the electron-wave that seems to be virtual crystal or a lattice will be generated by resonance. And soliton electron-wave becomes with $1/f$ noise (resonance), and tunnel resonance phenomena arises when it travels by a lattice of self excitation.

We have utilized the new wave equation that had a solution of the meaning $1/f$. We considered mechanism of Cold fusion that was resonance of electron wave which made a lattice of composition.

If a resonator producing resonance of electron-wave powerfully is developed, a generation of heat phenomenon will be in any time.

If we adjust interval of a lattice of electron-wave and lattice spacing of deuterium in a molecule, technology of Cold fusion may be born.

ACKNOWLEDGEMENTS: The author acknowledges discussions and suggestions by M. Nakamura, T. Sekiguchi, A. Nagata, M. Tsuda, M. Tuchiya and Y. Shinohara.

References:

1) K. Kisi, H. Eda: Electrostatic cooling, Journal of IEIC, 9/'77, vol.60, no.9, pp.1044-1046, Sep. (1977), in Japanese.

2) A. Tonomura, J. Endo, T. Matsuda, T. Kawasaki: Demon-stration of single-electron buildup of an interference pattern, Am. J. Phys. , vol. 57, no. 2, pp. 117-120, 1989.

3) M. Ban: 1/f Noise and Tunnel Resonance by Interaction Coulomb Forcd between Electrons, IEICE, TECNICAL REPORT OF IEICE, EMCJ2000-1(2000-04), in Japanese.

4) T.Haga, Y.Takane and K.Nakamura: $1/f^2$ Law in One-dimensional Quantum Transport: an Example of Weak Chaos in Quantum Systems, Chaos Solitons & Fractals Vol.5,No.7,pp.1077-1083,1995.

5) Gardner, C. S. , Green, J. M. , Kruskal, M. D. , and Miura, R. M. , Phys. Rev. Letters**19**(1967),1095.

6) Kimio Ueno: Extent of a nonlinear wave. The infinite world carried by a soliton., Mathematical Sciences, no.387, pp.42-47, Sep. , 1995, in Japanese.

7) E. Date, M. Jimbo, M. Kashiwara and T. Miwa: Operator approach to the Kadomtsev-Petviashvili equation Transformation groups for soliton equations III, Journal of the Pysical Society of Japan, vol.50, No.11, Nov. , 1981, pp.3806-3812.

8) T. Taniuti, K. Nishihara: Nonlinear Waves, Pitman Advanced Publishing Program, Boston, 1983; translated from the Japanese edition of Iwanamisyoten, 1977.

9) T. Musha, Borbély Gábor, M. Shoji: 1/f Phonon-Number Fluctuations in Quartz Observed by Laser Light Scattering, Phys. Rev. Lett. , vol.64, no.20, pp.2394-2397, May. , 1990.

10) Hiroaki Misawa, Keiji Sasaki, "Laser Scanning Micromanipulation," Japanese Journal of Optics, vol. 21, pp.91-92, 1992, in Japanese.